Untangling the branches: Genomic and Cytoskeletal insights to the neuron-like morphology of the amoeba *Filoreta ramosa*

By

SARAH LILY GUEST

DISSERTATION

Submitted in partial satisfaction of the requirements for the degree of

DOCTOR OF PHILOSOPHY

in

MICROBIOLOGY

in the

OFFICE OF GRADUATE STUDIES

of the

UNIVERSITY OF CALIFORNIA

DAVIS

Approved:

Scott Dawson, Chair

Bo Liu

Kassandra Ori-McKenney

Committee in Charge

2023

ABSTRACT

Untangling the branches: Genomic and Cytoskeletal insights to the neuron-like morphology of the amoeba *Filoreta ramosa*

By

Sarah Lily Guest

Comparative genomic studies across the eukaryotic tree have provided valuable insights into eukaryotic evolution, but many key microbial taxa have been overlooked due to their absence from culture collections. Among these taxa are the largely neglected Rhizaria, a supergroup and member of the Stramenopile, Alveolate, Rhizaria (SAR) clade that comprises approximately 60% of all eukaryotic diversity. Although ubiquitous in the environment, the Rhizaria have received limited attention in terms of molecular and cell biology, development, and genetics compared to other lineages due to difficulty establishing and maintaining laboratory cultures. Nonetheless, Rhizarian amoeboid protists offer insights into the evolution of multicellularity, morphological complexity, and mechanisms for spatial differentiation during their often multiphasic lifecycles. Many Rhizarian amoebae exhibit a network of reticulopodia, specialized pseudopodia that form a branched morphology resembling neuronal arbors. Despite the striking morphological similarities, the cell biology and shared components between Rhizarian amoebae and metazoan neurons remain poorly understood.

This study presents the first comprehensive genomic description and cytoskeletal investigation of *Filoreta* ramosa, a Rhizarian multinucleate (syncytial) amoeba isolate. Using fluorescence imaging and drug perturbations, we reveal the remarkable similarity of *Filoreta*'s cytoskeleton to that of neurons, suggesting an ancient conserved mechanism driving this morphology. The

elaborate cytoskeletal architecture enables rapid organelle transport and dynamic reorganization in response to the environment. Notably, the interphase microtubule array in *Filoreta* syncytia organizes longitudinally, facilitating bidirectional transport and displaying potential for parallel and antiparallel bundling through non-centrosomal nucleation. Furthermore, *Filoreta* demonstrates versatility by forming lamellipodia and filopodia, indicating a diverse repertoire of actin and actin-associated cytoskeletal proteins.

Genome analysis uncovers cytoskeletal and signaling proteins that further support *Filoreta*'s neuron-like behavior during the development of its complex arborized network and environmental sensing. The findings shed light on the cell biology and mechanisms underlying the intriguing convergence between Rhizaria and metazoan neurons. Additionally, we present a robust cultivation method for free-living amoeboid protists, expanding the available models for future investigations of non-model amoeboid organisms at the molecular, cellular, developmental, and genetic levels. This multiphasic analysis sets the stage for further research into the evolutionary and functional aspects of Rhizaria, offering valuable insights into eukaryotic cytoskeletal evolution.

ACKNOWLEDGEMENTS

I thank Dr. Scott Dawson for being there the day I found my first amoeba, his years of mentorship, enthusiasm, and support in my research.

I thank Dr. Kari Hagen for her encouragement, kindness, humor and wisdom.

I thank my committee Drs. Bo Liu, Sean Collins (previous committee member), and Kassandra Ori-McKenney for their expertise and guidance.

I thank two other professors in the Microbiology Department, Drs. Rebecca Parales and Doug Nelson for their friendly encouragement through the years.

I thank my friend and fellow lab mate Hannah Starcevich, for being there in the fun times and hard times, and helping me maintain my sanity through it all.

I thank my dad for teaching me resilience, persistence, a strong handshake, and how to use the right kind of “elbow grease” to get the job done.

I thank my mom for instilling my deep love of biology from an early age, encouraging my curiosity, and supporting my goals with unmatched determination.

I thank my cat Otter, who nearly made it to the end with me, spent all the late nights by my side, and filled my life with as much joy as he could in the ten years we had together.

I thank my partner Kirk for his diligence, motivational support, encouragement, and being a sounding board for my ideas.

List of Figures

Chapter 1

Chapter 2

Chapter 3

List of Tables

Chapter 1

Robust methods for cultivation, identification, and fixation of novel freshwater and marine amoebae

Sarah L. Guest and Scott C. Dawson

Department of Microbiology and Molecular Genetics

One Shields Avenue

UC Davis, Davis, CA 95616

Abstract

Protists play a pivotal role in resolving the evolution of eukaryotes, but they remain underrepresented in genomic and functional research models, at least in part due to lack of stably isolated laboratory strains. Amoeboid protists, despite their widespread presence in the environment, remain understudied due to challenges in processing and isolating adherent and delicate cells from raw environmental samples. To address this, I outline a method for enriching and isolating diverse amoeboid protists which instead capitalizes on their adherence, enabling effective and reproducible isolation of diverse clades. Descriptions of amoeboid species historically relied on morphological observations, with limited functional investigations. The ability to generate mono-eukaryotic strains of amoebae creates a conduit for species to be assessed in long-term functional study, linking classical morphologic-protistology approaches and contemporary cell biology to examine amoeboid features at a greater depth.

This report describes methods of isolation, identification, culture maintenance, and cytoskeletal examination of varied species from several major eukaryotic lineages, demonstrating the diversity of pseudopod morphology within and throughout the eukaryotic tree. I examined the prevalence of different modes of amoeboid locomotion in the strains generated by this method, and bridged pseudopodial type with phylogenetic placement. To go beyond brightfield live imaging approaches, I optimized fixation and immunostaining of the amoeboid cytoskeleton in particularly delicate marine species. These techniques offer a robust strategy for initial studies on free-living amoeboid protists, facilitating further research on protistan groups.

Introduction

Amoebae are predatory protists that are ubiquitous in diverse environments. While often referred to as a single taxonomic group of eukaryotes, amoebae do not belong to a single taxonomic clade and are found in nearly every major lineage across the eukaryotic tree. Each of the major eukaryotic supergroups including Amoebozoa, Excavates, Opisthokonts, Stramenopiles, Rhizaria, and even Archaeplastida contain amoeboid cell types (Goodson et al., 2021; Kang et al., 2017; Pawlowski and Burki, 2009). Amoeboid motility can be thought of more as a phenotype rather than a phylogenetic grouping.

The term amoeba is derived from the Greek word for change (amoibe, ἀμοιβή) which underscores the key factor in determining the amoeboid cell type. Amoebae undergo drastic morphological changes required by their locomotion. The amoeboid cell is one that lacks a rigid cell wall and is capable of undergoing changes in its shape by membrane deformation. Typically, amoebae are adherent to surfaces and are motile via pseudopodial turnover. Many morphotypes, however, do not adhere fully and maintain buoyance in the water column of aqueous environments by changing their surface area using pseudopodial projections (Gast, 2017).

Despite their widespread prevalence in numerous environments, amoeboid protists are relatively understudied at the functional level due to a lack of current methods for adherent cell isolation from raw environmental samples. Adherent amoebae are not easily sorted under flow cytometry, as they often adhere to large pieces that are typically removed in the pre-filtering step. Additionally, many amoebae do not tolerate the turbulence and high pressure associated with flow sorting machinery. By using a method of isolation that takes advantage the adherence of

many amoebae, we can effectively isolate amenable strains from a diversity of environmental sources without prefiltering samples.

Most cell biological models are of interest for their implications in human health, limiting the depth of knowledge of free-living amoebae from a diversity perspective. Free-living protists and amoebae, particularly those from marine or anoxic environments, are less developed as models for cell biology. Traditionally, descriptions of new amoeboid species are purely descriptive using either light or electron microscopy and far fewer have undergone in-depth investigations of the amoeboid morphology from structural and functional cell biological approaches. Other approaches investigating cytoskeletal evolution from gene content often do so with uncultivated protists, limiting the depth of functional study once the organisms are extracted (Burki et al., 2020; Krabberød et al., 2017; Liu et al., 2017). This leaves an obvious void in the field of protistan cell biology and a pending question: does uncultivat*ed* mean uncultiv*able*? Thus, there is a need for amoeboid protists that that are amenable to laboratory culture to bridge the gap between classical protistology and modern cell biological approaches to understand amoeboid motility.

For this reason, we have adapted and modified methods for enriching and isolating diverse amoeboid protists from marine environments which minimizes the potential for growing freshwater/soil-associated pathogenic species (i.e., *Naegleria, Acanthamoeba, Balamuthia*) or for carrying pathogenic intracellular bacteria (i.e. *Listeria, Legionella, Bordetella*) (Strassmann and Shu, 2017). The streamlined method for the enrichment and isolation presented here resulted in isolation of diverse species of amoeboid protists from primary eukaryotic lineages including Excavata, Rhizaria, Amoebozoa, and Opisthokonts. Overall, these methods provide a robust

strategy for the initial studies of free-living marine amoeboid protists that can be completed within weeks.

Results

Diversity of amoebae and morphotypes

We isolated and identified amoebae in four of the major eukaryotic supergroups, exhibiting all of the pseudopodial morphotypes (Figure 1.1A). Lamellipodia, filopodia, lobopodia, reticulopodia, and blebbing motility were observed in both freshwater and marine isolates, while axopodial morphology was only observed in one planktonic isolate from marine samples.

A total of 79 amoeba isolates were successfully isolated and their small subunit ribosomal RNA (SSU rRNA) sequenced (Table 1). We distinguished 17 different genera across four eukaryotic supergroups: Amoebozoa, Opisthokonts, Rhizaria and Excavates. Of the 79 isolates, 11 were unable to be identified by alignment using the NCBI database. These isolates had regions of high variability and did not have similarity to monophyletic groups. For example, strain "P5A" had a 77.04% identity over 29% of its sequence length to a Vannellid amoeba, and 76.73% identity over 36% of its sequence length to *Pinnularia*, a diatom.

Marine and freshwater sources had similar yields for amoeba isolates; 41 of the isolates were from marine environments and 38 were from freshwater. Both marine and freshwater isolates had representatives from Amoebozoa, Rhizaria, and Excavates. Many of the marine isolates were related (i.e. >97% partial 18S rRNA gene sequence similarity) to known genera; *Neovahlkampfia* (13 isolates), *Filoreta* (5 isolates), *Flabellula* (3 isolates), *Cunea* (3 isolates), *Pseudoparamoeba* (2 isolates), *Massisteria* (1 isolate) and *Neoparamoeba* (1 isolate). Ten marine isolates we called "Undetermined" had partial 18S rRNA gene sequence similarity

less than 85% to closest described species, and most had partial query coverage, with variable regions between aligned segments.

The freshwater isolates included *Vahlkampfia* (11 isolates), *Acanthamoeba* (5 isolates), *Vermamoeba* (5 isolates), *Tetramitus* (5), *Naegleria* (4 isolates), *Stenamoeba* (4 isolates), *Ripella*, *Spongomonas* and *Nuclearia* had 1 isolate each. One isolate, "M105" was undetermined, with approximately 88% similarity over 77% of the sequence length to *Echinamoeba*, (Amoebozoa), *Roombia* (Cryptista) and *Glomeromycotina* (Fungi).

Freshwater amoeba isolates from an algal layer in a UC Davis campus greenhouse were isolated and identified by SSU rRNA sequencing to be *Vermamoeba vermiformis* (99%) *Nuclearia pattersoni* (98%), and *Ripella platypodia* (%). Isolates from a similar biofilm on a north-facing apartment patio were identified as *Stenamoeba dejonckheerei* (98.7%), *Spongomonas minima* (98.7%) *Vermamoeba vermiformis* (99%), and *Vahlkampfia avara* (99%). Isolates from Putah Creek included *Vahlkampfia avara* (99%) and *Naegleria gruberi* (98%). A seasonal creek running through Waterman Canyon, CA yielded *Tetramitus* sp. (99%) and *Acanthamoeba castellani* (98.7%). Samples from the Vic Fazio Causeway had *Acanthamoeba castellani (99%), Vermamoeba vermiformis* (99%), and *Vahlkampfia avara* (98-99%).

Our marine and brackish amoeba isolates originated from sediments collected at Little Sippewissett Marsh and Trunk River, near Woods Hole MA, and from marshlands bordering Bodega Bay, CA. Sippewissett isolates were identified as *Cunea* (96-97%), *Pseudoparamoeba* (95-97%), *Neoparamoeba branchiphila* (98%), *Vexillifera* (96-97%), *Neovahlkampfia damariscottae* (92-98%), *Filoreta* sp. (86-98%), and 10 undetermined lineages. Trunk River

lagoon sediments yielded *Flabellula baltica* (99%), and *Filoreta* sp. (95%). Bodega Bay isolates included *Filoreta* (99%), *Flabellula* (88%) and *Massisteria* (99%).

There was a substantial amount of overlapping pseudopodial morphologies across clades, and most genera were capable of producing more than one pseudopodial type (Figure 1.2). Of the various morphologies, blebbing motility was the most abundant type to be isolated using these cultivation methods, but was mostly observed in Heterolobosean isolates, with the exception of *Cunea* sp. Lobopodia were also very common across isolates, and were observed in more genera (all Amoebozoa) than blebbing motility. Lamellipodia and filopodia had the largest diversity distribution, as they were observed in isolates belonging to Amoebozoa, Rhizaria and Opisthokont lineages.

Cyst formation across isolates

Most of the freshwater isolates produced cysts, while some marine isolates did not. *Cunea*, *Vexillifera* and *Massisteria* did not encyst at all, and the *Flabellula* isolates made pseudocysts that quickly exited the rounded form in favorable conditions (Figure 1.3C). Most freshwater isolates made simple spherical cysts, like the *Vahlkampfid* relatives (Figure 1.3A). *Nuclearia* formed distinct polyhedral cysts with linear sides that were reminiscent of cubic, octahedral, and icosahedral shapes (Figure 1.3B). Several of the marine novel amoebae did not encyst, though "P5A" has unusual longevity despite lack of cyst formation. A liquid culture of P5A was stored in sterile SWB without nutrients at room temperature for 3 years and recovered activity within 48 hours after feeding.

Fixation optimization based on cytoskeletal preservation in marine amoebae

Three methods of fixation were used to preserve and visualize the delicate structure and cytoskeleton of the marine amoeba strain SW4B from Sippewissett Marsh.

We optimized fixation of marine amoebae using the *Filoreta* strain SW4B to guide appropriate structural retention, with the notion that if cytoskeletal features were preserved in this sensitive amoeba, they would be preserved in most others. This amoeba presented the largest challenge as it grew as a delicate network across the culture surface and was very reactive to changes in the salinity, pH and osmolarity of the medium.

First, evaluation of adhesion on coverslips coated with 0.1% poly-L-lysine versus 0.1% gelatin (Methods) resulted in better retention of cell bodies on the gelatin-coated glass. Amoebae adhered better, grew in a manner similar to culture surfaces, and were less likely to become dislodged during the fixation and staining process. During fixation of marine amoebae, the presence of calcium dramatically altered cell shape during fixation. The pre-fixation step of replacing growth medium with calcium-free seawater (CFSW) was crucial to avoid beading and loss of membrane continuity (Figure 1.4A).

Fixed samples were assessed on whether they were morphologically preserved, in which broken pseudopodia and fractured network structure was apparent in overfixed, brittle samples (1.4A, third panel). Samples that were intact and appeared identical to live cultures were used in downstream optimization (1.4A, right panel).

Morphology was intact but lost microtubule structure when fixed with 0.5% glutaraldehyde in CFSW lacking sucrose (Figure 1.4B). The actin cytoskeleton was preserved, but microtubules depolymerized and fractionated into short fragments. The samples were also very obscured by

dense bacterial adhesion to the gelatin-coated coverslips. We fixed this issue by performing a "pre-rinse" of cultures before scraping and transferring onto coverslips in wells (Methods). After adjusting osmolarity of fixative solutions with 5% sucrose, microtubule structures were observed in thin sections of the cell body. However, the thicker regions of the fixed structure were very autofluorescent (1.4C), and had to be additionally quenched with longer incubations in 0.2M glycine. After quenching, permeabilization and staining, the signal of phalloidin-labeled F-actin was not as robust (1.4D), leading to optimized staining with a longer incubation time (1.4E).

Fixatives that contained paraformaldehyde took considerably more time to properly fix, an effect of the glutaraldehyde cross-linking activity (Kiernan 2000). Samples fixed in paraformaldehyde were assessed for their microtubule preservation, and iteratively adjusted in concentration and timing with CSB and sucrose. An optimized solution of 4% paraformaldehyde, 0.4 M sucrose, and 2.5X CSB diluted in CFSW was formulated, with optimal fixation occurring at 10 minutes.

Glyoxal has been reported as an optimal fixative for preserving proteins and their structures, and works faster than paraformaldehyde without the autofluorescent issues of glutaraldehyde (Richter et al., 2018). After fixation in 5% glyoxal solution (Appendix), we found microtubules were reliably well-preserved. However, glyoxal fixatives require ethanol as an accelerator, and these samples did not retain F-actin structure (Chapter 3, microtubule curvature).

We applied the same fixation procedure to marine amoebae *Cunea* and *Vexillifera*, and saw successful retention of actin-based structures and tubulin features (1.4F). These amoebae were significantly smaller than SW4B networks, but their morphologies were adequately preserved. Next, we adapted the technique to fix *Nuclearia*, a freshwater isolate. The 0.5% glutaraldehyde

fixative solution was made in calcium-free freshwater instead of seawater, and also preserved morphology and cytoskeletal features (1.4F).

Discussion

Amoeboid motility uses pseudopodia of diverse types and mechanisms. Pseudopodial types that require cytoskeletal polymers to change shape include lamellipodia, filopodia, lobopodia, axopodia and reticulopodia. Some cells use a different strategy called "blebbing motility" that involves delamination of the plasma membrane from the cell cortex, and forward extrusion of the cytoplasm accompanied by re-establishment of cortex in the bleb (Fritz-Laylin et al., 2018). All modes present as "transient" extensions of the cell body for locomotion and prey capture, and incorporate the actin and - in many cases - microtubule cytoskeletons and their interacting proteins. They are transient much like a cloud, in that no two pseudopodia will ever be the same, nor will the same pseudopod remain identical to itself. This is due to the nature of polarized cell motility, actin polymer dynamics and that the leading edge of an amoeba constantly responds to its environment and stimuli. The F-actin network is under constant assembly at the leading edge and disassembly at the trailing end in a process called treadmilling (Pollard and Borisy, 2003).

Historically, amoeboid cell types were classified by protozoologists via their morphology and pseudopodial architecture. Modern tools have enabled identification of amoebae using conserved 18S rRNA sequencing, simultaneously elucidating and confounding the organization of amoeboid cell types by genotype and not phenotype (Kang et al., 2017; Smirnov and Brown, 2004). While from a molecular perspective the resolution of amoeba phylogeny has greatly

improved, there now also exist significant phenotypic overlaps of morphology that occur in divergent clades. Where synapomorphic phenotypes of lamellipodia, for example, exist within lineages of the Amoebozoan supergroup, there are many other extant species in other supergroups (including Rhizaria and Opisthokonts), exhibiting lamellipodia-like features in paralogous, homologous, or analogous ways. How certain cytoskeletal features function in different lineages with conserved cytoskeletal components is key unresolved question in evolutionary cell biology that is key toward understanding the last eukaryotic common ancestor (LECA) and resolving the evolution of amoeboid protists (Burki et al., 2020).

Investigation into the conserved, convergent, and diversified cytoskeletal pathways to generating morphology across the eukaryotes is a major contributor to understanding the evolution of the cytoskeleton and its capabilities (Tekle et al., 2010; Tekle and Williams, 2016). Since all of the eukaryotic supergroups, including red alga (Goodson et al., 2021), contain amoeboid cell types, the amoeba cytoskeleton, morphology, and motility provides a platform to investigate conserved proteins, divergence, and their roles across lineages. Although the nomenclature and organization of the six eukaryotic supergroups have been updated and rearranged to some extent (Burki et al., 2020), the notion stands that eukaryotic lineages are more than slightly *engulfed* by amoeboid life strategies.

Wide pseudopodial diversity can be harnessed through these isolation strategies.

We show the isolation of diverse lineages and diverse morphologies using this strategy. The most common morphotype observed in all isolates was blebbing motility (Figure 1.1A, 1.2, Supplemental video 1), a hallmark feature of Heterolobosean amoebae, but also observed in Amoebozoan and Opisthokont lineages (Maroto and Hamill, 2007). These amoeba isolates moved very quickly and grew faster than other types, granting them an advantage in our

enrichment strategy, and likely the reason why this morphotype was most abundant in our collection. Blebbing motility enables rapid movement because it isn't consistently limited by the rate of actin polymerization and treadmilling (Fritz-Laylin, 2020; Schick and Raz, 2022). The delamination of the plasma membrane from the cell cortex results in rapid expansion of semispherical blebs, and is driven through actomyosin contraction of the cell body to extrude it forward, followed by cortex recovery (Charras et al., 2006; Petrie and Yamada, 2012; Schick and Raz, 2022). In this manner, only a portion of the cortex needs to be reassembled in the direction of cell flow, enabling faster forward motility.

Several isolate types exhibited lamellipodia, including *Nuclearia*, *Flabellula*, and *Cunea* (Figures 1.1A, 1.2, 1.3F, Supplemental video 2). Lamellipodia are common in very adherent amoebae, and appear as wide, ruffled edges consisting of branched actin arrays that undergo this actin polymer turnover and protrude the membrane forward at the cell front to crawl (Fritz-Laylin et al., 2017; Innocenti, 2018). As branched actin networks are crucial for the formation of lamellipodia, the accompanying repertoire of proteins responsible for this morphology may be conserved to a certain extent throughout the eukaryotes capable of making ruffled pseudopods. Actin polymers branch with the help of the Arp2/3 complex at a very specific 70 degree angle, and in doing so, creates a polarized meshwork of actin filaments. The microtubule cytoskeleton works in tandem with the lamellipodial front, where actin binding and interactions are important for directional motility, stabilization of the cell body, positioning of organelles and transport of engulfed prey (Kopf et al., 2020).

We also identified several amoebae exhibiting filopodia, including *Filoreta*, *Spongomonas*, *Nuclearia*, *Vexillifera*, and *Flabellula* (Figure 1.1A, 1.2, 1.3F). Filopodia similarly require actin polymers, but rather than actin meshworks, filopodia incorporate conserved actin bundling

proteins and altered dynamics to create thin protrusions that extend linearly from the membrane subsurface (Mattila and Lappalainen, 2008; Steffen et al., 2006). They often protrude from the leading edge of lamellipodia but can also form independently. In some cells, their role is to probe the environment of the cell front, making them important structures for directed migration and cell interactions (Mattila and Lappalainen, 2008). At the submembrane level, the actin filaments interact with other proteins (fascin, formins, myosins) and work to deform the membrane's protruding edge into a narrow tube (Chhabra and Higgs, 2007; Houdusse and Titus, 2021). In many cases, filopodia occur at the forefront of a lamellipodial edge, and the bundling of actin filaments recruits microtubule binding proteins. When microtubule capture occurs at these sites, the directional polymerization of the cytoskeleton will follow the directionality of the angle of microtubule capture (Kopf et al., 2020).

Most of the isolates belonging to the Amoebozoa supergroup exhibited lobopodia. Lobopodia are larger, blunt, more finger-like pseudopodial projections than filopodia, but similar in that they are formed by actin polymerization to deform the membrane, combined with cortical flow driving the cell body forward as the pseudopods extend (Fritz-Laylin, 2020; Stockem et al., 1983; Tekle and Williams, 2016). Lobopodia are distinct from the blebbing motility because they are maintained by a cortical actin meshwork to prevent membrane stress or delamination, rather than blistering through contractile forces extruding the cell forward. Contractile forces that generate locomotion in this way also incorporate actin and microtubule scaffolding to maintain cell shape and direct cytoplasmic flow.

Our *Massisteria* isolate was the only strain that exhibited axopodia (Figure 1.1A, Supplemental video 3). Axopodia are thin rigid pseudopodia that extend radially around a cell, and are largely made up of microtubules in organized parallel arrays (Tilney and Porter, 1965). This allows for

enhanced rigidity and improved transport along the axopod, which can reach lengths of over 100 micrometers. Amoebae that use axopodia are usually spherical, with axopodia radiating outward, and are typically planktonic rather than adherent. Axopodia can be retracted, which involves the depolymerization of the microtubule arrays running through the core of the axopod. *Massisteria marina* is one such case, in which under stressful conditions it rapidly retracts all of its axopodia in approximately ten seconds (Supplemental video 3). Once the axopodia are retracted, its single flagella begins beating and the cell swims to a new location to escape its suboptimal environment. While this amoeba was not isolated using the plaque method, we described its cultivation to include methods of developing strains for this specialized morphotype.

Two lineages were identified with reticulopodia; *Filoreta* and the single divergent *Flabellula*-related strain "BBWNBr" from Bodega Bay, CA (Figure 1.1A, 1.2, 1.3, Supplemental videos 4, 5). The latter strain's partial SSU rRNA sequence and morphology aligned within the Amoebozoan Leptomyxida clade (Smirnov et al., 2017), but because of its low similarity to NCBI-available sequences (88%), could not be appropriately called to species. *Filoreta* was successfully cultivated from three different environments, and all exhibited the characteristic filopodia, lamellipodia and reticulopodial networks. Reticulopodia are an unusual case of pseudopod formation, because while amoebae are capable of self-fusion (membrane closure to phagocytose prey), they typically do not maintain open "loops" in their surface adherent structure. Reticulopodia are generated by branching and anastomosing (fusing) pseudopods to generate a dense network, which is efficient in covering large surface areas and trapping prey. There are reticulopodia described in multiple eukaryotic lineages including Amoebozoa (*Darbyshirella, Leptomyxa*), Stramenopiles (*Leukarachnion*), and Rhizaria (*Reticulomyxa*, Forams, Cercozoa) (Berney et al., 2015; Jaške et al., 2022). The network formed by these

amoeboid cell types can be transient or stable and may or may not be formed around a distinct cell body. Additionally, many amoebae exhibiting reticulopodia are multinucleate during at least part of their life cycle.

Multinucleate cells can develop either by multicellular aggregation or coenocytic division (Medina et al., 2020; Ondracka et al., 2018; Patino-Ramirez et al., 2021). There are many amoeboid lineages (*Dictyostelium, Physarum, Fonticula, Guttulinopsis, Capsapora, etc)* that are additionally of interest for their multicellular life cycles (Bonner, 2003; Brown et al., 2012a, 2012b; Ruiz-Trillo et al., 2004; Tice and Brown, 2022). Understanding the origins of multicellularity continues to be a point of focus in the field of cell biology. Investigating how multicellularity evolves, and the contributions of cells in cooperation toward each other, is an important part of understanding the basis of multicellular organisms in our own clade, the metazoa. Luckily, multicellularity has arisen multiple times throughout the eukaryotic tree, in every major supergroup (Amoebozoa, Stramenopiles, Alveolates, Rhizaria, Archaeplastida, Excavates, and Opisthokonts), providing a diversity of evolutionary pathways to multicellular existence. In addition, there are numerous organisms whose life cycles include switching from unicellular to multicellular stages. This allows for investigation into the transcriptional, morphological, and metabolic changes (to name a few) that occur between these formats. Under what circumstances is multicellularity beneficial or more efficient?

Aggregative multicellularity is one of the types of multicellularity that undergoes this switching. Individuals in a population will migrate towards each other, recognize another cell as “self” and cooperate together to make up a multicellular organism or structure. Upon switching to cooperative life, the many *small*, become a large *one*, and in doing so undergo physiological changes. Many of these are emergent properties, where a single cell could not accomplish what

many in cooperation can. This includes increase in size, and therefore a need for organization to ensure cooperative function, which results in cell type differentiation. For decades, the multiphasic life cycles and cell biology of the Amoebozoans *Dictyostelium* and *Physarum* have been examined, yet investigations of other lineages are limited (Bozzaro, 2019; Oettmeier et al., 2020). Our stable, clonally propagated *Filoreta* isolate is one such organism that can further our understanding of multicellularity, complex pseudopodial morphogenesis, and the evolution of eukaryotic amoeboid morphotypes.

Cysts provide a means for isolation and enrichment of diverse amoebae.

Many amoebae form dormant cysts that have lowered metabolic states and can survive in stasis for prolonged periods, ranging from seasons to decades (Lima et al., 2017; Sriram et al., 2008). Encystation is a strategy for the amoeba to survive in suboptimal conditions, and from a cultivation perspective it provides a fail-safe for laboratory culture. A culture that is able to encyst will survive a missed "feeding," rather than starve and die off. Cyst longevity is also useful for laboratory strains as they can be collected and stored for future use. Cysts can be formed from a variety of components including proteins, lipids, and polysaccharides, with many using chitin and cellulose polymers for structural rigidity (Fouque et al., 2012; Garajová et al., 2019; Siddiqui and Khan, 2012). Cysts typically are double-layered and have a diversity of shapes, ranging from spherical to ovoid, to polyhedral. Pseudocysts are similar to "true cysts" in that they enable the survival of the amoeba in unfavorable conditions but are not resistant to total desiccation or mild detergents (Lima et al., 2017). Macrocysts are another specialized variety of encystation that include multiple individuals in macrocysts the social amoebae Dictyostelium or are polynuclear from the syncytial Arboramoeba and relatives (Berney et al., 2015; Mehdiabadi et al., 2010; Romeralo et al., 2012). In Dictyostelid amoebae, macrocysts are also used in sexual

reproduction (Mehdiabadi et al., 2010; Romeralo et al., 2012). We identified cysts in numerous strains, including spherical cysts in Vahlkampfia and relatives (1.3A), the polyhedral cysts of our Nuclearia isolate (1.3B), pseudocysts in Flabellula, (1.3C) and giant macrocysts in *Filoreta* (1.3D). The longevity of cysts in these strains was assessed and amoebae excysted successfully after more than two years of incubation in sterile medium at room temperature.

Fixation of marine amoebae: why it is important to optimize for the cytoskeleton?

To better understand the underlying mechanisms driving pseudodpodial morphology, it is important to directly visualize the organization of the cytoskeleton. In non-model systems whose cytoskeletal proteins are not able to be directly tagged with fluorescent proteins, fixation and immunofluorescence is an invaluable tool. Like taxidermy, fixation is a way of preserving morphology of a cell in a life-like form for further observation. Also, like taxidermy, a bad fixation alters structural features, causing problems with morphological interpretations.

Amoeboid cells often are negatively affected by the fixation process because they don't have cell walls or other rigid structures to help maintain their shape. During fixation, amoebae can often round up, bleb, form beaded appearances, and lose fine features like lamellipodial ruffles and narrow filopodial projections. At the protein level, preserving structure is important to be able to stain with antibodies; no preserved structure, no epitope to bind and label.

Over-fixed cells can also become autofluorescent and limit the localization of antibodies to proteins of interest. When autofluorescence is present, additional quenching may be required (i.e., addition of 0.2M Glycine for 1 hour at room temperature, or a reducing agent like 1mg/ml sodium borohydride on ice for an hour) (Clancy and Cauller, 1998). However, under-fixed cells present a different set of problems as they are extremely fragile and will be lost during the multistep process of immunostaining.

There are numerous ways to fix cells, and optimal fixative concentrations depend on many factors including their morphology and the proteins of interest to be labeled. For example, glyoxal is a fixative that works very well for preserving the delicate microtubule cytoskeleton of *Filoreta sp.*, but does not preserve F-actin structure, and staining with Phalloidin conjugates yields no discernible pseudopodial morphology. Ethanol and methanol similarly do not preserve actin structure. Paraformaldehyde typically preserves actin very well, but microtubules often appeared fragmented in these samples. Glutaraldehyde fixes cells fast enough to preserve both actin and microtubules, but must undergo additional quenching steps are required in order to reduce autofluorescence.

It is also important to pre-wash with calcium-free seawater when fixing marine amoebae. During fixation, calcium in solution simultaneously rushes into the cell as the membrane becomes fixed, causing the cells to swell and lose their shape (Bowser and Travis, 2000). The presence of excess calcium also affects the structure of both actin and microtubule cytoskeletal polymers (Bowser and Travis, 2000; O'Brien et al., 1997; Wales et al., 2016). There are additives that can improve the efficacy of fixative solution, including cytoskeleton stabilizing buffers and osmolarity-adjustments with sucrose. These work to adjust the osmolarity of the fixative to prevent cell deformation and protect the cytoskeletal proteins and limit their depolymerization during fixation, while also enhancing the fixative crosslinking activity (Hua and Ferland, 2017). Most cytoskeleton stabilizing buffers include EGTA, a calcium chelator. Sucrose has been shown in delicate fixation of retinal neurons to prevent beading and loss of shape (Stradleigh et al., 2015). Optimal fixation in any case is crucial to accurate visualization of structures in order to study the cell's morphological features.

There is a need for more diverse cell biological models to study cytoskeletal evolution.

All of the amoeboid morphotypes use cytoskeletal rearrangements and polymer turnover to regulate and change shape, generating forces for adhesion, locomotion, and engulfing or piercing their prey. The amoeboid cytoskeleton is therefore an important feature for understanding the evolution of extant eukaryotic supergroups and their cellular processes involved in cell shape and locomotion. Are the morphological similarities of amoebae across the eukaryotic tree conserved or convergent morphotypes? Morphologies within lineages can vary widely, indicating diverse mechanisms for the evolution of morphotypes even within more closely related clades. The strains generated in this study may be useful in uncovering conserved mechanisms across eukaryotes; particularly in *Filoreta* and *Cunea* strains, whose genomes have been fully sequenced (Chapter 2). Additional genome coverage of diverse amoeboid lineages are needed for pursuing evolutionary cell biology, highlighting the importance of generating cultivable laboratory strains of free-living amoeboid protists. Genome content can be used in tandem with cell biological approaches to better understand the conserved or divergent mechanisms driving pseudopod formation, force generation and motility.

Methods

Isolation of "food" bacteria

During the initial bacterial bloom of enrichment of amoebae in flasks, plastic sterile loops were used to streak bacteria onto a Marine Amoeba Agar (MAA) plate (containing Seawater Base (SWB: 342.2 mM NaCl, 14.8 mM MgSO4*6H2O, 6.71 mM KCl, 9.0 mM CaCl) 0.1% Yeast Extract, 0.1% Tryptone, 5mM MOPS pH 7.0, 1.0% Bacto Agar). We selected strains based on size, motility, lawn formation and absence of clumping under wet mount. A colony was selected that exhibited gliding motility and distributed evenly over the MAA culture surface. The isolate

was prepared for colony PCR by boiling in ALP and the 16S rRNA gene was amplified with bacteria-specific primers (8F=AGAGTTTGATCCTGGCTCAG, 1391R=GACGGGCGGTGWGTRCA) and sequenced using 515F primer (GTGCCAGCMGCCGCGGTAA). The strain belonged to the genus *Maribacter,* determined by SSU rRNA alignment. This strain was used to isolate marine amoebae on MAA.

For freshwater "food" bacteria, we isolated using the same methods as described above, by streaking onto Freshwater Amoeba Agar (FAA) (containing Freshwater Base (FWB), 0.1% Yeast Extract, 0.1% Tryptone, 1.0% Bacto Agar and 5 mM MOPS pH 7.0) FWB was prepared as modular media in five 200-ml stock solutions containing: 2.4 g NaCl, 0.1 g $MgS0_4 \bullet 6H_20$, 0.1 g $CaCl_2 \bullet 2H_20$, 2.84 g Na_2HP0_4 and 2.72 g KH_2P0_4. To make one liter of FWB, 10 ml of each of the five stock solutions were added, (final concentration of 2.2 mM NaCl, 22 µM $MgS0_4 \bullet 6H_20$, 34 µM $CaCl_2 \bullet 2H_20$, 1 mM Na_2HP0_4, 1 mM KH_2P0_4). Bacteria on FAA were selected with the same parameters as described above. Most species that grew were small, motile bacteria identified by SSU rRNA to be *Pseudomonas* spp. and were used to isolate freshwater amoebae on FAA.

Amoeba cultivation

Marine and brackish environmental samples were collected from organic and sulfidic sediments found in intertidal zones in the Little Sippewissett Marsh (SW, SP, PL, L, P) and Trunk River Lagoon (TR) near Woods Hole, Massachusetts, and in marshlands bordering Bodega Bay (BA, BB) in California. Freshwater samples were collected from a variety of natural sources in Northern California (Putah Creek, (PCr); Vic Fazio Causeway (CW); Hay infusion from UC Davis teaching laboratories (Hay), algal biofilms growing on concrete flooring of a patio (PA) and greenhouse (GH) in Davis, California), Southern California (Waterman Canyon Creek,

(WC)), seasonal pools and creek beds near Las Vegas, Nevada (Black Corridor (BC), Sandstone Quarry (SQ)).

Samples categorized as “marine” or “freshwater” used SWB or FWB and MAA or FAA plates, respectively. Samples were observed microscopically prior to processing, and any that contained numerous active amoebae were immediately used in plaque isolation. Samples that did not have abundant amoebae were enriched as follows: approximately 1 ml volume of organic material in suspension from each environmental sample was added to a T25 flask with SWB/FWB and 0.01% filter-sterilized Yeast Extract and Tryptone (YET). Flasks were grown at room temperature and monitored with a Nikon TS100 phase contrast inverted microscope until numerous amoebae were present. Upon observing adequate growth, culture surfaces were scraped with a cell scraper (GeneMate) and 100 µl of the suspension was transferred for serial dilution.

Cell suspensions were serially diluted into 1:10, 1:50 and 1:100 in microfuge tubes with SWB/FWB, inverting several times between each dilution to mix. Each dilution was then plated by adding 100 µl of sample to 100 µl of food bacteria (diluted to approximately 0.5 McFarland density) and spread-plating onto the agar surface using metal flame-sterilized cell spreader. The plates were sealed with parafilm to preserve moisture and incubated at room temperature. Bacterial lawns were monitored daily for changes in texture and plaque formation. When plaques were visible, presence of amoebae were verified microscopically. Isolated, non-overlapping plaques containing active amoebae were gently scraped with a sterile plastic loop (Thermo Nunc), resuspended in SWB/FWB, and serially diluted as before to create secondary isolations.

Secondary plaques were then harvested and transferred into T25 culture flasks containing 10 ml of SWB/FWB, 5 mM MOPS pH 7.0, 0.01% YET, filter sterilized. Bacteria that were transferred

from plates were presumably a mixture of isolated “food bacteria” and any bacteria originally present in the environmental samples in close association with the amoebae. The T25 flasks were monitored using an inverted phase contrast microscope at the 24 hour timepoint to ensure purity, and observe growth rate and morphology.

Non-adherent amoebae

Enrichments of green cyanobacterial mats from Sippewissett Marsh produced planktonic non-adherent amoebae exhibiting axopodia that fed on cyanobacteria. These amoebae did not grow on plates. Attempts to isolate axopodial amoebae entailed dilution to extinction in 96-well plates, and cell sorting using a Wolf Benchtop microfluidic cell sorter (NanoCellect). Flow-sorting gates were selected using high autofluorescence with red and green laser lines, and high backscatter for size approximation. The sorted fractions were maintained by adding 0.1% filter-sterilized spinach puree (equal w/v leaf to distilled water, blended to liquid consistency, then sequentially filtered from 50 μm to 5 μm, to 0.22 μm), rather than bacterial prey.

Live imaging

Amoebae were grown in flasks as described above, briefly washed in SWB/FWB to remove excess bacteria, scraped with cell scrapers, and transferred to Mattek dishes or 96-well glass-bottom plates. They were allowed to adhere for 30 minutes, then imaged on a Nikon Eclipse TS100 equipped with phase contrast and Qimaging Retiga 2000R CCD camera, or on a Leica DMI 6000B with differential interference contrast (DIC) and a Prime 95B sCMOS camera. Frame intervals were set to 1 second, with camera exposures from 100ms to 500 ms under low light settings. Images were background cleaned in FIJI, where a duplicate image is Gaussian blurred, then divided against the original image to remove artifact background shading.

gDNA isolation

Amoebae were clonally maintained and expanded into T75 flasks containing 50 ml of SWB/FWB to increase cell number. When cultures were at peak density, genomic DNA was extracted using a modified phenol:chloroform extraction as follows. Flask culture surfaces were briefly rinsed with sterile SWB/FWB to remove excess bacterial cells and decanted, refilling with 10 ml of sterile SWB/FWB. Amoebae were harvested from flasks using cell scraper, transferred into 15-ml conical tubes (Corning) and centrifuged for 5 minutes at 2000 x g at 4°C. The supernatant was removed and cell pellets (approximately 1 ml) were transferred into microfuge tubes. A mixture of 500µl 2X Buffer A, 60µl Proteinase K, 10µl SDS (20%) was added to the cells, briefly vortexed, and incubated for 30 minutes at 50°C.

For each strain,1 ml of lysis mixture was added a bead beating tube (Sarstedt 72.693.005) containing 0.3g of acid-washed zirconium beads (BioSpec #11079105z), 500 µl phenol:chloroform:IAA (25:24:1), 200µl SDS (20%), then beat at 2500 rpm for 2 minutes in a mini bead beating machine (Cole-Parmer). The tubes were centrifuged at 16000 x g for 3 minutes, and the aqueous layer was transferred to new microfuge tubes before secondary extraction in equal volumes of chloroform:IAA (24:1). The supernatant (500 µl) was transferred to new microfuge tubes and precipitated with equal volume (500 µl) of isopropanol and 0.1 volume (50 µl) of 0.3 M sodium acetate (pH 5.2) on ice for 20 minutes. Precipitates were pelleted by centrifugation at 16000 x g for 10 minutes at 4°C. The supernatant was removed, and pellets were washed in 500 µl of cold 80% ethanol, centrifuged at 16000 x g for 5 minutes, then air-dried for 20 minutes at room temperature. The pelleted DNA was resuspended in 20 µl of nuclease-free H2O.

Ssu rRNA sequencing

The V2-7 regions of the isolates' 18S SSU rRNA gene were amplified using combinations from four universal eukaryote-specific primers: (Forward) 82FE = GAADCTGYGAAYGGCTC; (Forward) 360FE = CGGAGARGGMGCMTGAGA; (Reverse) 1391RE = GGGCGGTGTGTACAARGR; (Reverse) 1200RE = GGRCATCACDGACCTG. (Dawson 2002). Fragments were amplified from total gDNA using Easy-A High-Fidelity PCR Master Mix (Agilent Catalog #600640) in 25 µl reactions. Amplification was carried out with initial 5 minutes at 94°C, followed by 30 cycles of: [1 minute at 94°C, 1 minute at 55°C, 4 minutes at 72°C], and a final 10 minute extension at 72°C. PCR products were visualized by gel electrophoresis before cleanup using Exo-SAP (78 µl nuclease-free water, 2 µl Exonuclease 1 (Amersham Bio E70073X) 20 µl Shrimp Alkaline Phosphatase (Amersham Bio E70092X)). Products were sequenced with 1200R primer by the UC Berkeley DNA sequencing facility. For strains whose PCR products did not yield quality sequencing or did not generate single bands (a potential problem with heterogenous fragment mixture), the amplified fragments were inserted into a cloning vector using topoisomerase-based cloning procedures (TOPO-cloned) to isolate clonally propagated PCR products (Invitrogen). Colonies that grew from this protocol were selected and plasmids were extracted by miniprep (Qiagen) and sequenced with M13 forward primer by the UC Berkeley DNA sequencing facility.

Fixation optimization for marine amoebae

Fixation of marine amoebae required iterative optimization (Figure 2). The exceptionally delicate marine isolate "SW4B" was used in the optimization to design fixation procedures that would work for most amoebae. Example fixation methods were used from existing literature (Bowser

and Travis, 2000; Richter et al., 2018; Wheatley and Wang, 1998; Whelan and Bell, 2015) and were modified iteratively using ranges of fixatives, their concentrations, buffers, additives and salinity. All fixation attempts were used on amoebae adhered to coverslips pre-coated with either 0.1% poly-L-lysine, or 0.1% cold water fish skin (Sigma). Coverslips were placed in a sterile petri dish and covered with either 0.1% solution, allowed to sit for 10 minutes at room temperature, and the solution removed. The coverslips were then dried completely and used within 24 hours. Amoebae from active cultures were scraped and added to coverslips in 8-well dishes (Thermo 267062), allowed to adhere and grow their reticulopodia (1-6 hours) prior to fixation attempt. In all cases, the SWB medium was replaced with CFSW (see Appendix) for 2-5 minutes immediately prior to fixation. Cultures were previously monitored for 2 hours to ensure morphology was not perturbed by this substitution. Fixative solutions were tested with ranges of 0.5-5% Paraformaldehyde, 0.1-2% Glutaraldehyde, 1-6% glyoxal, and contained a range of sucrose (0.1-0.5M), CFSW (0.5X-2X) CSB (0.25X-5X) (see Appendix) for 10 seconds to 30 minutes at room temperature.

Preservation of overall structure was verified using a phase contrast microscope before proceeding to the permeabilization and immunostaining process. Samples whose structure was disrupted were discarded, and samples with life-like structure were immunostained to visualize adequate preservation of the microtubule and actin network. See Appendix for examples of optimized fixation protocol.

Literature Cited

Berney C, Geisen S, Van Wichelen J, Nitsche F, Vanormelingen P, Bonkowski M, Bass D. 2015. Expansion of the 'Reticulosphere': Diversity of Novel Branching and Network-forming Amoebae Helps to Define Variosea (Amoebozoa). *Protist* **166**:271–295. doi:10.1016/j.protis.2015.04.001

Bonner JT. 2003. On the origin of differentiation. *J Biosci* **28**:523–528. doi:10.1007/BF02705126

Bowser SS, Travis JL. 2000. Methods for Structural Studies of Reticulopodia, the Vital Foraminiferal "Soft Part." *Micropaleontology* **46**:47–56.

Bozzaro S. 2019. The past, present and future of Dictyostelium as a model system. *Int J Dev Biol* **63**:321–331. doi:10.1387/ijdb.190128sb

Brown MW, Kolisko M, Silberman JD, Roger AJ. 2012a. Aggregative Multicellularity Evolved Independently in the Eukaryotic Supergroup Rhizaria. *Current Biology* **22**:1123–1127. doi:10.1016/j.cub.2012.04.021

Brown MW, Silberman JD, Spiegel FW. 2012b. A contemporary evaluation of the acrasids (Acrasidae, Heterolobosea, Excavata). *European Journal of Protistology*, ECOP 2011 **48**:103–123. doi:10.1016/j.ejop.2011.10.001

Burki F, Roger AJ, Brown MW, Simpson AGB. 2020. The New Tree of Eukaryotes. *Trends in Ecology & Evolution* **35**:43–55. doi:10.1016/j.tree.2019.08.008

Charras GT, Hu C-K, Coughlin M, Mitchison TJ. 2006. Reassembly of contractile actin cortex in cell blebs. *J Cell Biol* **175**:477–490. doi:10.1083/jcb.200602085

Chhabra ES, Higgs HN. 2007. The many faces of actin: matching assembly factors with cellular structures. *Nat Cell Biol* **9**:1110–1121. doi:10.1038/ncb1007-1110

Clancy B, Cauller LJ. 1998. Reduction of background autofluorescence in brain sections following immersion in sodium borohydride. *J Neurosci Methods* **83**:97–102. doi:10.1016/s0165-0270(98)00066-1

Fouque E, Trouilhé M-C, Thomas V, Hartemann P, Rodier M-H, Héchard Y. 2012. Cellular, Biochemical, and Molecular Changes during Encystment of Free-Living Amoebae. *Eukaryot Cell* **11**:382–387. doi:10.1128/EC.05301-11

Fritz-Laylin LK. 2020. The evolution of animal cell motility. *Current Biology* **30**:R477–R482. doi:10.1016/j.cub.2020.03.026

Fritz-Laylin LK, Lord SJ, Kakley M, Mullins RD. 2018. Concise language promotes clear thinking about cell shape and locomotion. *Bioessays* **40**:e1700225. doi:10.1002/bies.201700225

Fritz-Laylin LK, Riel-Mehan M, Chen B-C, Lord SJ, Goddard TD, Ferrin TE, Nicholson-Dykstra SM, Higgs H, Johnson GT, Betzig E, Mullins RD. 2017. Actin-based protrusions of migrating neutrophils are intrinsically lamellar and facilitate direction changes. *eLife* **6**:e26990. doi:10.7554/eLife.26990

Garajová M, Mrva M, Vaškovicová N, Martinka M, Melicherová J, Valigurová A. 2019. Cellulose fibrils formation and organisation of cytoskeleton during encystment are essential for Acanthamoeba cyst wall architecture. *Sci Rep* **9**:4466. doi:10.1038/s41598-019-41084-6

Gast RJ. 2017. Centrohelida and Other Heliozoan-Like Protists In: Archibald JM, Simpson AGB, Slamovits CH, editors. Handbook of the Protists. Cham: Springer International Publishing. pp. 955–971. doi:10.1007/978-3-319-28149-0_28

Goodson HV, Kelley JB, Brawley SH. 2021. Cytoskeletal diversification across 1 billion years: What red algae can teach us about the cytoskeleton, and vice versa. *Bioessays* **43**:e2000278. doi:10.1002/bies.202000278

Houdusse A, Titus MA. 2021. The Many Roles of Myosins in Filopodia, Microvilli and Stereocilia. *Curr Biol* **31**:R586–R602. doi:10.1016/j.cub.2021.04.005

Hua K, Ferland RJ. 2017. Fixation methods can differentially affect ciliary protein immunolabeling. *Cilia* **6**:5. doi:10.1186/s13630-017-0045-9

Innocenti M. 2018. New insights into the formation and the function of lamellipodia and ruffles in mesenchymal cell migration. *Cell Adh Migr* **12**:401–416. doi:10.1080/19336918.2018.1448352

Jaške K, Barcytė D, Pánek T, Ševčíková T, Eliášová A, Eliáš M. 2022. The net-like heterotrophic amoeba Leukarachnion salinum sp. nov. (Ochrophyta, Stramenopiles) has a cryptic plastid. doi:10.1101/2022.04.05.487141

Kang S, Tice AK, Spiegel FW, Silberman JD, Pánek T, Čepička I, Kostka M, Kosakyan A, Alcântara DMC, Roger AJ, Shadwick LL, Smirnov A, Kudryavtsev A, Lahr DJG, Brown MW. 2017. Between a Pod and a Hard Test: The Deep Evolution of Amoebae. *Molecular Biology and Evolution* **34**:2258–2270. doi:10.1093/molbev/msx162

Kopf A, Renkawitz J, Hauschild R, Girkontaite I, Tedford K, Merrin J, Thorn-Seshold O, Trauner D, Häcker H, Fischer K-D, Kiermaier E, Sixt M. 2020. Microtubules control cellular shape and coherence in amoeboid migrating cells. *J Cell Biol* **219**:e201907154. doi:10.1083/jcb.201907154

Krabberød AK, Orr RJS, Bråte J, Kristensen T, Bjørklund KR, Shalchian-Tabrizi K. 2017. Single Cell Transcriptomics, Mega-Phylogeny, and the Genetic Basis of Morphological Innovations in Rhizaria. *Mol Biol Evol* **34**:1557–1573. doi:10.1093/molbev/msx075

Lima PC, Taylor RS, Cook M. 2017. Pseudocyst formation in the marine parasitic amoeba Neoparamoeba perurans: a short-term survival strategy to abrupt salinity variation. *Journal of Fish Diseases* **40**:1109–1113. doi:10.1111/jfd.12588

Liu Z, Hu SK, Campbell V, Tatters AO, Heidelberg KB, Caron DA. 2017. Single-cell transcriptomics of small microbial eukaryotes: limitations and potential. *ISME J* **11**:1282–1285. doi:10.1038/ismej.2016.190

Maroto R, Hamill OP. 2007. Chapter 17 - MscCa Regulation of Tumor Cell Migration and Metastasis In: Hamill OP, editor. Current Topics in Membranes, Mechanosensitive Ion Channels, Part B. Academic Press. pp. 485–509. doi:10.1016/S1063-5823(06)59019-2

Mattila PK, Lappalainen P. 2008. Filopodia: molecular architecture and cellular functions. *Nat Rev Mol Cell Biol* **9**:446–454. doi:10.1038/nrm2406

Medina EM, Robinson KA, Bellingham-Johnstun K, Ianiri G, Laplante C, Fritz-Laylin LK, Buchler NE. 2020. Genetic transformation of Spizellomyces punctatus, a resource for studying chytrid biology and evolutionary cell biology. *eLife* **9**:e52741. doi:10.7554/eLife.52741

Mehdiabadi NJ, Kronforst MR, Queller DC, Strassmann JE. 2010. Phylogeography and sexual macrocyst formation in the social amoeba Dictyostelium giganteum. *BMC Evolutionary Biology* **10**:17. doi:10.1186/1471-2148-10-17

O'Brien ET, Salmon E d., Erickson HP. 1997. How calcium causes microtubule depolymerization. *Cell Motility* **36**:125–135. doi:10.1002/(SICI)1097-0169(1997)36:2<125::AID-CM3>3.0.CO;2-8

Oettmeier C, Nakagaki T, Döbereiner H-G. 2020. Slime mold on the rise: the physics of Physarum polycephalum. *J Phys D: Appl Phys* **53**:310201. doi:10.1088/1361-6463/ab866c

Ondracka A, Dudin O, Ruiz-Trillo I. 2018. Decoupling of Nuclear Division Cycles and Cell Size during the Coenocytic Growth of the Ichthyosporean Sphaeroforma arctica. *Curr Biol* **28**:1964-1969.e2. doi:10.1016/j.cub.2018.04.074

Patino-Ramirez F, Arson C, Dussutour A. 2021. Substrate and cell fusion influence on slime mold network dynamics. *Sci Rep* **11**:1498. doi:10.1038/s41598-020-80320-2

Pawlowski J, Burki F. 2009. Untangling the phylogeny of amoeboid protists. *J Eukaryot Microbiol* **56**:16–25. doi:JEU379 [pii] 10.1111/j.1550-7408.2008.00379.x

Petrie RJ, Yamada KM. 2012. At the leading edge of three-dimensional cell migration. *J Cell Sci* **125**:5917–5926. doi:10.1242/jcs.093732

Pollard TD, Borisy GG. 2003. Cellular Motility Driven by Assembly and Disassembly of Actin Filaments. *Cell* **112**:453–465. doi:10.1016/S0092-8674(03)00120-X

Richter KN, Revelo NH, Seitz KJ, Helm MS, Sarkar D, Saleeb RS, D'Este E, Eberle J, Wagner E, Vogl C, Lazaro DF, Richter F, Coy-Vergara J, Coceano G, Boyden ES, Duncan RR, Hell SW, Lauterbach MA, Lehnart SE, Moser T, Outeiro TF, Rehling P, Schwappach B, Testa I, Zapiec B, Rizzoli SO. 2018. Glyoxal as an alternative fixative to formaldehyde in immunostaining and super-resolution microscopy. *EMBO J* **37**:139–159. doi:10.15252/embj.201695709

Romeralo M, Escalante R, Baldauf SL. 2012. Evolution and Diversity of Dictyostelid Social Amoebae. *Protist* **163**:327–343. doi:10.1016/j.protis.2011.09.004

Ruiz-Trillo I, Inagaki Y, Davis LA, Sperstad S, Landfald B, Roger AJ. 2004. Capsaspora owczarzaki is an independent opisthokont lineage. *Current Biology* **14**:R946–R947. doi:10.1016/j.cub.2004.10.037

Schick J, Raz E. 2022. Blebs—Formation, Regulation, Positioning, and Role in Amoeboid Cell Migration. *Front Cell Dev Biol* **10**:926394. doi:10.3389/fcell.2022.926394

Siddiqui R, Khan NA. 2012. Biology and pathogenesis of Acanthamoeba. *Parasites & Vectors* **5**:6. doi:10.1186/1756-3305-5-6

Smirnov A, Brown S. 2004. Guide to the methods of study and identification of soil gymnamoebae. *Protistology* **3**:148–190.

Smirnov A, Nassonova E, Geisen S, Bonkowski M, Kudryavtsev A, Berney C, Glotova A, Bondarenko N, Dyková I, Mrva M, Fahrni J, Pawlowski J. 2017. Phylogeny and Systematics of Leptomyxid Amoebae (Amoebozoa, Tubulinea, Leptomyxida). *Protist* **168**:220–252. doi:10.1016/j.protis.2016.10.006

Sriram R, Shoff M, Booton G, Fuerst P, Visvesvara GS. 2008. Survival of Acanthamoeba Cysts after Desiccation for More than 20 Years. *J Clin Microbiol* **46**:4045–4048. doi:10.1128/JCM.01903-08

Steffen A, Faix J, Resch GP, Linkner J, Wehland J, Small JV, Rottner K, Stradal TEB. 2006. Filopodia Formation in the Absence of Functional WAVE- and Arp2/3-Complexes. *Mol Biol Cell* **17**:2581–2591. doi:10.1091/mbc.E05-11-1088

Stockem W, Hoffmann H-U, Gruber B. 1983. Dynamics of the cytoskeleton in Amoeba proteus. *Cell Tissue Res* **232**:79–96. doi:10.1007/BF00222375

Stradleigh TW, Greenberg KP, Partida GJ, Pham A, Ishida AT. 2015. Moniliform deformation of retinal ganglion cells by formaldehyde-based fixatives. *J Comp Neurol* **523**:545–564. doi:10.1002/cne.23689

Strassmann JE, Shu L. 2017. Ancient bacteria–amoeba relationships and pathogenic animal bacteria. *PLoS Biol* **15**:e2002460. doi:10.1371/journal.pbio.2002460

Tekle YI, Grant JR, Kovner AM, Townsend JP, Katz LA. 2010. Identification of new molecular markers for assembling the eukaryotic tree of life. *Mol Phylogenet Evol* **55**:1177–82. doi:S1055-7903(10)00108-9 [pii] 10.1016/j.ympev.2010.03.010

Tekle YI, Williams JR. 2016. Cytoskeletal architecture and its evolutionary significance in amoeboid eukaryotes and their mode of locomotion. *Royal Society Open Science* **3**:160283. doi:10.1098/rsos.160283

Tice AK, Brown MW. 2022. Multicellularity: Amoebae follow the leader to food. *Current Biology* **32**:R418–R420. doi:10.1016/j.cub.2022.03.067

Tilney LG, Porter KR. 1965. Studies on microtubules in Heliozoa I. *Protoplasma* **60**:317–344. doi:10.1007/BF01247886

Wales P, Schuberth CE, Aufschnaiter R, Fels J, García-Aguilar I, Janning A, Dlugos CP, Schäfer-Herte M, Klingner C, Wälte M, Kuhlmann J, Menis E, Hockaday Kang L, Maier KC, Hou W, Russo A, Higgs HN, Pavenstädt H, Vogl T, Roth J, Qualmann B, Kessels MM, Martin DE, Mulder B, Wedlich-Söldner R. 2016. Calcium-mediated actin reset (CaAR) mediates acute cell adaptations. *eLife* **5**:e19850. doi:10.7554/eLife.19850

Wheatley SP, Wang Y. 1998. Chapter 18 Indirect Immunofluorescence Microscopy in Cultured CellsMethods in Cell Biology. Elsevier. pp. 313–332. doi:10.1016/S0091-679X(08)61588-5

Whelan DR, Bell TDM. 2015. Image artifacts in Single Molecule Localization Microscopy: why optimization of sample preparation protocols matters. *Sci Rep* **5**:7924. doi:10.1038/srep07924

Table 1.1: Isolates sequenced from the amoeba collection

Clade	Genus	Culture Type	Strain ID		Sample Location	Nucleotide #	% Similarity
Amoebozoa	*Cunea*	Marine	L3A	*	Sippewissett Marsh, MA	444	97.30%
			L3B	*	Sippewissett Marsh, MA	1217	96.64%
			L11A		Sippewissett Marsh, MA	1298	97.38%
	Pseudoparamoeba	Marine	L17A		Sippewissett Marsh, MA	1459	97.4%
			L17B		Sippewissett Marsh, MA	606	95.24%
	Neoparamoeba	Marine	KCPV1		Sippewissett Marsh, MA	1083	98.07%
	Acanthamoeba	Freshwater	CW1C2	*	Vic Fazio Causeway, CA	1398	99.64%
			CW3C4		Vic Fazio Causeway, CA	1401	99.07%
			WCC1		Waterman Canyon, CA	1049	99.14%
			WCC2		Waterman Canyon, CA	1019	98.92%
			WCB3		Waterman Canyon, CA	749	99.73%
	Vexillifera	Marine	SW5A		Sippewissett Marsh, MA	1014	96.96%
			SW5D		Sippewissett Marsh, MA	1102	97.12%
			SWM1	*	Sippewissett Marsh, MA	1120	96.67%
	Ripella	Freshwater	GH51		Greenhouse Biofilm	965	94.29%
	Stenamoeba	Freshwater	HayB1	*	Hay Infusion	1095	93.81%
			PatioB1		Patio Biofilm	979	95.43%
			PatioC1C3		Patio Biofilm	971	98.97%
			PatioF1C2		Patio Biofilm	950	98.74%
	Vermamoeba	Freshwater	CW2C2		Vic Fazio Causeway, CA	835	99.4%
			GH2C1	*	Greenhouse Biofilm	407	99.51%
			HayD1C4		Hay Infusion	1020	99.22%
			SQ2A		Sandstone Quarry, NV	940	99.89
			SQ2B		Sandstone Quarry, NV	1009	99.90%
	Flabellula	Marine	BBWNBr	*	Bodega Bay, CA	350	88.03%
			TRVerF	*	Trunk River, MA	1011	99.70%
			TRKR6		Trunk River, MA	723	99.45%
Heterolobosea	*Neovahlkampfia*	Marine	P4A		Sippewissett Marsh, MA	860	93.41%
			P4C		Sippewissett Marsh, MA	1044	97.86%
			P4D		Sippewissett Marsh, MA	1042	97.86%
			P7A		Sippewissett Marsh, MA	879	92.95%
			P7B		Sippewissett Marsh, MA	1003	93.64%
			P8A		Sippewissett Marsh, MA	1043	95.38%
			P8B		Sippewissett Marsh, MA	820	97.78%
			P9A		Sippewissett Marsh, MA	1066	97.53%
			P9B		Sippewissett Marsh, MA	980	95.38%
			P12A	*	Sippewissett Marsh, MA	1051	97.86%
			SP6A	*	Sippewissett Marsh, MA	1036	95.38%
			SPM1		Sippewissett Marsh, MA	1030	95.38%
			SPM2		Sippewissett Marsh, MA	1171	95.23
	Vahlkampfia	Freshwater	CW2C1	*	Vic Fazio Causeway, CA	900	99.56%
			CW2C3		Vic Fazio Causeway, CA	916	99.78%
			CW3C1		Vic Fazio Causeway, CA	912	99.89%
			CW3C2		Vic Fazio Causeway, CA	807	98.64%
			CW3C3		Vic Fazio Causeway, CA	938	99.47%
			HayB2	*	Hay Infusion	1215	99.67%
			HayE1		Hay Infusion	1030	99.61%
			ISA		Ice Scoop Biofilm	873	99.71%
			PatioA1		Patio Biofilm	1033	99.71%
			PatioA2		Patio Biofilm	1005	99.50%
			PatioE1C1		Patio Biofilm	374	96.12%
	Naegleria	Freshwater	PCr1		Putah Creek, CA	1014	99.90%
			PCrA		Putah Creek, CA	983	99.69%
			PCrB		Putah Creek, CA	978	99.59%
			BC1A	*	Black Corridor, NV	1087	99.82%
	Tetramitus	Freshwater	WCA1		Waterman Canyon, CA	954	99.58%
			WCA2	*	Waterman Canyon, CA	1032	99.81%
			WCB2		Waterman Canyon, CA	542	99.63
			WCE1		Waterman Canyon, CA	1035	99.61%
			WCE2		Waterman Canyon, CA	1016	99.80%
Rhizaria	*Filoreta*	Marine	SW1A		Sippewissett Marsh, MA	961	98.54%
			SW4B	*	Sippewissett Marsh, MA	659	86.80%
			SW7C		Sippewissett Marsh, MA	1054	98.58%
			TRFil		Trunk River, MA	804	95.17%
			BBFil		Bodega Bay, CA	299	99.00%
	Massisteria	Marine	BBHelio1	*	Bodega Bay, CA	1060	99.43%
	Spongomonas	Freshwater	PatioD1C1	*	Patio Biofilm	1111	99.82%
Opisthokonta	*Nuclearia*	Freshwater	GHFC1	*	Greenhouse Biofilm	413	90.38%
Undetermined	Undetermined	Marine	P1A		Sippewissett Marsh, MA	1007	< 80%
			P1D		Sippewissett Marsh, MA	1172	< 80%
			P5A	*	Sippewissett Marsh, MA	1322	< 80%
			P5B		Sippewissett Marsh, MA	1274	< 80%
			P5C		Sippewissett Marsh, MA	825	< 80%
			PL2A		Sippewissett Marsh, MA	1111	< 80%
			SW10A	*	Sippewissett Marsh, MA	1004	< 82%
			SW10D		Sippewissett Marsh, MA	1161	< 82%
			SW3B		Sippewissett Marsh, MA	1309	< 80%
			SW7B		Sippewissett Marsh, MA	654	< 82%
		Freshwater	M105	*	Greenhouse Biofilm	1253	< 86%

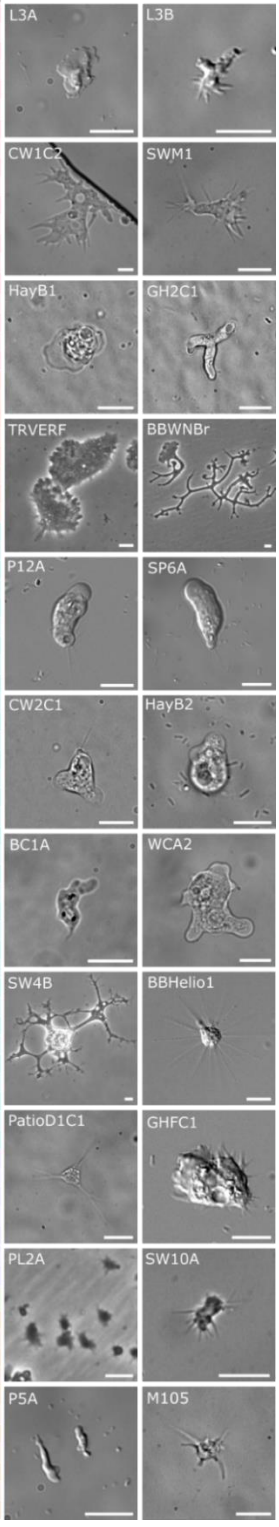

Table of free-living amoebae isolated in this study, color-coded by major eukaryotic clade, and categorized by genera and environmental sample type/location. Strain identities organized by percent similarity over nucleotide length sequenced. Strain IDs with asterisks are shown in images to the right. Scale bars = 10 µm.

Figure 1.1: Diverse amoeba isolated across the eukaryotic tree

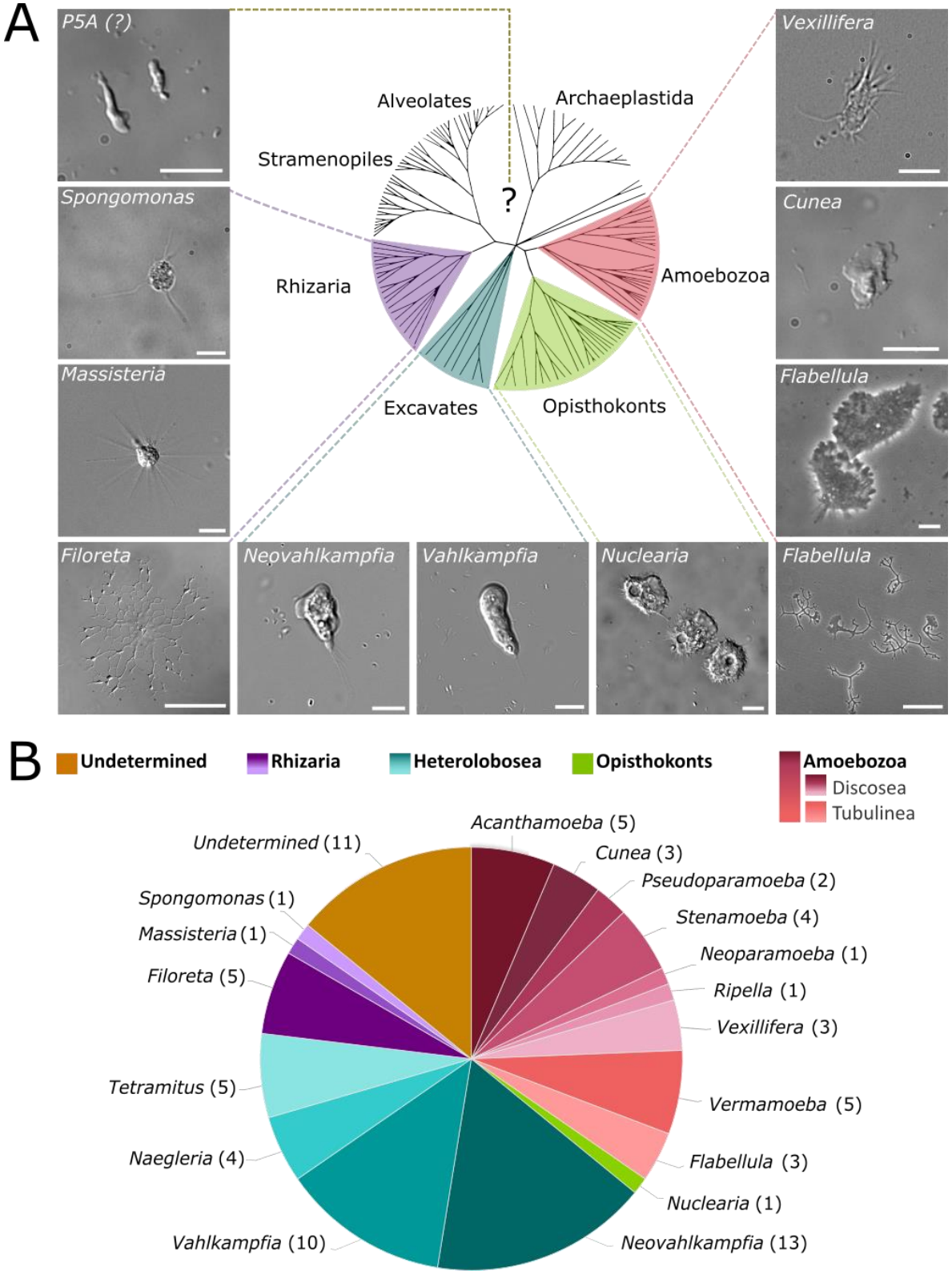

(A) A simplified tree of eukaryotes, showing major groups in which isolates were identified, with representative images of genera and pseudopodia observed in each strain.

P5A (undetermined lineage) with lobopodia and blebbing motility. Scale = 10 µm.

Spongomonas (Rhizaria; Cercozoa) with filopodia. Scale = 10 µm.

Massisteria (Rhizaria; Cercozoa) with axopodia. Scale = 10 µm.

Filoreta (Rhizaria; Cercozoa) with reticulopodia, filopodia and lamellipodia. Scale = 100 µm.

Neovahlkampfia (Excavates; Heterolobosea) with blebbing motility. Scale = 10 µm.

Vahlkampfia (Excavates; Heterolobosea) with blebbing motility. Scale = 10 µm.

Nuclearia (Opisthokonts) with filopodia and lamellipodia. Scale = 10 µm.

Flabellula (Amoebozoa; Tubulinea) (bottom right) isolate "BBWNBr" with low similarity (88%) exhibiting branched morphology with lamellipodia, filopodia and reticulopodia. Scale = 100 µm.

Flabellula (above) isolate with high similarity (99%) exhibiting filopodia and lamellipodia. Scale = 10 µm.

Cunea (Amoebozoa; Discosea) with lamellipodia and lobopodia. Scale = 10 µm.

Vexillifera (Amoebozoa; Discosea) with filopodia. Scale = 10 µm.

(B) A pie chart quantifying the isolates per eukaryotic lineage (color coded). Undetermined lineages include strains whose SSU sequences were less than 85% similarity to nearest monophyletic clade.

Figure 1.2: Pseudopodial morphotypes measured by isolate number

A

Pseudopod Type	Genus	# Genera	# isolates
Lamellipodia	*Cunea, Flabellula, Filoreta, Ripella, Acanthamoeba, Nuclearia*	6	18
Filopodia	*Filoreta, Spongomonas, Nuclearia, Acanthamoeba, Vexillifera, Flabellula*	6	18
Lobopodia	*Cunea, Vermamoeba, Stenamoeba, Acanthamoeba, Pseudoparamoeba, Neoparamoeba, Vexillifera, Ripella, Flabellula*	9	27
Reticulopodia	*Filoreta, Flabellula (WNBr)*	2	6
Blebbing	*Neovahlkampfia, Vahlkampfia, Tetramitus, Naegleria, Cunea*	5	36
Axopodia	*Massisteria*	1	1

B

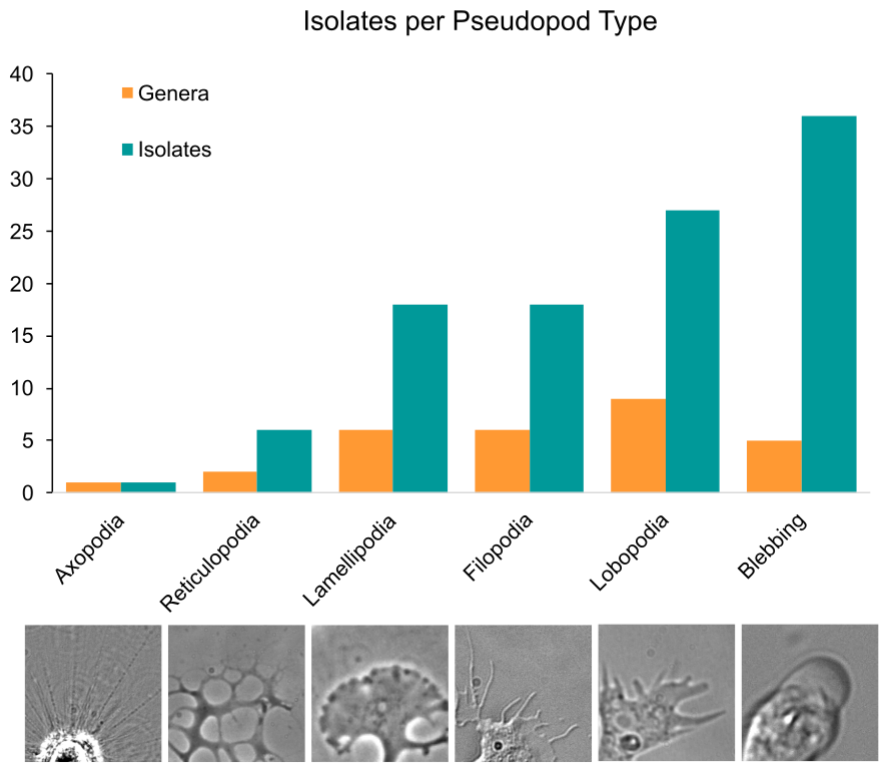

(A) A table quantifying number of genera and isolates per pseudopod type.

(B) Distribution of number of genera identified with pseudopodia morphotype (green) and number of isolates with observed morphotype (orange) for pseudopodia diversity and cultivable amoebae. Representative images of pseudopods in lower panel.

Figure 1.3: Different formats of cysts in various strains

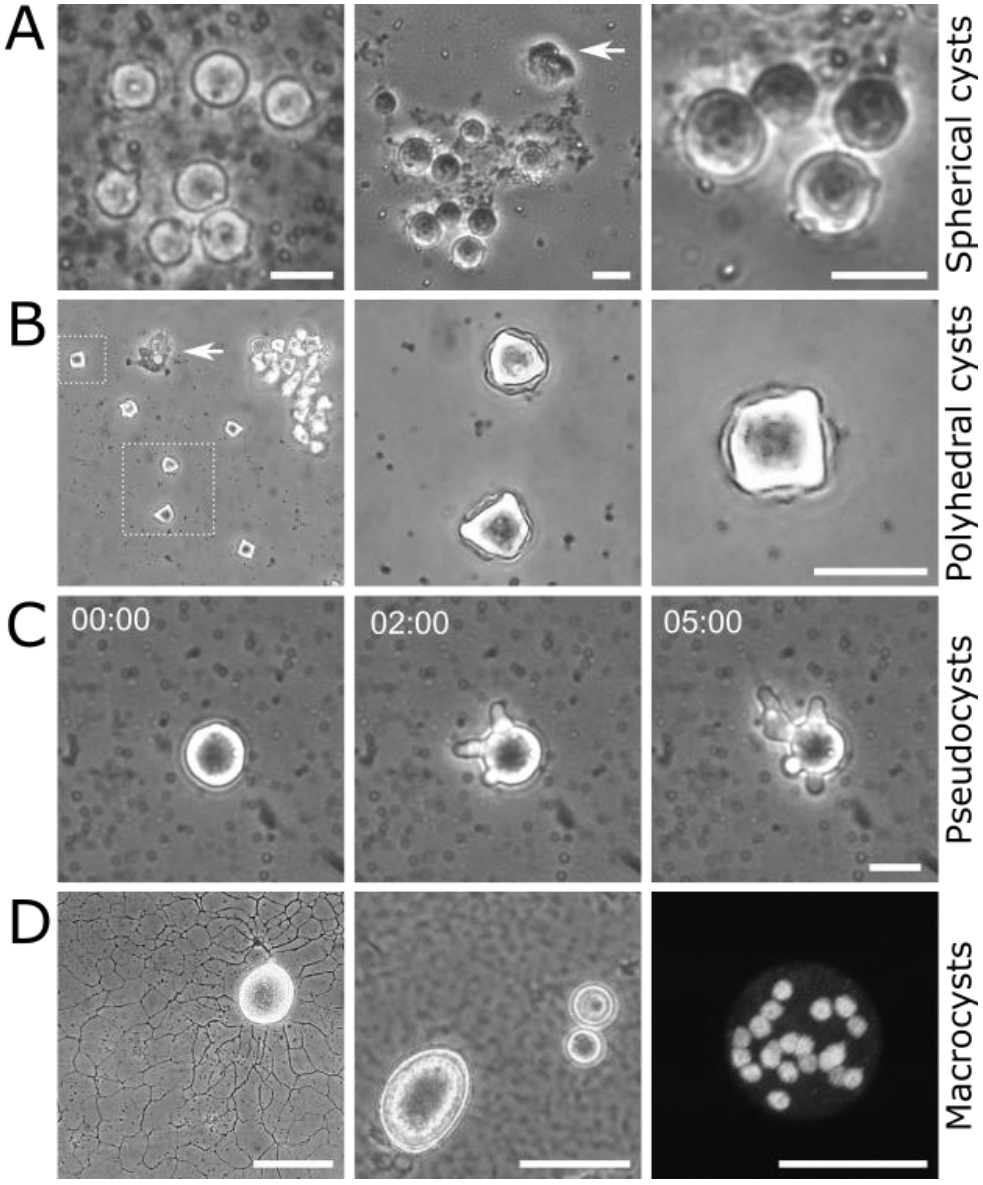

(A) The spherical cysts of Neovahlkampfia (left) and Vahlkampfia isolates. Active amoeba shown in middle panel (arrow). Scale = 10 µm.

(B) The polyhedral double-walled cysts of *Nuclearia.* Active amoeba shown in left panel (arrow). Scale = 10 µm.

(C) The pseudocysts of *Flabellula* strain WNBr developing pseudopods shortly after refreshing medium. Scale = 10 µm.

(D) The large multinucleate macrocysts of *Filoreta* strains BBFil (left), SW4B (center, right). Right panel shows small compact DAPI-stained nuclei within a 10 µm macrocyst. Scale bar = 100 µm (left), 50 µm (middle), 10 µm (right).

Figure 1.4: Fixation optimization following iterative improvements

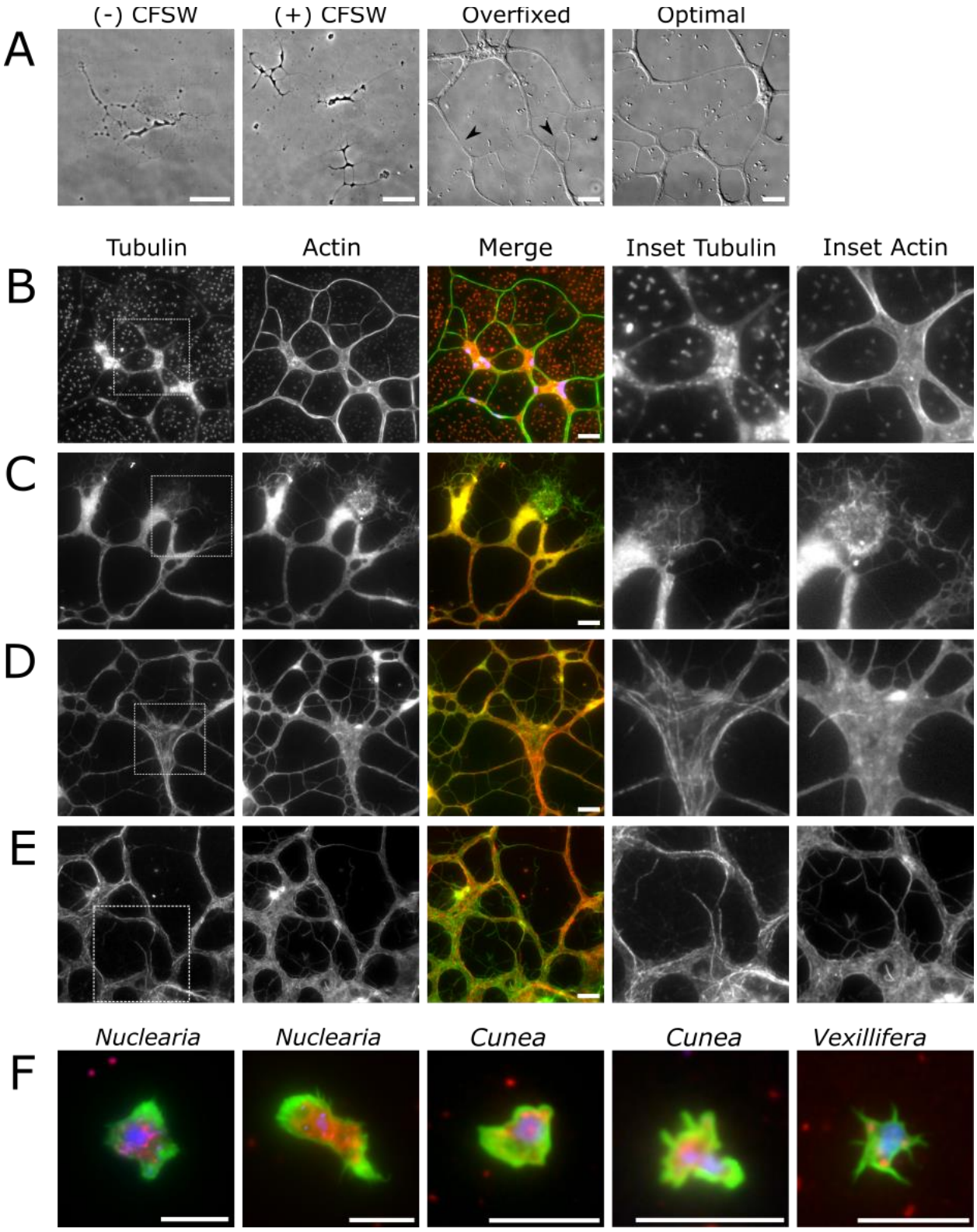

(A) Phase contrast and DIC images of fixed *Filoreta* isolate SW4B. "(-) CFSW" (left panel) fixed with 2% PFA for 5 minutes, showing characteristic beading response of cell body without prior addition of calcium-free seawater. Scale = 50 um. “(+) CFSW” fixed identically, with prior 2-min wash in CFSW. Scale = 50 µm.

"Overfixed" sample, (third panel) 0.5% glutaraldehyde for 5 minutes, showing effects of brittle structures and broken features (arrows). Scale = 10 µm. "Optimal" (far right) 0.5% glutaraldehyde for 30 seconds. Scale = 10 µm.

(B) Suboptimal fixation SW4B. Excessive adhesion of bacterial cells to coverslip, poor retention of microtubule structures. Scale = 10 µm.

(C) Suboptimal quenching of fixed SW4B. Microtubule structure retained, but sample is too autofluorescent to see features in thicker regions. Scale = 10 µm.

(D) Suboptimal staining of SW4B. Sample adequately fixed for microtubule retention, quenched to minimize autofluorescence, but actin-based structures have minimal signal. Scale = 10 µm.

(E) Optimal fixation and staining of SW4B. Microtubule structures apparent, minimal autofluorescence, actin structures and filaments defined. Scale = 10 µm.

(F) Other small marine and freshwater strains fixed using optimized method. *Nuclearia* exhibiting lamellipodia and filopodia, *Cunea* exhibiting lamellipodia and lobopodia, and *Vexillifera* exhibiting branched filopodia. Red = MTs, Green = actin, Blue = nuclei. Scales = 10 µm.

Appendices

Supplemental Videos of amoeba morphology:

1. Blebbing Motility (*Vahlkampfia*) https://youtube.com/shorts/hsgnQAMnjCE
2. Lamellipodia (*Flabellula*) https://youtu.be/wNNq9cIk8tE
3. Axopodia (*Massisteria*) https://youtube.com/shorts/ubvp9C9lCfI
4. BBWNBr branched pseudopodia https://youtu.be/H58A-TcJ0lw
5. Reticulopodia and filopodia (*Filoreta*) https://youtube.com/shorts/i9lNBT65LQ8

Appendix 1: Cultivation Methods:

The protocol outlined here has been implemented in curriculum for microbial diversity course (MIC105L) at the University of California, Davis, and in the Microbial Diversity intensive training course at the Marine Biological Laboratory at Woods Hole, MA.

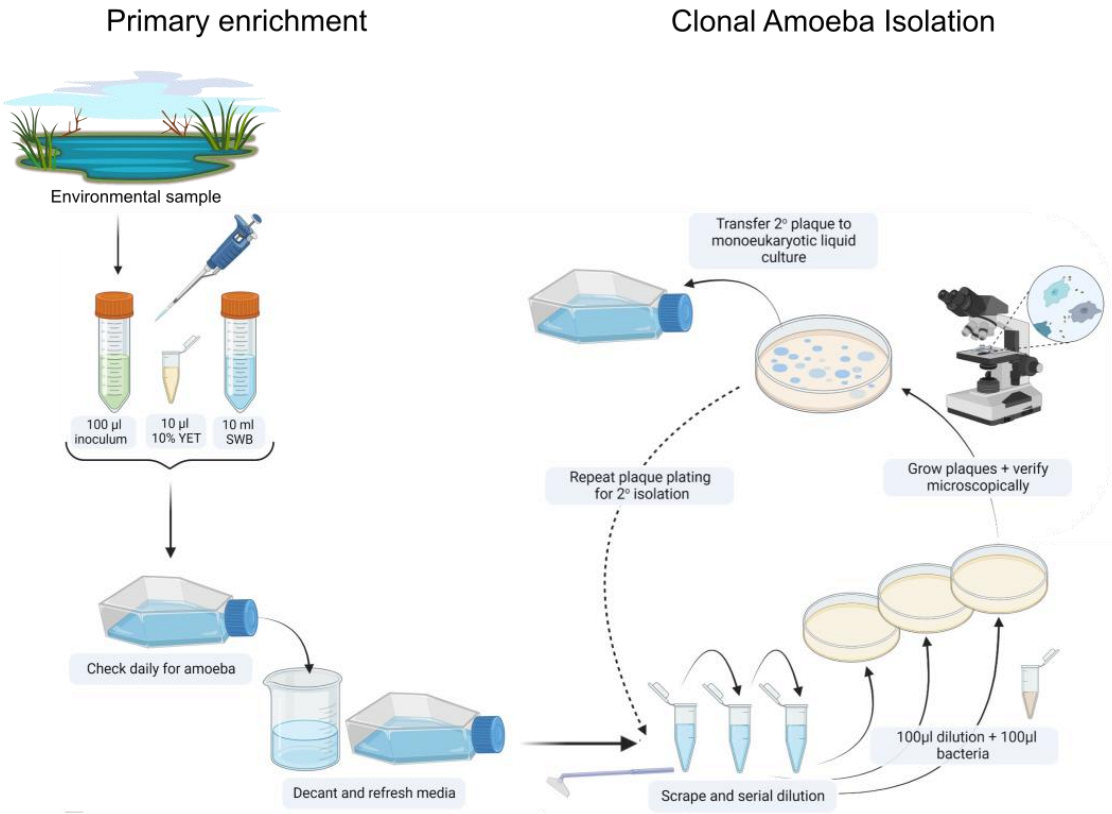

Primary Amoebae Enrichment

1. Obtain several grams of environmental sample, such as detritus-rich sediment, algal biofilms, etc. Surface-attached amoebae isolated with this method are largely adherent and are often found in algae/biofilm consortia in aerobic conditions. Sampling from water without detritus or solid material is generally more challenging.

2. Make an enrichment in a rectangular liquid culture flask (Falcon™ 353014, T25). Such flasks are surface-treated to facilitate adhesion for various cell types, and can be easily monitored for growth on an inverted phase contrast microscope. For marine amoebae, use 100µl of your inoculum source to 10ml of SWB, and "feed" by adding 10µl (or 1µl/ml) of 10% YET (Yeast Extract + Tryptone). Avoid too much sand or inorganic material as this makes it difficult to observe the amoebae through the bottom of the flask.

3. Incubate the culture flask on its flat base at room temperature (20-22°C). Check each day for amoebae on the bottom surface using an inverted phase microscope (recommended) or by making wet mounts from the scraped surface.

Within 1-2 days the enrichment will become slightly cloudy as the environmental bacteria bloom. As the bacteriovorous eukaryotes feed on the bacteria, the medium will become relatively clear again. Enrichments may need to be "fed" in succession, if there are few amoebae present after the first feeding. When numerous amoebae are observed (i.e., >3 per field at 40X magnification), proceed to primary isolation.

Clonal Amoeba Isolation (plaques)

3. Pour off used medium from the flask, and immediately replace with 10 ml of fresh medium. This helps remove extraneous material and eukaryotes that are not adherent. *(It is best to work quickly when tilting the flask upright, as many amoebae are sensitive to drying out, and loss of water to the culture surface can damage them.)* Gently scrape the bottom of the flask (halfway is sufficient) to dislodge adherent amoebae. Of this cell suspension, gently pipette 500 ul into a sterile microfuge tube.

4. Create a small dilution series of the enrichment as 1:1, 1:10, and 1:50, using sterile 1X Seawater Base (SWB). Pipette gently as amoebae lack cell walls and larger cells can be fragile. Transfer dilution series in microfuge (1.5ml) tubes. Keep the flask growing in the same conditions as before (it is recommended to keep this as a backup if the plating isolation fails).

5. Take 100 µL of each dilution and add 100 µL of bacterial "food" in a microfuge tube to 200 µL total volume (fresh marine bacterium overnight liquid culture or colony suspension in SWB). Gently spread each 200 µL mixture onto Amoeba Marine Agar plates by using sterile "hockey sticks." Only spread as much as needed to evenly cover the plate surface, because additional time manually spreading the liquid may shear any of the more delicate amoebae.

6. Label, parafilm to preserve moisture, and store upside down at room temperature. Check daily for plaques. Alternatively to using parafilm, the plates can be incubated in a large plastic container with locking lid to increase humidity. It may take over a week for plaques to begin to appear, though some may form overnight.

Note: Not all amoeba plaques are as distinctive as viral plaques, and often appear as shiny, glossy spreading regions of thinner lawn or strange looking irregular colonies instead of distinct-margined circular “holes”.

7. Once plaques are observed, check under wet mount to make sure amoebae and/or cysts are present. Make note of size and morphology. Carefully identify an isolated plaque without interrupted margins, and take sample by scraping center of the plaque with a sterile tip.

8. Suspend the scraped plaque in a sterile microfuge tube with 500 µL of sterile Seawater Base. Pipette up and down gently- only enough to remove the material from the tip, and vortex on low to suspend fully.

Secondary Isolation of amoebae

9. Perform a new serial dilution as before in sterile microfuge tubes. Add 100µL of bacterial food to each 100µL dilution as before.

10. Spread the combined 200µL onto Amoeba Marine Agar, seal the plate with parafilm, and store upside down. Check daily for plaques. Take note of the previous growth time for your first plaques.

11. When secondary plaques are observed, check under wet mount and compare morphology. There should be only one type of amoeba present, and no flagellates or fungi. Take a scraping from a well-isolated plaque and suspend in liquid medium as before.

Transfer of clonal amoebae to Liquid Medium

12. Add 10 mL of medium into a small flat-bottom culture flask. Add the suspended plaque, and incubate as before at Room Temperature on the culture surface side. Check regularly using an inverted microscope (or wet mount) for amoeba growth.

> *Note: Make sure to watch for other eukaryote contaminants, as the sample cannot be sequenced if it is not a mono-eukaryotic culture.*

13. You may need to refresh the medium, or add more carbon source to encourage further growth of your amoeba strain. Refresh medium with YET in SWB if there are few amoebae, amoebae have mostly encysted or they have stopped growing. (1µL of 10% YET per ml of SWB).

Maintenance of amoebae cultures

Once you have a single type of amoeba in isolation (mono-eukaryotic), the culture can be expanded into larger volumes to generate more cells for the various identification and characterization techniques (*see optional analyses*).

1. Transfer your mono-eukaryotic culture into a sterile cell culture flask containing fresh SWB and YET to increase the volume and total number of cells.
2. Maintain cultures and re-feed by adding additional medium to the flask. After several days, cultures may need to be refreshed by decanting and replacing the medium. If amoebae are not as adherent, the cells can be collected by gently pelleting in a centrifuge to remove spent medium.

Appendix 2: Further analyses for clonal amoebae (mono-eukaryotic) cultures

Identification

Identify amoeba via the eukaryotic 18S rDNA, using eukaryote-specific degenerate primers (Dawson and Pace, 2002). Because amoebae are not monophyletic, using different primer combinations to amplify conserved regions can ensure amplification of products originating in different eukaryotic clades. It is also useful to use an annealing gradient from 45–65°C to ensure maximal specificity. One of four primer combinations generally amplified most taxa using the following two forward and reverse primers: (Forward) 82FE = GAADCTGYGAAYGGCTC; (Forward) 360FE = CGGAGARGGMGCMTGAGA; (Reverse) 1391RE = GGGCGGTGTGTACAARGR; (Reverse) 1200RE = GGRCATCACDGACCTG.

The 18S rRNA amplicon sequences may be obtained by Sanger Sequencing or by first cloning the PCR products using TOPO Cloning (Invitrogen). In some cases, TOPO Cloning may be necessary to obtain quality sequences. Provided the culture is monoeukaryotic, amplification of only a few colonies is generally sufficient to identify the amoebae. If the amoebae are growing in the presence of another eukaryotic organism, the number of bacterial colonies picked may need to be increased to reflect the population ratio of the amoebae. (Some larger amoebae require eukaryotic prey, and therefore must be grown in coculture.)

Live Imaging of amoeboid motility

Imaging the new amoeba isolate is essential to observe and classify their characteristic types of motility. When imaging, it is important to remember that amoebae are often fragile and responsive to their environments. When preparing cells for imaging, keep in mind the importance of capturing cell behavior that is biologically relevant. Most of the aforementioned

amoeba cultures are at room temperature. But imaging conditions can stress the amoebae. So minimize such conditions as heat, fluorescent light, or pH, to ensure that the observations you make are indicative of the cell's usual morphology or motility. Inaccurate live imaging analyses can negatively impact downstream analyses because the "baseline" of your strain's movements, morphology and behavior will be inaccurate.

Where wet mounts work for some types of amoebae, other amoboid cells and movements appear to respond negatively to the limited space, bright light, temperature, and oxygen fluctuations that can occur by being confined to a tight space and under the intense microscope lamp. Depending on the size and shape of your amoebae, being confined to the narrow space between glass may physically disrupt the morphology or behavior. For this reason, it is preferable to perform imaging in a dish with a coverslip bottom (see below) to prevent temperature variations that occur under intense magnification. One typical way to note that the imaging conditions are not optimal is to note that the amoebae stop crawling, round up as they swell and uptake water, produce blebs, and eventually lyse.

Preparing amoebae for staining and imaging in a Mattek Dish

Gently scrape the culture surface with a cell scraper to suspend cells, then pipette 1 ml of amoeba suspension into the Mattek dish, directly onto the glass coverslip in the center. Let them settle by gravity for 15-30 minutes to ensure the cells land and adhere to the glass surface where they can be imaged. After they have adhered, add an additional 2 ml of sterile medium to allow the "bubble" to fill over, and fill the bottom of the dish. This ensures that the majority of amoebae will be attached to the imaging surface of the dish. See figure below.

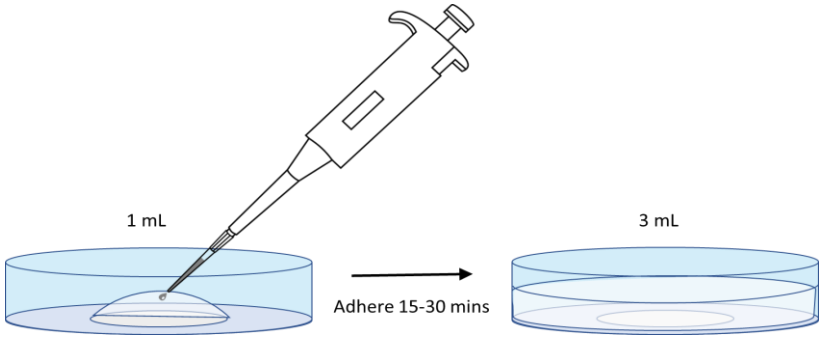

With a known volume in the dish, it is easy to adjust the added volume of staining solutions. Typically, a 2X concentration is made of the stain or dye, and added at a 1:1 ratio to an existing volume of medium in the dish, to prevent the cells from desiccating and ensuring rapid distribution of the additive. For example, if you remove 1.5ml of SWB from the 3 ml in the dish, add back 1.5 ml of the 2X staining solution to reach a final working concentration of 1X. If the staining solution requires wash step(s), simply remove and replace medium by pipetting from the side of the dish to avoid disrupting cells on the glass surface.

Example Fixations:

Note: In all cases, fixatives and other solutions are replaced by gently pipetting down the corner of a well, not directly over the coverslip. Coverslips that float to the surface must be immediately re-submerged using forceps, as loss of sample may occur if allowed to dry between steps.

<u>4% Paraformaldehyde Fixation</u>

1. Prepare clean number 1.5 coverslips by coating in 0.1% cold-water fish skin gelatin. Add 50 µL 0.1% gelatin to a coverslip and smear across surface with another coverslip until coated evenly. Allow the surface to dry fully, either at room temperature or in a warm incubator.

2. Place coated coverslips face up into an 8-well rectangular dish (Thermo 267062), Add the cells to the surface of the coverslips using the “bubble” method as described in Mattek dish

preparation. Let amoebae adhere undisturbed for at least 30 minutes, then add 2ml of sterile room temperature calcium-free seawater (CFSW) (NaCl (469 mM), KCl (10 mM), $MgCl_2$ (36 mM), $MgSO_4$ (17 mM), HEPES-NaOH (10 mM, pH 8.2), EGTA (10 mM)). Let sit 2-5 minutes.

3. Remove CFSW (leaving enough to keep coverslip submerged) and immediately replace with fixative solution (Paraformaldehyde (4%) fixative (20ml calcium-free seawater containing 0.4 M sucrose, 8ml cytoskeletal stabilizing buffer (CSB) (recipe below), 4ml 32% paraformaldehyde) for 10 minutes. CSB was prepared as a 10x stock and contained 50 mM KCl, 1.37 M NaCl, 40 mM NaHCO3, 110 mM Na2HPO4, 20 mM MgCl2, 50mM PIPES, 20 mM EGTA. Further optimization may be necessary for different types of amoebae.

4. After 10 minutes of fixation, remove fixative and quench by adding 2ml of PEMBALG (100 mM PIPES, 1 mM EGTA, 0.1 mM MgSO4, 1% bovine serum albumin, 0.1% sodium azide, 100 mM lysine, and 0.5% cold-water fish skin gelatin) (Woessner and Dawson, 2012).

5. Permeabilize with 0.1% TritonX-100 for 10 minutes, followed by three successive washes in PEM (100 mM PIPES, 1 mM EGTA, 0.1 mM MgSO4).

6. Apply antibodies and counterstain as desired, blocking between each step using PEMBALG.

7. Mount the coverslips on slides with an aqueous mountant, such as ProLong™ Glass Antifade Mountant (Cat. No. P36980).

<u>5% Glyoxal Fixation</u>

1. Prepare cleaned, 0.1% Gelatin-coated coverslips, and add cells to the surface as described above. Let amoebae adhere undisturbed for at least 30 minutes, then add 2ml of sterile room temperature CFSW. Let sit 2-5 minutes.

2. Remove CFSW (leaving enough to keep coverslip submerged) and immediately replace with glyoxal fixative (1.5ml of 40% glyoxal (Sigma 128465), 2ml ethanol, 1ml CSB, 7ml calcium-free seawater) for 30 seconds.

3. Immediately quench fixation by replacing fixative with PEMBALG, then allow to sit undisturbed for 2 minutes to rehydrate. Replace with new PEMBALG for two more washes, 2 minutes each.

4. Permeabilize in 0.1% Triton-X 100 diluted in PEM for 10 minutes, followed by three successive washes in PEM.

5. Apply antibodies and counterstain as desired, blocking between each step using PEMBALG, then mount on slides as described above.

<u>0.5% Glutaraldehyde Fixation</u>

1. Prepare cleaned, 0.1% Gelatin-coated coverslips, and add cells to the surface as described above. Let amoebae adhere undisturbed for at least 30 minutes, then add 2ml of sterile room temperature CFSW. Let sit 2-5 minutes.

2. Remove CFSW and immediately replace with glutaraldehyde fixative (0.5% glutaraldehyde, 5% sucrose, in calcium-free seawater buffered with 1X CSB) for one minute.

3. Immediately quench fixation by replacing fixative with PEMBALG, then allow to sit undisturbed for 2 minutes to rehydrate. Replace with new PEMBALG for two more washes, 2 minutes each.

4. Replace PEMBALG with 0.2 M Glycine for one hour at room temperature to quench unreacted aldehydes to reduce autofluorescence. Alternatively, two successive washes in

sodium borohydride (caution) can be used on ice for 10 minutes each (1mg/ml $NaBH_4$ in CFSW).

5. Permeabilize in 0.1% Triton-X 100 diluted in PEM for 10 minutes, followed by three successive washes in PEM.

6. Apply antibodies and counterstain as desired, blocking between each step using PEMBALG, then mount on slides as described above.

Chapter 2

Genomic evidence for conserved developmental strategies in the genome of the Rhizarian amoeba *Filoreta ramosa*

Sarah L. Guest, Kirk R. Amundson, and Scott C. Dawson

Department of Microbiology and Molecular Genetics

One Shields Avenue

UC Davis, Davis, CA 95616

Abstract

While the eukaryotic lineages of metazoa, fungi, plants, and parasites have received significant attention and include well-established model systems, the eukaryotic supergroup known as the Rhizaria have been comparatively neglected despite their significance in cell biological and evolutionary contexts. Although the clade is as genetically diverse as the Opisthokonts, a lack of working model systems has made studying the Rhizarian group an enigmatic and daunting pursuit. Our recent Rhizarian amoeba isolate, *Filoreta ramosa*, is stably maintained as a mono-eukaryotic culture, enabling closer examination of its physiology and complete genome sequencing and annotation.

By leveraging comparative genomics with other Rhizarian protists, we achieve a deeper perspective on their evolutionary history and the unique adaptations that have shaped cellular dynamics in this clade. This genome report on *Filoreta ramosa* significantly contributes to our knowledge of Rhizarian cell biology. It stands as a milestone as the third complete Rhizarian genome, which is comprehensively annotated with respect to the organism's life cycle and morphological development. The proteins identified in this report mirror the observed intricate spatiotemporal organization of *Filoreta* in culture; its functional modes of amoeboid motility, extensive interphase microtubule arrays, and long-ranged organelle transport via varied motor proteins align with the complex syncytial stage of development. Moreover, the genetic content sheds light on the organism's intricate interactions with its environment, incorporating pathways like photoreception, neuron-like signaling receptors, and the orchestration of lipid biosynthesis and membrane trafficking which accounts for the syncytium's extensive surface area.

This study highlights key aspects of *Filoreta's* life cycle and cellular behavior, while also emphasizing the importance of further research to observe and validate the presence of the

flagellate stages in this lineage of Rhizaria. Additionally, shared cytoskeletal and signaling features between *Filoreta* and metazoan neurons opens a new avenue for understanding the evolution of signaling, morphology, and spatial differentiation across eukaryotes. The genetic evidence and genomic data presented here pave the way for new discoveries in the study of this syncytial life cycle and provide valuable insights into the broader understanding of the Rhizarian supergroup.

Introduction

Comparative genomic efforts across the eukaryotic tree have yielded important insights to the evolution of eukaryotes yet have missed many key microbial taxa primarily due to their absence from culture collections. The Rhizaria are one of the major supergroups of eukaryotes, and are part of the Stramenopile, Alveolate, Rhizaria (SAR) clade which comprises roughly 60% of all eukaryotic diversity (del Campo et al., 2014; Grattepanche et al., 2018). Rhizaria are as genetically diverse as Metazoa, yet in comparison to the other lineages the molecular and cell biology, development, and genetics of the Rhizaria remains largely understudied. (Burki and Keeling, 2014; Harder et al., 2016).

Rhizarian protists are morphologically diverse as well and may range in size from just over 2 µm (*Massisteria voersi*) to over 20 centimeters (Xenophyophore), with most lineages comprising amoeboid cell types in at least one stage of their often-complex life cycles(Gooday et al., 2017; Mylnikov et al., 2015). The Rhizaria have been sorted into three major lineages, the Cercozoa, Foraminifera and Radiolaria. While many members of Rhizarian lineages have been morphologically described, few are cultivable for long-term laboratory investigations. The complex life cycles of Rhizaria, which often involve various stages and morphological forms,

pose challenges for their comprehensive characterization. While individual stages and life cycle components have been described for specific members within the Rhizarian lineages, a comprehensive understanding of the entire life cycle of a Rhizarian species is still lacking.

Many of the Rhizarian amoeboid species form tests, making them invaluable tools for the fossil record and palaeoecological indicators due to their role in the global carbon cycle (Burki and Keeling, 2014; Orsi et al., 2020; Tyszka et al., 2019). Rhizaria also sequester carbon and other minerals to build their tests and are a major contributor to the global carbon cycle, with immense amounts of carbon falling to the ocean floor each year in the form of empty (dead) tests, which will not re-enter the carbon cycle for hundreds of years. Rhizarian test deposition can be an indicator of oceanic and sea-floor health, as Rhizaria that use calcium carbonate (CaCO3) that sequester carbon from re-entering the atmosphere. Additionally, CaCO3 sequestered by Rhizaria helps to alkalinize the sediments at the ocean floor, buffering the ocean acidification process. However, as oceans become more acidic due to anthropogenic CO2, the biological CaCO3 deposition slows, and Rhizarian plankton are unable to build shells at the same rate. This in turn yields less carbon removed from the cycle and less mass of CaCO3 available at depths that normally regulate alkalinity.

Rhizarian amoeboid protists are notable for their specialized pseudopodia called ***reticulopodia***, which are extensively branched, form loops (a fusion process called ***anastomosis***), and exhibit unusually rapid transport and dynamic reorganization (Bowser and Travis, 2000). The reticulopodia exhibited by Rhizarian amoebae are morphologically similar to the pseudopodial networks of branch-forming Amoebozoa, but there has been little to no investigation on the cell biology, mechanism and potential convergence or conserved components between the two clades (Berney et al., 2015). In addition to reticulopodia, many Rhizarian amoebae are capable of

forming lamellipodia and filopodia more commonly seen throughout the eukaryotic tree, highlighting the potential for an extensive repertoire of actin and actin-associated cytoskeletal proteins.

The lack of available genome information from diverse lineages like the Rhizaria has put these organisms at the trailing edge of evolutionary cell biological efforts. To date, there are only two complete Rhizarian genomes: *Reticulomyxa filosa* and *Bigelowiella natans* (Curtis et al., 2012; Glockner et al., 2014). Of the research investigating the Rhizarian amoeboid cytoskeleton and morphology, *Reticulomyxa's* genome and cytoskeletal studies indicate intriguing evolutionary characteristics of the clade(Bowser and Travis, 2000; Glockner et al., 2014; Orokos et al., 2000; Orokos and Travis, 1997). A Rhizarian divergent beta tubulin is capable of depolymerizing in a non-canonical mechanism yielding helical fragments, rather than canonical protofilaments (Habura et al., 2005). The transport mechanisms allowing for rapid and bidirectional transport of organelles across large distances has been attributed to a novel bidirectional Rhizarian motor protein (Schliwa et al., 1991). Additionally, many Rhizarian amoeboid species are often multinucleate (syncytial) in at least one life stage, during which the means for organelle and nuclear positioning and karyoplasmic maintenance are integral to maintain nuclear autonomy. Similar to other multicellular systems like *Physarum*, a Rhizarian syncytium would require some format of spatial differentiation to distinguish cell polarity and raise dynamic and appropriate responses to its environment (Gerber et al., 2022).

Rhizarian protists thus provide a foundational tool for understanding multiple facets within the evolution of multicellularity in eukaryotes, and the dynamic changes in structure and self-organizing mechanisms involved in multiphasic lifecycles. Here, I define the life cycle and the genome of a novel isolate *Filoreta ramosa (*"ramosa" = Latin; "having many branches"*)*, a

relative of the previously described species *Filoreta marina (AY268044), F. tenera (EF514503 ATCC 50975), F. turcica (EU567292),* and *F. japonica (EU567293).* This analysis represents the first life cycle characterization of this clade and is also the third genome from this important group. *Filoreta* ramosa is readily grown in the lab, and I have also been able to track the majority of life cycle stages in laboratory culture. This life cycle and genomic analysis provides a foundation for future molecular, cell and developmental, and genetic tools that will enable future study of the first Rhizaria non-model organism.

***Filoreta ramosa* species description:** Individual cells variably shaped, usually semi-rounded with few protruding filopodia. Remain briefly unicellular in liquid culture and quickly form a network with other cells by extending pseudopodia. Syncytial stage also induced by physically perturbing the culture surface, where cells respond to physical stress by fusing together. Once fused, the syncytial body varies widely in size depending on stage of growth. Freshly excysted syncytial body extends radially by extending both filopodia and lamellipodia to capture bacterial prey and crawl outwards at speeds up to 5 μm/minute. Pseudopodia constantly anastomose into a reticulated network with increasing density of smaller loops towards the periphery and pruning or simplification to interior branch loops. Syncytia will grow and fuse to neighboring bodies to cover the entire culture surface area, so far measured to 225 cm^2, but not necessarily limited to that size. Branches of the network vary in width: widest branches at the cell interior during initial stages of outgrowth, at sites of neighbor-fusion events, and at hub formation during early encystation stage.

Reticulopodial granules absent, but intracellular organelles and components visibly swell membranes of narrow branches and move bidirectionally along internode lengths. Culture response to abiotic culture medium lacking nutrient sources results in complete encystation

within 96 hours. Macrocysts vary in size from 10-200 μm in diameter, spherical to ovoid, appearing to be double-walled and often presenting with a golden orange hue (esp. in larger cysts). Macrocysts appear medium to dark orange in color when concentrated by centrifugation. Macrocysts contain several to hundreds of nuclei, which occasionally do not resolve to single nuclear packages upon DAPI staining. Cysts have been observed to remain dormant for over 2.5 years in artificial seawater at room temperature, and capable of exiting stasis without issue upon culture refresh. Bacterivorous, though it will consume marine yeasts and undergoes micropinocytosis in enriched medium. Samples were originally collected from Little Sippewissett Marsh, MA (41°34'33.6"N 70°38'22.7"W) from detritus-rich sediments at the intertidal brackish pool during low tide, July 2014. Strain SW4B was isolated on solid media September 2014 at UC Davis.

Results

Overall genome structure and completeness

The assembled *Filoreta* genome was approximately 35.8 Mbp across 107 contigs, with an N50 of 2.54 Mbp (Figure 2.1A). Twelve of the contigs were over 1 Mbp, and another ten were between 1Mbp and 100 Kbp (Figure 2.1B). The GC content was approximately 46% across all contigs and consisted of 55.5% coding vs non-coding regions. We predicted a total of 11,518 protein coding genes. An average of 4.4 introns were found per gene, with an average length of 87.75 bp, and median of 47 bp.

We identified telomeric sequences in several of the larger contigs (Figure 2.1C-D) including at least one contig with full end-to-end (telomere to telomere) continuity. The telomere monomers were identical and had a “TAGTGT” repetitive sequence over 200-500 bp at each end. We also found unusual regions of short monomeric tandem repeats of “ATTTT-ATTTT” and “ATT-

ATT" near the centers of the contigs ranging from 130-700bp in which the entire region had a GC content of 0% and were often flanked with long poly-T sequences. We characterized these as presumptive centromeric regions of interest. Transposable elements (TEs) were identified and mapped by percentage across the contig lengths, and had an average length of 351 bp, with about 0.1 TEs per Kbp of contig length, or roughly 1 TE per 10,000bp (Figure 2.3C-E).

We found a complete set of tRNA sequences, 155 total, with multiple copies per tRNA type across all amino acid residues, and 20 pseudogenes (Figure 2.2A, B). Ribosomal RNA subunits were identified across numerous contigs, with 74 - 18S, 77 - 28S, 77 - 5.8S and 24 – 5S subunit copies (Figure 2.1A).

Genome "completeness" is difficult to determine in protists. One commonly used method to determine completeness - BUSCO analysis – is notoriously poor at predicting genome completeness in protists in particular due to undersampling of protist genomes (Johnson et al., 2019). Despite this caveat, we used BUSCO analysis with the pan-eukaryote dataset to determine that the *Filoreta* genome is 71.4% complete (182 complete out of 255 BUSCO conserved genes), with 176 single-copy and 6 duplicates; 36 BUSCO genes were fragmented and 37 were missing entirely (Figure 2.2C, D). When we compared this to our protein set, the completeness was 84.4% (215 complete out of 255 BUSCOs). Using other limited BUSCO gene sets, we found that the *Filoreta* genome had 82.0% completeness (genome to Stramenopile BUSCOs) versus 90.0% (protein set to Stramenopile BUSCOs), and 88.3% (genome to Alveolate BUSCOs) versus 90.6% (protein set to Alveolate BUSCOs).

To define overall metabolic pathways, conserved proteins and conserved protein families, we performed a KEGG analysis using GhostKOALA (REFS). The GhostKOALA KEGG pathway

reconstruction analyses yielded full metabolic pathways and several unexpected biosynthesis and signaling pathways, which we used as a starting point for identifying other proteins of interest (Aoki-Kinoshita and Kanehisa, 2007; Kanehisa et al., 2016).

***Filoreta* protein repertoires reflect observed functional processes throughout the life cycle.**

Filoreta's life cycle (Figure 2.6) follows a multiphasic development from excystation. Macrocysts excyst and give rise to either individual amoebae or a syncytium. The amoebae are migratory and produce both lamellipodia and elongated filopodia (Figure 2.6, top row), and readily fuse together to form the multinucleate syncytium. This coordinated process requires activity of the cytoskeleton to produce motility toward neighboring cells. We found actin and microtubule- associated cytoskeletal genes involved in amoeboid motility (Tables 2.1, 2.2) that reflect an expanded cytoskeletal protein repertoire. The genome contains six alpha-tubulins and five beta-tubulins, five actins, seven canonical actin-related proteins (Arps), and twelve novel Arps. We did not find a canonical myosin II, which is known to provide contractile forces for amoeboid motility in many migratory eukaryotic cells (Jay et al., 1995). The unusual myosin II copies in *Filoreta* suggest that the contractile forces driving amoeboid motility in Rhizaria may occur through a different mechanism.

The observed amoeboid motility is reflected in actin and tubulin-associated proteins in the genome.

Actin and microtubule interactions are important for many types of amoeboid motility, as microtubules and their orientations create the scaffold for directed movement (Kopf et al., 2020). Actin-binding and microtubule-binding proteins can interact; notable examples of such interactions include the microtubule crosslinker Tau and actin crosslinker ACF7 in neurons. The microtubule end-binding protein EB3 interacts with drebrin, which in binds actin filaments

(Dogterom and Koenderink, 2019). Formins are another protein interactor that can mediate microtubule dynamics with actin polymerization (Bartolini and Gundersen, 2010). We identified formins as potential MT-actin interactors, yet *Filoreta* lacks Tau, ACF7, and drebrin homologs.

The presence of key cytoskeletal proteins in *Filoreta* supports the phenotypic similarity of the branched, reticulated syncytial network to other branched cellular types in Metazoa.

In the syncytial form, *Filoreta* develops its branched reticulated network (Figure 2.6, 2.7) by pseudopodial extension and elongation of its branches in a manner physically similar to the arborization of neural cell types. The syncytial cytoskeleton exhibits an extensive microtubule array, with longitudinal MTs that are partially contiguous through most branch nodes (Figure 2.7). We identified proteins involved in microtubule stability, bundling, and branched nucleation machinery, including XMAP215, MAP65, SSNA1, and all components of the gamma-tubulin ring complex (ɣ-TuRC). We were unable to identify homologs to Tau, Augmin or TPX2, though branched microtubule nucleation can occur laterally via SSNA1 scaffolding and ɣ-TuRC recruitment (Basnet et al., 2018; Lawrence et al., 2021).

Conserved cytoskeletal motor proteins support observations of rapid nuclear transport in the syncytia

Organelles and nuclei move rapidly and bidirectionally throughout the network during the syncytial stages of development (Figure 2.8). The nuclei were often visibly compressed as they squeezed through narrow branches, and relaxed (recovered rounded appearance) quickly after exiting the branch into a wider node (Figure 2.8A). The nuclei were compressible to approximately 0.5 µm, less than 25% of their normal diameter of 2.2 µm. Lamins are known to provide flexible support of the nuclear envelope, and nuclear compression is typically limited to prevent nuclear envelope rupture. We identified one B-type lamin, which matches the

distribution as Type A lamins are typically only found in vertebrates (Adam and Goldman, 2012).

We tracked nuclear movements in the syncytial networks at rates averaging 5.3 µm/sec and up to ~12 µm/sec (Figure 2.8B). Numerous motor proteins are present in the genome that are likely key for this extensive transport, including sixteen dynein heavy chains (13 axonemal, 3 cytoplasmic), five intermediate chains (one cytoplasmic), five light intermediate chains (one cytoplasmic), and four light chains. There are also thirty-seven kinesins (18 of which are canonical), five dynactin proteins (dynactin 1, 4, 5, and subunit p22), and at least eighteen myosins (including eight myosin I, four myosin IV, two myosin II-like, one myosin 7-like, and several orphans). In syncytial fungi, nuclear migration and distribution is regulated by a nuclear distribution protein called NudF, which is a homolog to metazoan gene LIS-1 required for normal brain development. Haploinsufficiency of LIS-1 leads to catastrophic effects of lissencephaly, as LIS-1 is required for nuclear positioning and neuronal migration by mediating dynactin binding on microtubules (Markus et al., 2020; Trokter and Surrey, 2012; Xiang et al., 1995). We also found a LIS-1/NudF homolog in *Filoreta* that has the conserved domain architecture of LIS-1 and a coronin-like actin binding region in the WD40 tandem repeat domain.

Conserved flagellar genes indicate a missing flagellate stage

Similar to observations in long-term cultures of *Reticulomyxa,* we have not observed any flagellate form in *Filoreta* in ten years in active culture. However, the genetic content indicates a flagellate stage exists in the *Filoreta* life cycle, as the necessary components for axoneme structure, axonemal dyneins, intraflagellar transport (IFT) and basal body appendages are present (Table 2.4, Figure 2.10).

Conserved nuclear structural and anchoring proteins suggest conserved mechanisms for nuclear transport in syncytia

Nuclear structure and positioning complexes are important in many syncytial organisms for maintaining nuclear distribution and spatial organization (Gladfelter and Berman, 2009; Roberts and Gladfelter, 2015). We identified the components involved in nuclear structure and anchoring to the cytoplasm including a nuclear lamin, all components of the nuclear pore complex (cytoplasmic filaments, inner and outer rings), the transcription-export (TREX) complex THOC1, C2, C3, and importins, and the LINC (Linker of Nucleoskeleton and Cytoskeleton) components SUN (Sad1p, UNC-84) and KASH (Klarsicht/ANC-1/Syne Homology) proteins (Table 2.6). The TREX complex components THO C1, C2 and C3 were not previously reported in any members of the SAR group (Makarov et al., 2021; Serpeloni et al., 2011). The presence of these components in *Filoreta* signifies the conserved nature of the TREX complex and its potential functions in RNA nucleocytoplasmic export across the eukaryotic tree.

Conserved cell cycle and mitotic genes despite an inability to determine the timing of mitosis during the life cycle.

Although we have not directly observed mitotic events, the syncytial growth and increased number of nuclei accommodating that size indicates that mitosis potentially occurs in the syncytial stage. Our analyses identified the components for spindle assembly and structure (aurora kinase 1, CKAP5, etc), sister chromatid separation protein separase, anaphase-promoting complex (APC1- 8, 10), and cell cycle progression proteins (cyclins A, B and E) (Table 2.6).

The presences of encystation-specific components predict the mechanism of macrocyst wall formation

During the development of the expansive network, regions of intersecting branches become thickened and eventually swell to form hubs (Figures 2.6, 2.9). These hubs become filled with nuclei as they traffic into the hub (Figure 2.9B) as they mature and round up to form the multinucleate macrocysts (2.9A).

Though the composition of *Filoreta's* cyst walls remains unclear, we identified biosynthesis pathways for sterols, glycans, and the enzyme UDP-N-Acetylglucosamine pyrophosphorylase – a key component to the production of chitin and cellulose based cell walls (Liu et al., 2013).

Genetic support of "self" branch fusion, branch healing, and signaling

Filoreta consistently fused membranes with itself throughout its life cycle. First, amoebae fused to form the syncytium, then the syncytium fused branches to form the reticulated network as it grew in size (Figure 2.6). When neighboring clonal syncytia grow together, they fuse to form a larger syncytial network (Figure 2.11A). Syncytial networks can also heal from physical shearing by growing back together and fusing membranes (2.11B).

We also observed the syncytial development of *Filoreta ramosa* strain SW4B in co-culture with other *Filoreta* strains isolated from other environmental samples (Chapter 1). Each strain only fused to its own strain type (a clonal population), and actively avoided contact and fusion with the other strains (Figure 2.12). The SW4B syncytium opted to break its own branch in two upon contact by a "non-self" pseudopodium (2.12A). It also broke radial symmetry to grow away from non-self neighbors, and increased growth towards its own strain type (2.12B).

We sought to identify potential pathways of self-recognition in *Filoreta* to explain this phenomenon. Several different signaling receptors are present in the genome, including six copies of domain-verified 7-transmembrane GPCRs ("Rhodopsin-like"), six gamma-aminobutyric acid (GABA) type B receptors and transporters, three ionotropic glutamate receptors, a metabotropic glutamate receptor, nine Hedgehog signaling receptors Patched 1, and several voltage-dependent calcium channels (Table 2.7). There were also numerous pathways for lipid and sterol biosynthesis, key components for membrane organization, vesicle fusions and interactions (syntaxins), and membrane repair (dysferlin) and tactile detection by the mechanosensitivity ion channel Piezo.

Discussion

For the first time, I have described the *Filoreta* life cycle which entails multiple developmental phases requiring dynamic changes in proteins, structures and spatial differentiation. In the switch between the individual amoeba to fused syncytial form, *Filoreta* must produce and recognize a signal of "self," migrate and/or grow towards neighboring cells, fuse membranes and reorganize intracellular components and organelles. Then, the growing syncytium generates an organized network through the cytoskeletal arrays and interacting proteins that is able to dynamically respond to its environment.

The extensive cytoskeletal network reflects the composition of the cytoskeletal protein repertoire we identified in the *Filoreta* genome. Pseudopodial turnover and branch extension requires the coordination of actins, Arps, elongating, capping and bundling proteins, myosins, crosslinkers, and complexes involved in MT-actin crosstalk (Table 2.1). The extensive microtubule cytoskeleton requires nucleation complexes, bundling proteins, regulators, post-translational modifiers, end-binding and severing proteins (Table 2.2).

For a cell to grow to a large size, it must overcome the problem of organelle distribution and spatially organize itself and enable dynamic responses to its environment (Gerber et al., 2022). The motor protein repertoire driving organelle and nuclear transport along the cytoskeletal network facilitates the proper distribution of organelles for the syncytium.

During development, the syncytium increases in size and surface area, a task that involves extensive lipid biosynthesis for membranes to accommodate the highly arborized structure (Pfenninger, 2009). The syncytium detects changes in its environment and alters its network architecture in accordance, likely undergoing signal transduction to modify the spatial organization of branches and the organelles within them. The signaling repertoire of *Filoreta* includes numerous conserved GPCRs, GABA receptors, ionotropic and metabotropic glutamate receptors, calcium channels and photoreception pathways known to mediate these signaling processes (Table 2.7).

Cues initiating encystation can be stress-related or part of life cycle development. Production of macrocysts by the syncytium also requires nuclei and organelle trafficking into specific regions of the syncytial body, indicating coordinated and directed movements in the multinucleate cell across large distances.

Spatiotemporal organization

In other organisms exhibiting syncytial or coenocytic lifecycles, mitotic events can be synchronous or asynchronous. In the Amoebozoan *Physarum polycephalum,* nuclei undergo a closed mitosis that is parasynchronous in waves in the multinucleate syncytial form, but open mitosis in unicellular form (Gerber et al., 2022; Solnica-Krezel et al., 1991). In the syncytial fungus *Ashbya gossypii,* mitosis is asynchronous and nuclei go through cell cycles independently from their neighbors (Gibeaux et al., 2017). It is also noteworthy that in asynchronous mitosis,

the energy requirements and response of the organism to its environment is not hindered by the process of division in one big event.

While I have been unable to observe mitotic stages, I hypothesize that *Filoreta's* nuclei are transported as a function of localized responses, which may be coupled with the cell cycle as seen in fungi and neurons (Markus et al., 2020; Xiang et al., 1995). I predict that mitosis occurs in the multinucleate syncytium (coenocyte) stage. Since syncytia can grow to cover multiple square centimeters without entering the encystation phase, they must increase the number of nuclei as they increase in size to maintain the karyoplasmic ratio (Huber and Gerace, 2007). A likely mechanism involves asynchronous mitosis of nuclei that are not undergoing rapid transport, reducing their potential for shearing and loss of nuclear content within branches with high organelle traffic. This could potentially occur in the greatly clustered "hubs" where there is more room for organelles, less compression of nuclei, and slower vesicular movements, or at the syncytial periphery where the network has room for expansion.

In fungal syncytia, nuclear positioning is crucial for normal growth, as nuclei can change their local cell architectures through altered cell cycle dynamics and gene expression as a response to changes detected in their environment (Roberts and Gladfelter, 2015). Nuclei also migrate along microtubules in neuron progenitor cells as a function for cell division towards the tissue periphery for more efficient progenitor expansion (Fish et al., 2008; Umeshima et al., 2007). In *Filoreta*, I observed that nuclei are not propelled by cytoplasmic streaming, but rather are actively transported along microtubules within the same branch. Nuclei move independently, bidirectionally, processively, often at different rates (Chapter 3). Nuclear positioning is important for several different cell processes, and typically entails nuclear pore complex machinery and anchoring interactions via SUN/KASH with motor proteins and the cytoskeleton (Fridolfsson

and Starr, 2010; Kim et al., 2015). We identified several of these interacting components that are known to play a role in nuclear positioning and transport and are conserved in other eukaryotes (Table 2.5).

The complexity of the rhizarian MT cytoskeleton is reflected in its cytoskeletal proteins

The Rhizarian cytoskeleton and motor proteins have been a source of intrigue for cell biology since the 1980s, when the unusually rapid transport of organelles and other materials garnered attention to the freshwater Foraminifer *Reticulomyxa* (Euteneuer et al., 1988; Koonce and Schliwa, 1985; Schliwa et al., 1991). We had observed similar transport rates in *Filoreta* and identified the cytoskeletal and motor protein components in this Rhizarian relative. Overall, we found that *Filoreta* has a somewhat expanded cytoskeletal repertoire as compared to the genome size and content of *Reticulomyxa*.

Duplication of tubulin isoforms occur throughout the eukaryotic tree. An increase in isotype number is thought to be a facet of multicellular complexity, but there are many free-living protists that break this rule (MacRae and Langdon, 1989). To illustrate, *Filoreta* has 6 α-tubulins and 5 β-tubulins. Prior work in *Reticulomyxa* uncovered an unusual and divergent β-tubulin isoform, with an insertion site in the H1-B2 loop. This is suggested to be responsible for enhanced beta-beta contacts in polymerized microtubules, resulting in altered microtubule dynamics and non-canonical depolymerization geometry (Habura et al., 2005). These increased beta-tubulin affinities lead to alpha-beta dimers unfurling in a helical fashion around the perimeter of the tubule, rather than into separate protofilaments. This divergent beta tubulin was found in Foraminifers but not in the other described Rhizaria. We searched and aligned *Filoreta*'s beta tubulins to the existing B2 alignment and found that while there is substantial

overlap of sequence similarity, yet *Filoreta* beta tubulins lack the specific 4-6 residue insertion in the H1-B2 loop region observed in other Rhizaria.

Kinesins are microtubule-based motors that are considered distantly related to myosins based on their similarities in folded structure (Jon Kull et al., 1996; Kull and Endow, 2002). *Filoreta's* kinesin repertoire includes 37 kinesins, 18 of which have canonical alignments, while the remaining 19 have either truncated N or C termini, or additional insertions. Although there is limited data on protistan kinesins, the SAR members within Stramenopiles and Alveolates contain kinesin orthologs for each major family, with exception of Kinesin 7 and 18 in alveolates (Wickstead et al., 2010).

The other major microtubule motor, dynein, is conserved across the eukaryotic tree, and is composed of a four-unit complex of dynein heavy chains (DHC), light-intermediate or light chains (LC), and intermediate chains (IC). All nine dynein heavy chain families are projected to be present in the last eukaryotic common ancestor (LECA) based on extant species phylogenies (Wickstead, 2018). Eight of the nine major DHC families are responsible for flagellar/ciliary activity, where the outlier is a cytoplasmic dynein family providing minus-end directed transport along non-axonemal microtubules.

Filoreta includes 13 axonemal dynein heavy chains (8 inner arm, 4 outer arm), and 3 cytoplasmic dynein heavy chains including cytoplasmic dynein 1 and 2 (IFT dynein). It also contains Dynactin 1, 4, 5, and two copies of subunit p22. A Rhizarian cytoplasmic dynein-like ATPase with bidirectional transport was found in *Reticulomxya* and examined for its unusually rapid transport rates and polar "promiscuity" (Euteneuer et al., 1988; Koonce and Schliwa, 1985; Schliwa et al., 1991). Parallels have been drawn between the motor protein activity for long-

ranged transport in giant Rhizarian amoebae like Reticulomyxa, and the motors responsible for transport in neurons (Hirokawa et al., 1990).

Microtubule nucleation machinery is also conserved across eukaryotes, though not all lineages have the same set of nucleating components. The components that make up the microtubule nucleating gamma-tubulin ring complex (ɣ-TuRC) are present in the *Filoreta* genome and include GCP2, 3, 4, 5, 6, SAS6, and gamma tubulin (Kollman et al., 2008). *Filoreta* also has one homolog of XMAP215, a protein originally identified in *Xenopus laevis* egg extracts, that synergistically nucleates microtubules and promotes polymerization (King et al., 2020; Liu et al., 2021; Thawani et al., 2018).

End binding (EB) proteins are important for microtubule dynamics, growth and distribution, and localization of other microtubule interacting proteins (Bisgrove et al., 2008). We identified two EB1 homologs in *Filoreta*, each containing the conserved "BIM1" domain. One of the EB1 proteins also has an unusual C-terminal Nup88 domain, which is part of the nuclear pore complex. The discovery of this potentially novel EB1 could connect microtubule dynamics and nuclear pore complex (NPC) components and suggests a role in anchoring nuclei with the microtubule cytoskeleton.

Another microtubule associated protein family, MAP65, is important for its various and divergent activities including microtubule bundling, stabilizing in cells, and promoting flexibility of singlet microtubules in vitro (Mao et al., 2005; Portran et al., 2013). Different types of MAP65 characteristically bundle microtubules in parallel and antiparallel arrays. The *Filoreta* MAP65 is similar to the MAP65 orthologs PRC1 and Ase1, which have antiparallel bundling activity (Bieling et al., 2010; Gaillard et al., 2008; Loïodice et al., 2005).

Conserved and novel features of actin-based motility in *Filoreta*

Within the Rhizarian lineages, an actin duplication event occurred after the Forams and Retaria diverged from Cercozoa (*Filoreta*, *Gromia*, etc) (Krabberød et al., 2017). Our data aligns with this finding, as the five actin copies in *Filoreta* group closely together phylogenetically, in a distinct clade separated from the ARPs. We identified Arps 2 and 3, components of the Arp2/3 complex responsible for generating branched actin arrays, as well as Arps 1, 4, 5, 7 and 10, and twelve novel Arps, three of which are Rhizarian -specific (thus far found only in *Reticulomyxa* and *Filoreta*). Actin binding homologs including cofilin, filamin, gelsolin, and troponin are also present in the genome, indicating *Filoreta*'s actin cytoskeleton has the necessary interactors for canonical actin dynamics. We also found the actin-MT cytoskeleton crosslinkers including spectrin and coronin.

Filoreta's propensity to form long filopodia warranted investigation into actin filament bundling proteins such as fascin. While I did not identify a fascin homolog, I did find multiple plastin, espin and actinin homologs responsible for parallel actin filament bundling (Rajan et al., 2023).

Filoreta has at least eighteen myosins, including eight myosin I, two unusual myosin-II-like myosins, four myosin IV, a myosin 7-like containing a myth-FERM domain, and several Rhizarian myosin orphans. Myosins are a crucial component in cells driving motility, polarity, organelle transport and membrane trafficking, and are typically identified through their functionally conserved head domains (Goodson, 1994; Thompson and Langford, 2002). Myosin I and II are the earliest diverging myosins by phylogenetic analyses and are important for several different processes in cells, often with varying activities. In *Dictyostelium*, the different myosin I isoforms carry out distinct functions for motility, secretion, polarity, and membrane interactions (Jung et al., 2008; Novak et al., 1995). Myosin II proteins are required for actin-based

contractility, while myosin VII-like proteins include a MyTH4-FERM domain and are required for filopodial formation ((Petersen et al., 2016)).

Our phylogenetic analyses indicate *Filoreta* has a wider repertoire of myosin I than its other myosin families. The lack of a canonical myosin II in an amoeboid migratory cell type suggests that another mechanism may generate contractile forces at the trailing end of pseudopodia, as would be the case in the individual amoeboid stage and the syncytial stage of the *Filoreta* life cycle. One of the myosin II-like proteins also has similarity to myosin XVIII, which is similar in sequence similarity to myosin II, and is considered Holozoan-specific (Sebé-Pedrós et al., 2014; Taft and Latham, 2020).The potential presence of myosin XVIII-like proteins in *Filoreta* are unprecedented and suggests a broader distribution of this myosin type across the eukaryotes. *Filoreta* also has a myosin VII-like protein, including the MyTH4-FERM domains responsible for filopodial actin arrangements. Additionally, myosin IV and VII are reported to not coincide in the same lineages (Hodge and Cope, 2000; Thompson and Langford, 2002). The presence of these diverse myosin families and numerous orphans in *Filoreta* indicates that the Rhizarian lineage has unusual myosins in its repertoire and warrants further study. These findings have broad implications for the evolution and divergence of myosins and mechanisms of amoeboid motility across the eukaryotic lineages (Sebé-Pedrós et al., 2014).

SCAR proteins not present in Rhizaria

The SCAR/WAVE proteins recruit the branched actin nucleator Arp2/3 to polymerize an actin network at the edge of amoeboid pseudopodia, specifically in lamellipodia. To date, none of the identified SAR members (Stramenopiles, Alveolates, Rhizaria) include SCAR, but pseudopodial-type evidence within Rhizaria indicates a branched actin organization and nucleating mechanism

of similar effect to SCAR/WAVE activity (Fritz-Laylin et al., 2017). Within amoeboid cell types, those that do not utilize SCAR exhibit blebbing motility with Myosin II force generation, rather than actin polymerization-dependent pseudopodial extension (Paluch and Raz, 2013). While the Rhizarian amoebae *Guttulinopsis* does exhibit blebbing motility, many other lineages including *Filoreta, Gromia* and *Reticulomyxa* consistently form reticulopodia, filopodia and lamellipodia (Travis et al., 1983; Travis and Allen, 1981). For this reason, we suspect the Rhizaria have implemented a mechanism independent of SCAR for actin polymerization-dependent protrusion of the leading membrane edge. We identified two proteins with N-terminal WH1 domains and actin binding motifs, which we suspect may have activity similar to WASP, which has a C-terminal WH1 domain (Pollitt and Insall, 2009). Further investigation into the evolutionary background for this type of actin polymerization and functionality of these identified proteins in the Rhizarian clade is needed.

A predicted flagellate stage in *Filoreta*

Many Rhizaria exist either solely as flagellates or are at least partly composed of a flagellate stage in their life cycle (Cavalier-Smith et al., 2018). The *Filoreta* genome has all the proteins required to produce a functional motile flagellum (Figure 10, Table 4), but no one has directly observed flagellates in this or any other related *Filoreta* species yet. The presence of canonical axonemal/ciliary microtubule-associated proteins, motors and basal bodies indicates flagella are present in the genome and likely produced at some point in the *Filoreta* life cycle.

Flagellar proteins were also found in the *Reticulomyxa* genome analyses, where flagella-associated proteins were identified, but in cultures over the span of 12 years, no one ever observed the flagellate stage (Glockner et al., 2014). Other Rhizarian amoeboid protists

(Cercozoa) like *Limnofila*, have a documented brief flagellate stage (Bass et al., 2018; Nikolaev et al., 2004).

Predicted photoreception and phototransduction in *Filoreta*

Little is known about the Rhizarian supergroup's ability to detect and respond to light, aside from the phototactic-photosynthetic *Bigelowiela natans* and the Foraminifer *Amphistegina's* positive phototaxis along light gradients (Jékely, 2009; Zmiri et al., 1974). *Filoreta* responds negatively to intense light exposure either by retracting pseudopodia or initiating encystation, but also during imaging blinking light specifically (Chapter 3). We observed that to capture growth and development of the syncytial network, the light shutter must be set to "open" so that the light source does not repeatedly blink as it illuminates the sample.

Yet, in the genome we identified genes involved in light-detection pathways, including a rhodopsin kinase and associated signal transduction pathways, 11-cis-retinol dehydrogenase, all-trans-retinol 13,14-reductase, and the biosynthesis pathways for both retinol and carotenoid-terpenoid backbone molecules. Evidence of this light-detection phenomenon suggests that it is not purely an amoeboid response via localized metabolic response from increased temperature. In contrast, constant light does not elicit the same response, even though constant illumination at the same intensity would result in a greater temperature increase. The reaction is also not only initiated by broad-spectrum light, and can be induced via blinking fluorescent light in wavelengths from UV (very sensitive) to far-red. We hypothesize that *Filoreta's* rhodopsin kinase is similarly involved in the signal turnoff via phosphorylation of rhodopsin (RHO), the G protein- coupled receptor that initiates the phototransduction cascade (Horner et al., 2005). This rapid desensitization is essential for fast cell responses to changes in illumination, like blinking light.

Euglena's phototaxis functions via an adenylyl cyclase with a flavoprotein photoactivated adenylyl cyclase (PAC) (Ntefidou and Häder, 2005). After searching for PAC-like sequences in the Filoreta genome, we identified several adenylate/guanylate cyclases, but did not find any with a conserved BLUF domain (blue light detection) or any other light-activated domains. However, the extensive retinol/rhodopsin pathway components indicate that photoreception likely occurs without PAC activity.

Cell signaling in *Filoreta* and the presence of unusual neuron-like pathways

Eukaryotic multicellular life cycles and complex signaling pathways predate metazoan neuron repertoires (Heidel et al., 2011). Cells that interact with others in their population use similar mechanisms to receive and transduce signals across the plasma membrane, and downstream pathways to mediate the cell response to those signals. In the social amoeba *Dictyostelium*, numerous intercellular signaling pathways including cAMP and GABA have been identified that enable recognition and cooperative interaction in varied environments (Consalvo et al., 2019; Loomis, 2014).

In the *Filoreta* genome, there are numerous genes involved in cell-cell signaling, including many overlapping in neural development pathways. *Filoreta* has a homolog of ARMS/Kidins220, which in Metazoa is required for neurite branch development, and functions to convey extracellular stimuli to the intracellular effectors of cytoskeletal organization (Wu et al., 2009). There is also evidence of GABA signaling: at least four metabotropic GABA type B receptors, three ionotropic glutamate receptors, two voltage-dependent calcium channels, a metabotropic glutamate receptor (GRM4), and downstream interactor guanine nucleotide-binding protein G(i) subunit alpha (GNAI) (Terunuma, 2018).

Filoreta also has several synapse-specific proteins including a homolog of synaptic vesicle glycoprotein 2B (SV2B), which remarkably aligns more strongly with metazoan (vertebrate) homologs than with any similar protein among *Filoreta's* Rhizarian relatives, or even other protists. For its function in transmembrane transporter activity, SV2B forms a complex with synaptotagmin, syntaxin and SNARE-motif proteins, of which *Filoreta* has proteins with high similarity (Lazzell et al., 2004).

Syntaxins are an integral component to vesicle and endomembrane trafficking across the eukaryotic tree. Mammalian lineages have 15 syntaxin family proteins, while yeasts have seven. *Filoreta* has a relatively expanded repertoire of syntaxins, with 13 different proteins, the majority of which align closest to syntaxin-16, which is important for Golgi and trans-golgi-network transport. The neuronal specificity of syntaxins and their associated complexes depends on various factors, including number and type, and membrane binding domains. Neuron-associated syntaxins are Syntaxin 1A and 1B (Teng et al., 2001) and has a c-terminal transmembrane region and flanking leucine zipper layers, which form a hydrophobic seal that protects the ionic interactions of the SNARE core (Urbina and Gupton, 2020). *Filoreta* does contain a copy of a syntaxin that aligns with more closely with neuronal-specific Syntaxin 1A of vertebrates (Megalobrama) than other protists and contains domain architectures matching those in vertebrate Syntaxin 1A/B.

It remains unclear whether the proteins involved in membrane fusion and signaling in *Filoreta* are used like those in other "social" cell types or even neurons, because these pathways have not been investigated in Rhizarian systems. While the functions of these proteins in *Filoreta* are hypothetical, it makes sense that it would employ a wide repertoire of signaling pathways to ensure an efficient and dynamic response to its environment and ability to recognize "self." In

contrast to other amoeboid cell types, the network formation of *Filoreta* is non-migratory and instead expands as it explores its environment, leaving behind branches and loops that it can use for long-distanced transport. For this lifestyle, the syncytium must respond to external stimuli in a concerted manner that is distinct from the highly migratory cell types of other amoebae.

As in neurons, the plasma membrane of reticulopodial amoebae is massive and increases as surface area expands (Pfenninger, 2009). *Filoreta's* extensive network therefore requires a massive amount of biolipid synthesis to accommodate the expansion of the syncytium as it grows to cover multiple centimeters. We identified complete lipid biosynthesis pathways, and found components for sphingolipid biosynthesis and metabolism, which designates importance to membrane structure, lipid organization and energy potential. Sphingolipids specifically are involved in membrane organization, function, and interactions with lipid rafts, protein complexes and the cytoskeleton (Olsen and Færgeman, 2017). In neuronal cells, sphingolipids are responsible for maintaining membrane microdomains that allow for cells to spatially differentiate points of growth, cell contacts, and interactions like synapse formation.

For a cell that recognizes self, membrane proteins, sterols and lipid rafts are therefore crucial in regulating localized composition in response to external stimuli. *Filoreta* readily fuses to itself in anastomosing branches and within a clonal population of separate syncytia, highlighting the importance of these pathways for membrane remodeling and organization. Of the two other maintained *Filoreta* isolates (Chapter 1; Trunk River and Bodega Bay), none of the strains recognize and fuse to each other (Figure 6).

Conclusion

This new compelete genome of the Rhizarian syncytial amoeba *Filoreta ramosa* provide the foundation for its future study and development as a model system, and also as a new Rhizarian genome for comparative genomics of eukaryotes. The predicted cytoskeletal, nuclear, and environmental signalling proteins in this amoeba are reminiscent of those in similarly organized human cell types like neurons. Yet open questions remain. For example, the development of the syncytium from unicellular amoebae requires spatial differentiation and an organized structure, which involves extensive cytoskeletal remodeling. How conserved are these cytoskeletal proteins within the understudied Rhizaria and across the eukaryotic tree?

What are the branched actin polymerization protein repertoires across eukaryotes, if the SAR lineages don't include canonical proteins like SCAR? How do the nuclei in a syncytium like *Filoreta's* maintain autonomy and properly localize in a spatially differentiated complex multicellular network? How does *Filoreta* sense "self" and enable membrane autofusion, but discriminates between seemingly identical strains from other sources? I anticipate that this first description of the life cycle of *Filoreta* along with the genome analysis will spearhead future investigations into evolutionary relationships and functional pathways outlined here.

Methods

Filoreta isolation and culture

Brackish sediment samples were collected in July 2014 from the intertidal zone at Little Sippewissett Marsh in Woods Hole, MA (41°34'33.6"N 70°38'22.7"W). The sediment was serially diluted into artificial seawater and mixed with a 1:1 ratio of liquid culture of *Maribacter sp.* isolated from the same location at approximate 0.5 McFarland density (Chapter 1 Methods).

These mixed samples were spread onto artificial seawater plates (Chapter 1 Methods) and incubated at room temperature in a hydration chamber to prevent desiccation. A lawn of bacteria formed within 48 hours. After 5-7 days, notable plaques in the lawn were observed under phase microscopy to verify presence of amoebae. Well-isolated plaques were numbered and collected by gently scraping the surface with a sterile pipette tip. The cell material for each plaque was diluted and transferred to secondary isolation plates using the same serial dilution and bacterial addition procedure. When plaques formed on the secondary isolation plate, the cells were transferred to 25 cm^2 liquid culture flasks containing 10 ml of media to monitor growth using an inverted microscope. Strain SW4B followed nomenclature from the initial "SW" Sippewissett Marsh plate, as the fourth collected primary plaque, and second plaque "B" of the secondary isolates (Chapter 1).

All subsequent cultures were grown in sterile artificial seawater adjusted to pH 7.0, containing 5 mM MOPS buffer and 0.01% final concentration of Yeast Extract and Tryptone (filter sterilized). Syncytia were maintained by refreshing culture media every 24-48 hours and were observed to start encystation 72-96 hours after the last refresh.

18S ssu-based identification of isolate SW4B

Liquid cultures were scraped and pelleted, and genomic DNA was extracted using previously described phenol:chloroform methods (Chapter 1). The V2-7 regions of the isolate's 18S SSU rRNA gene were amplified using 82FE (5′-GAADCTGYGAAYGGCTC-3′) and 1391RE (5′-GGGCGGTGTGTACAARGRG-3′) universal eukaryote-specific primers (Chapter 1)(Dawson and Pace, 2002). Fragments were amplified from total gDNA using Easy-A High-Fidelity PCR Master Mix (Agilent Catalog #600640) in 25 µl reactions. Amplification was carried out with

initial 5m-94C, 30 cycles of; [1m-94C, 1m-55C, 4m-72C], final 10-minute extension at 72 °C. PCR products were verified with 1% agarose gel electrophoresis before cleanup using ExoSap (Chapter 1). Products were sequenced with 1391R primer by the UC Berkeley DNA sequencing facility.

Genomic DNA extraction

Ten 75cm^2 flasks were grown out to dense culture, then allowed to fully encyst by replacing media with sterile artificial seawater lacking nutrient sources. After 96 hours, all flasks were fully encysted. Cysts were collected by scraping with a cell scraper (GeneMate T-2443-1), transferred into 50-ml conical tubes (Falcon), then pelleted at 2,000 x g for 5 minutes at 4C in a benchtop centrifuge. A sample of the ~1 ml cell pellet was observed under phase contrast to contain intact cysts and clumps of residual bacteria that had grown in co-culture with the amoeba as food.

The cyst pellet was resuspended in an equal volume of P2 buffer (0.5%SDS) for 5 minutes to lyse residual bacterial cells, then washed three times in sterile artificial seawater, re-pelleting between each wash. Post wash, the pellet volume was approximately 250µl. A 10 µl aliquot of the washed cyst pellet was stained with DAPI and imaged using a Leica DMI6000B epifluorescent microscope to confirm retention of nuclei within cysts walls. All cysts observed contained nuclei and dense DAPI signal.

The remaining volume of unstained, washed cyst pellet was treated with 500µl 2X Buffer A (recipe), 60µl Proteinase K (20mg/ml), 10µl SDS (20%). The mixture was placed on a hot plate to incubate for 30 minutes at 50C.

Two 2-ml bead beating tubes (Sarstedt 72.693.005) were prepared with 0.3g of 0.5mm acid-washed Zirconia-silica beads (BioSpec #11079105z), 500µl phenol:chloroform:IAA (25:24:1) and 200µl SDS (20%). The heated lysate was transferred to these bead-beat tubes, then beat for 2 minutes at 2500 rpm using a benchtop beater, (Cole-Parmer Mini bead beater, SKU# BZB8906519). The tubes were pelleted at 16000 x g for 3 minutes at room temperature. The top aqueous layer (~600µl) was carefully transferred to a new 1.5 ml microcentrifuge tube containing equal volume of phenol:chloroform:IAA. The tubes were mixed by inverting 10 times, then centrifuged at 16000 x g for 2 minutes. The top aqueous layer (~500 µl) was transferred to a new 1.5 ml microcentrifuge tube and 500 µl of 100% isopropanol and 50 µl of 3M sodium acetate (pH 5.2) were added. They were mixed by inverting 5 times, then placed on ice for 25 minutes. After icing, the tubes were centrifuged at 16000 x g for 20 minutes at 4C. The supernatant was aspirated using a vacuum line fitted with sterile slanted needle to avoid the DNA pellet. The pellet was then washed by adding 500 µl cold 80% ethanol, inverted 5x, then centrifuged for 5 minutes, for a total of two washes. After the second wash, the pellets were air-dried at room temperature for 30 minutes, then rehydrated in 50 µl 10mM Tris-HCl, and allowed to resuspend without pipetting before pooling volumes together.

The gDNA sample was quantified using a Qubit DNA Broad Range quantification kit, and 5 µl was run on a gel to verify quality and size. The final volume was calculated to contain 12 µg gDNA (120 ng/µl in 100 ul).

RNA extraction and library prep

Syncytial RNA was obtained from a total of six clonal 75 cm^2 culture flasks grown to maximal density. Syncytia were first washed to remove excess bacteria by pouring off spent media, rinsing with 50 ml of sterile artificial seawater, then removing the rinse before adding 2 ml of

TRI Reagent directly onto the culture surface. This was allowed to lyse for 30 seconds before scraping the surface with a sterile cell scraper to dislodge material. The lysed material was transferred to 2x 1.5 ml microcentrifuge tubes, vortexed for 30 seconds, then centrifuged to remove cell debris and unlysed cysts using an Eppendorf benchtop centrifuge at 16000 x g for 1 minute.

Cysts were prepared for RNA extraction by centrifugation at 1200 x g for 5 minutes, resuspended in sterile seawater, collected with a 40 µm cell strainer (Fisherbrand 22363547) and re-pelleted at 10000 x g. The volume of the resultant pellet was approximately 100 µl. Washed cysts were observed intact under light microscopy before suspension in TRI Reagent. An equal volume of zirconium beads was added and the sample was mechanically disrupted for 5 minutes on a benchtop vortex at level 10. After vortexing, a 10 µl aliquot of suspension was verified microscopically to contain broken and empty cysts. The samples were then centrifuged at 16000 x g for 1 minute to separate debris and empty cysts from the aqueous layer.

The supernatants of each sample type were then mixed with equal volumes of 100% ethanol. Total RNA was extracted using a Zymo RNA mini kit, including DNase treatment steps, and eluted into 50 µl (per column). The resultant total RNA was quantified using a Qubit fluorometer, then further extracted via polyA selection using Promega PolyATract bead kit. The polyA-selected RNA was eluted into a final volume of 200ul, then cleaned and concentrated using a Zymo RNA Clean and Concentrate column kit. The final elution volume was 20 µl each, (S=150 ng and C=50 ng) and stored at -80C until use.

DNA Libraries were prepared using a Zymo-Seq Ribofree® Total RNA Library Kit, with primer sets 18 and 19 for syncytia and cysts, respectively. The amplification included 12 cycles based on the total input RNA. Final Library elution volume was 20 µl, with S=10.2 ng/µl and C=13.4

ng/µl. A preliminary iSeq run indicated the presence of adapter dimers even after multiple cleanup steps in the Zymo-seq kit, so an additional size exclusion was performed using Ampure XL beads at an adjusted ratio of 1X volume of beads instead of 1.8X volume. The resultant DNA was quantified with Qubit HS DNA reagent at S=7.0 ng/µl and C=7.6 ng/µl, in a final volume of 20 µl.

Libraries were pooled to a concentration of >1ng/µl and sequenced at the sequencing facility of University of Illinois at Urbana-Champaign, on an SP lane on NovaSeq 6000 system (2 x 100bp Paired-Reads).

Genome Sequencing and Assembly

The long-read sequencing and assembly was done by Pacific Biosciences as a courtesy by Michael Weiand and Jonas Korlach, to supplement research for the Microbial Diversity Training course at the Marine Biological Laboratory in Woods Hole, MA. Assembly by SMRTAnalysis yielded a total of 466 contigs, 7.5 Mbp maximum contig length, and N50 of 3.5 Mbp. Contigs were analyzed with MiniKraken (Wood 2014) to remove bacterial contaminants. A total of 107 contigs with a max of 5.18 Mbp and an N50 of 2.54 Mbp was retained.

Identification and annotation of repetitive elements

Transposable elements (TEs) were identified by the Extensive De Novo TE Annotator (EDTA) v.2.0.0 and the non-redundant TE libraries provided to RepeatMasker v.4.0.9 with default parameters. Soft-masked eukaryotic contigs were used for further annotation.

Identification of telomeric and structural RNA sequences

Contigs were visualized in SnapGene Viewer and sequences were color-coded by GC content. End regions containing more than 200bp of short repetitive sequences were compared across all

contigs, and an identical consensus telomeric sequence was identified over eight of the 22 largest contigs.

The concatenated contigs were uploaded to the Galaxy EU server and tRNAs were identified by running tRNAscan (Galaxy version 0.4) on the genome set (Chan and Lowe, 2019). Ribosomal RNAs were identified using barrnap (Galaxy version 1.2.2) with "Kingdom: Eukaryote" defaults (Seemann, 2013).

Prediction of protein coding genes

Raw RNAseq reads were trimmed with Cutadapt (version 1.15) (Martin, 2011) and then aligned to the soft-masked eukaryotic contigs HISAT2 v.2.1.0 with the --dta parameter. Duplicates were marked with Picard (version 2.18) MarkDuplicates. Two rounds of BRAKER were then carried out for gene annotation. For the first round, aligned RNAseq reads were used to train gene prediction models of GeneMark-ET and AUGUSTUS using the BRAKER1 pipeline (Hoff et al., 2016). For the second round, protist protein sequences were retrieved from OrthoDB, combined with the predicted proteomes of *Paulinella micropora* (Lhee et al., 2021), *Plasmodiophora brassicae* (Schwelm et al., 2015) and *Reticulomyxa filosa* (Glockner et al., 2014) to train gene prediction with the BRAKER2 pipeline (Brůna et al., 2021). The output of the first and second rounds of annotation were then merged using TSEBRA (Gabriel et al., 2021) with default parameters. For each functional annotation, InterProScan (version 5.57-90.0) was used to predict potential protein domains based on sequence signatures with parameters '-iprlookup -appl Pfam'.

Genome Completeness: BUSCOs and KEGG Orthology pathway analyses

We ran BUSCO analyses on both the *Filoreta* genome assembly and predicted proteins with the gene sets for Eukaryota, Alveolata, Apicomplexa, Stramenopiles, and Fungi. (Dependencies and versions: hmmsearch: 3.1 metaeuk: 5.34c21f2.)

We also submitted the concatenated amino acid sequences in fasta format to GhostKOALA (Version 2.0) automatic annotation servers for additional analyses with KEGG Orthology assignment and pathway reconstruction (Kanehisa et al., 2016). Proteins identified in metabolic pathways were manually verified by blastp against the NCBI database to sequence similarity, conserved domains and checking for additional interactors not listed.

Literature Cited

Adam SA, Goldman RD. 2012. Insights into the Differences between the A- and B-Type Nuclear Lamins. *Adv Biol Regul* **52**:108–113. doi:10.1016/j.advenzreg.2011.11.001

Aoki-Kinoshita KF, Kanehisa M. 2007. Gene Annotation and Pathway Mapping in KEGG In: Bergman NH, editor. Comparative Genomics, Methods In Molecular Biology™. Totowa, NJ: Humana Press. pp. 71–91. doi:10.1007/978-1-59745-515-2_6

Bartolini F, Gundersen GG. 2010. Formins and Microtubules. *Biochim Biophys Acta* **1803**:164–173. doi:10.1016/j.bbamcr.2009.07.006

Basnet N, Nedozralova H, Crevenna AH, Bodakuntla S, Schlichthaerle T, Taschner M, Cardone G, Janke C, Jungmann R, Magiera MM, Biertümpfel C, Mizuno N. 2018. Direct induction of microtubule branching by microtubule nucleation factor SSNA1. *Nat Cell Biol* **20**:1172–1180. doi:10.1038/s41556-018-0199-8

Bass D, Tikhonenkov DV, Foster R, Dyal P, Janouškovec J, Keeling PJ, Gardner M, Neuhauser S, Hartikainen H, Mylnikov AP, Berney C. 2018. Rhizarian "Novel Clade 10" Revealed as Abundant and Diverse Planktonic and Terrestrial Flagellates, including Aquavolon n. gen. *J Eukaryot Microbiol* **65**:828–842. doi:10.1111/jeu.12524

Berney C, Geisen S, Van Wichelen J, Nitsche F, Vanormelingen P, Bonkowski M, Bass D. 2015. Expansion of the 'Reticulosphere': Diversity of Novel Branching and Network-forming Amoebae Helps to Define Variosea (Amoebozoa). *Protist* **166**:271–295. doi:10.1016/j.protis.2015.04.001

Bieling P, Telley IA, Surrey T. 2010. A Minimal Midzone Protein Module Controls Formation and Length of Antiparallel Microtubule Overlaps. *Cell* **142**:420–432. doi:10.1016/j.cell.2010.06.033

Bisgrove SR, Lee Y-RJ, Liu B, Peters NT, Kropf DL. 2008. The Microtubule Plus-End Binding Protein EB1 Functions in Root Responses to Touch and Gravity Signals in Arabidopsis. *The Plant Cell* **20**:396–410. doi:10.1105/tpc.107.056846

Bowser SS, Travis JL. 2000. Methods for Structural Studies of Reticulopodia, the Vital Foraminiferal "Soft Part." *Micropaleontology* **46**:47–56.

Brůna T, Hoff KJ, Lomsadze A, Stanke M, Borodovsky M. 2021. BRAKER2: automatic eukaryotic genome annotation with GeneMark-EP+ and AUGUSTUS supported by a protein database. *NAR Genomics and Bioinformatics* **3**:lqaa108. doi:10.1093/nargab/lqaa108

Burki F, Keeling PJ. 2014. Rhizaria. *Current Biology* **24**:R103–R107. doi:10.1016/j.cub.2013.12.025

Cavalier-Smith T, Chao EE, Lewis R. 2018. Multigene phylogeny and cell evolution of chromist infrakingdom Rhizaria: contrasting cell organisation of sister phyla Cercozoa and Retaria. *Protoplasma* **255**:1517–1574. doi:10.1007/s00709-018-1241-1

Chan PP, Lowe TM. 2019. tRNAscan-SE: Searching for tRNA genes in genomic sequences. *Methods Mol Biol* **1962**:1–14. doi:10.1007/978-1-4939-9173-0_1

Consalvo KM, RIJAL R, TANG Y, KIROLOS SA, SMITH MR, GOMER RH. 2019. Extracellular signaling in Dictyostelium. *Int J Dev Biol* **63**:395–405. doi:10.1387/ijdb.190259rg

Curtis BA, Tanifuji G, Burki F, Gruber A, Irimia M, Maruyama S, Arias MC, Ball SG, Gile GH, Hirakawa Y, Hopkins JF, Kuo A, Rensing SA, Schmutz J, Symeonidi A, Elias M, Eveleigh RJM, Herman EK, Klute MJ, Nakayama T, Oborník M, Reyes-Prieto A, Armbrust EV, Aves SJ, Beiko RG, Coutinho P, Dacks JB, Durnford DG, Fast NM, Green BR, Grisdale CJ, Hempel F, Henrissat B, Höppner MP, Ishida K-I, Kim E, Kořený L, Kroth PG, Liu Y, Malik S-B, Maier UG, McRose D, Mock T, Neilson JAD, Onodera NT, Poole AM, Pritham EJ, Richards TA, Rocap G, Roy SW, Sarai C, Schaack S, Shirato S, Slamovits CH, Spencer DF, Suzuki S, Worden AZ, Zauner S, Barry K, Bell C, Bharti AK, Crow JA, Grimwood J, Kramer R, Lindquist E, Lucas S, Salamov A, McFadden GI, Lane CE, Keeling PJ, Gray MW, Grigoriev IV, Archibald JM. 2012. Algal genomes reveal evolutionary mosaicism and the fate of nucleomorphs. *Nature* **492**:59–65. doi:10.1038/nature11681

Dawson SC, Pace NR. 2002. Novel kingdom-level eukaryotic diversity in anoxic environments. *Proc Natl Acad Sci U S A* **99**:8324–8329. doi:10.1073/pnas.062169599

del Campo J, Sieracki ME, Molestina R, Keeling P, Massana R, Ruiz-Trillo I. 2014. The others: our biased perspective of eukaryotic genomes. *Trends in Ecology & Evolution* **29**:252–259. doi:10.1016/j.tree.2014.03.006

Dogterom M, Koenderink GH. 2019. Actin-microtubule crosstalk in cell biology. *Nat Rev Mol Cell Biol* **20**:38–54. doi:10.1038/s41580-018-0067-1

Euteneuer U, Koonce MP, Pfister KK, Schliwa M. 1988. An ATPase with properties expected for the organelle motor of the giant amoeba, Reticulomyxa. *Nature* **332**:176–178. doi:10.1038/332176a0

Fish JL, Dehay C, Kennedy H, Huttner WB. 2008. Making bigger brains-the evolution of neural-progenitor-cell division. *J Cell Sci* **121**:2783–2793. doi:10.1242/jcs.023465

Fridolfsson HN, Starr DA. 2010. Kinesin-1 and dynein at the nuclear envelope mediate the bidirectional migrations of nuclei. *Journal of Cell Biology* **191**:115–128. doi:10.1083/jcb.201004118

Fritz-Laylin LK, Riel-Mehan M, Chen B-C, Lord SJ, Goddard TD, Ferrin TE, Nicholson-Dykstra SM, Higgs H, Johnson GT, Betzig E, Mullins RD. 2017. Actin-based protrusions of migrating neutrophils are intrinsically lamellar and facilitate direction changes. *eLife* **6**:e26990. doi:10.7554/eLife.26990

Gabriel L, Hoff KJ, Brůna T, Borodovsky M, Stanke M. 2021. TSEBRA: transcript selector for BRAKER. *BMC Bioinformatics* **22**:566. doi:10.1186/s12859-021-04482-0

Gaillard J, Neumann E, Van Damme D, Stoppin-Mellet V, Ebel C, Barbier E, Geelen D, Vantard M. 2008. Two microtubule-associated proteins of Arabidopsis MAP65s promote antiparallel microtubule bundling. *Mol Biol Cell* **19**:4534–4544. doi:10.1091/mbc.e08-04-0341

Gerber T, Loureiro C, Schramma N, Chen S, Jain A, Weber A, Weigert A, Santel M, Alim K, Treutlein B, Camp JG. 2022. Spatial transcriptomic and single-nucleus analysis reveals heterogeneity in a gigantic single-celled syncytium. *eLife* **11**:e69745. doi:10.7554/eLife.69745

Gibeaux R, Politi AZ, Philippsen P, Nédélec F. 2017. Mechanism of nuclear movements in a multinucleated cell. *MBoC* **28**:645–660. doi:10.1091/mbc.e16-11-0806

Gladfelter A, Berman J. 2009. Dancing genomes: fungal nuclear positioning. *Nat Rev Microbiol* **7**:875–886. doi:10.1038/nrmicro2249

Glockner G, Hulsmann N, Schleicher M, Noegel AA, Eichinger L, Gallinger C, Pawlowski J, Sierra R, Euteneuer U, Pillet L, Moustafa A, Platzer M, Groth M, Szafranski K, Schliwa M. 2014. The genome of the foraminiferan Reticulomyxa filosa. *Curr Biol* **24**:11–8. doi:10.1016/j.cub.2013.11.027

Gooday AJ, Holzmann M, Caulle C, Goineau A, Kamenskaya O, Weber AA-T, Pawlowski J. 2017. Giant protists (xenophyophores, Foraminifera) are exceptionally diverse in parts of the abyssal eastern Pacific licensed for polymetallic nodule exploration. *Biological Conservation* **207**:106–116. doi:10.1016/j.biocon.2017.01.006

Goodson HV. 1994. Molecular evolution of the myosin superfamily: application of phylogenetic techniques to cell biological questions. *Soc Gen Physiol Ser* **49**:141–157.

Grattepanche J-D, Walker LM, Ott BM, Paim Pinto DL, Delwiche CF, Lane CE, Katz LA. 2018. Microbial Diversity in the Eukaryotic SAR Clade: Illuminating the Darkness Between Morphology and Molecular Data. *BioEssays* **40**:1700198. doi:10.1002/bies.201700198

Habura A, Wegener L, Travis JL, Bowser SS. 2005. Structural and Functional Implications of an Unusual Foraminiferal β-Tubulin. *Molecular Biology and Evolution* **22**:2000–2009. doi:10.1093/molbev/msi190

Harder CB, Rønn R, Brejnrod A, Bass D, Al-Soud WA, Ekelund F. 2016. Local diversity of heathland Cercozoa explored by in-depth sequencing. *ISME J* **10**:2488–2497. doi:10.1038/ismej.2016.31

Heidel AJ, Lawal HM, Felder M, Schilde C, Helps NR, Tunggal B, Rivero F, John U, Schleicher M, Eichinger L, Platzer M, Noegel AA, Schaap P, Glöckner G. 2011. Phylogeny-wide analysis of social amoeba genomes highlights ancient origins for complex intercellular communication. *Genome Res* **21**:1882–1891. doi:10.1101/gr.121137.111

Hirokawa N, Sato-Yoshitake R, Yoshida T, Kawashima T. 1990. Brain dynein (MAP1C) localizes on both anterogradely and retrogradely transported membranous organelles in vivo. *Journal of Cell Biology* **111**:1027–1037. doi:10.1083/jcb.111.3.1027

Hodge T, Cope MJTV. 2000. A myosin family tree. *Journal of Cell Science* **113**:3353–3354. doi:10.1242/jcs.113.19.3353

Hoff KJ, Lange S, Lomsadze A, Borodovsky M, Stanke M. 2016. BRAKER1: Unsupervised RNA-Seq-Based Genome Annotation with GeneMark-ET and AUGUSTUS. *Bioinformatics* **32**:767–769. doi:10.1093/bioinformatics/btv661

Horner TJ, Osawa S, Schaller MD, Weiss ER. 2005. Phosphorylation of GRK1 and GRK7 by cAMP-dependent Protein Kinase Attenuates Their Enzymatic Activities*. *Journal of Biological Chemistry* **280**:28241–28250. doi:10.1074/jbc.M505117200

Huber MD, Gerace L. 2007. The size-wise nucleus: nuclear volume control in eukaryotes. *Journal of Cell Biology* **179**:583–584. doi:10.1083/jcb.200710156

Jay PY, Pham PA, Wong SA, Elson EL. 1995. A mechanical function of myosin II in cell motility. *J Cell Sci* **108 (Pt 1)**:387–393. doi:10.1242/jcs.108.1.387

Jékely G. 2009. Evolution of phototaxis. *Philos Trans R Soc Lond B Biol Sci* **364**:2795–2808. doi:10.1098/rstb.2009.0072

Johnson LK, Alexander H, Brown CT. 2019. Re-assembly, quality evaluation, and annotation of 678 microbial eukaryotic reference transcriptomes. *GigaScience* **8**:giy158. doi:10.1093/gigascience/giy158

Jon Kull F, Sablin EP, Lau R, Fletterick RJ, Vale RD. 1996. Crystal structure of the kinesin motor domain reveals a structural similarity to myosin. *Nature* **380**:550–555. doi:10.1038/380550a0

Jung HS, Burgess SA, Billington N, Colegrave M, Patel H, Chalovich JM, Chantler PD, Knight PJ. 2008. Conservation of the regulated structure of folded myosin 2 in species separated by at least 600 million years of independent evolution. *Proceedings of the National Academy of Sciences* **105**:6022–6026. doi:10.1073/pnas.0707846105

Kanehisa M, Sato Y, Morishima K. 2016. BlastKOALA and GhostKOALA: KEGG Tools for Functional Characterization of Genome and Metagenome Sequences. *J Mol Biol* **428**:726–731. doi:10.1016/j.jmb.2015.11.006

Kim DI, Birendra K, Roux KJ. 2015. Making the LINC: SUN and KASH protein interactions. *Biol Chem* **396**:295–310. doi:10.1515/hsz-2014-0267

King BR, Moritz M, Kim H, Agard DA, Asbury CL, Davis TN. 2020. XMAP215 and γ-tubulin additively promote microtubule nucleation in purified solutions. *MBoC* **31**:2187–2194. doi:10.1091/mbc.E20-02-0160

Kollman JM, Zelter A, Muller EGD, Fox B, Rice LM, Davis TN, Agard DA. 2008. The Structure of the γ-Tubulin Small Complex: Implications of Its Architecture and Flexibility for Microtubule Nucleation. *Mol Biol Cell* **19**:207–215. doi:10.1091/mbc.E07-09-0879

Koonce MP, Schliwa M. 1985. Bidirectional organelle transport can occur in cell processes that contain single microtubules. *J Cell Biol* **100**:322–326. doi:10.1083/jcb.100.1.322

Kopf A, Renkawitz J, Hauschild R, Girkontaite I, Tedford K, Merrin J, Thorn-Seshold O, Trauner D, Häcker H, Fischer K-D, Kiermaier E, Sixt M. 2020. Microtubules control cellular shape and coherence in amoeboid migrating cells. *J Cell Biol* **219**:e201907154. doi:10.1083/jcb.201907154

Krabberød AK, Orr RJS, Bråte J, Kristensen T, Bjørklund KR, Shalchian-Tabrizi K. 2017. Single Cell Transcriptomics, Mega-Phylogeny, and the Genetic Basis of Morphological Innovations in Rhizaria. *Mol Biol Evol* **34**:1557–1573. doi:10.1093/molbev/msx075

Kull FJ, Endow SA. 2002. Kinesin: switch I & II and the motor mechanism. *Journal of cell science* **115**:15–23.

Lawrence EJ, Arpag G, Arnaiz C, Zanic M. 2021. SSNA1 stabilizes dynamic microtubules and detects microtubule damage. *eLife* **10**:e67282. doi:10.7554/eLife.67282

Lazzell DR, Belizaire R, Thakur P, Sherry DM, Janz R. 2004. SV2B Regulates Synaptotagmin 1 by Direct Interaction*. *Journal of Biological Chemistry* **279**:52124–52131. doi:10.1074/jbc.M407502200

Lhee D, Lee J, Ettahi K, Cho CH, Ha J-S, Chan Y-F, Zelzion U, Stephens TG, Price DC, Gabr A, Nowack ECM, Bhattacharya D, Yoon HS. 2021. Amoeba Genome Reveals Dominant Host Contribution to Plastid Endosymbiosis. *Molecular Biology and Evolution* **38**:344–357. doi:10.1093/molbev/msaa206

Liu P, Würtz M, Zupa E, Pfeffer S, Schiebel E. 2021. Microtubule nucleation: The waltz between γ-tubulin ring complex and associated proteins. *Curr Opin Cell Biol* **68**:124–131. doi:10.1016/j.ceb.2020.10.004

Liu X, Li F, Li D, Ma E, Zhang W, Zhu KY, Zhang J. 2013. Molecular and Functional Analysis of UDP-N-Acetylglucosamine Pyrophosphorylases from the Migratory Locust, Locusta migratoria. *PLoS One* **8**:e71970. doi:10.1371/journal.pone.0071970

Loïodice I, Staub J, Setty TG, Nguyen N-PT, Paoletti A, Tran PT. 2005. Ase1p Organizes Antiparallel Microtubule Arrays during Interphase and Mitosis in Fission Yeast. *MBoC* **16**:1756–1768. doi:10.1091/mbc.e04-10-0899

Loomis WF. 2014. Cell signaling during development of Dictyostelium. *Dev Biol* **391**:1–16. doi:10.1016/j.ydbio.2014.04.001

MacRae TH, Langdon CM. 1989. Tubulin synthesis, structure, and function: what are the relationships? *Biochem Cell Biol* **67**:770–790. doi:10.1139/o89-116

Makarov AA, Padilla-Mejia NE, Field MC. 2021. Evolution and diversification of the nuclear pore complex. *Biochemical Society Transactions* **49**:1601–1619. doi:10.1042/BST20200570

Mao T, Jin L, Li H, Liu B, Yuan M. 2005. Two Microtubule-Associated Proteins of the Arabidopsis MAP65 Family Function Differently on Microtubules. *Plant Physiol* **138**:654–662. doi:10.1104/pp.104.052456

Markus S, Marzo M, McKenney R. 2020. New insights into the mechanism of dynein motor regulation by lissencephaly-1. *eLife* **9**. doi:10.7554/eLife.59737

Martin M. 2011. Cutadapt removes adapter sequences from high-throughput sequencing reads. *EMBnet.journal* **17**:10–12. doi:10.14806/ej.17.1.200

Mylnikov AP, Weber F, Jürgens K, Wylezich C. 2015. Massisteria marina has a sister: Massisteria voersi sp. nov., a rare species isolated from coastal waters of the Baltic Sea. *European Journal of Protistology* **51**:299–310. doi:10.1016/j.ejop.2015.05.002

Nikolaev SI, Berney C, Fahrni JF, Bolivar I, Polet S, Mylnikov AP, Aleshin VV, Petrov NB, Pawlowski J. 2004. The twilight of Heliozoa and rise of Rhizaria, an emerging supergroup of amoeboid eukaryotes. *Proc Natl Acad Sci U S A* **101**:8066–8071. doi:10.1073/pnas.0308602101

Novak KD, Peterson MD, Reedy MC, Titus MA. 1995. Dictyostelium myosin I double mutants exhibit conditional defects in pinocytosis. *Journal of Cell Biology* **131**:1205–1221. doi:10.1083/jcb.131.5.1205

Ntefidou M, Häder D-P. 2005. Photoactivated adenylyl cyclase (PAC) genes in the flagellate Euglena gracilis mutant strains. *Photochem Photobiol Sci* **4**:732–739. doi:10.1039/B502002F

Olsen ASB, Færgeman NJ. 2017. Sphingolipids: membrane microdomains in brain development, function and neurological diseases. *Open Biology* **7**:170069. doi:10.1098/rsob.170069

Orokos DD, Cole RW, Travis JL. 2000. Organelles are transported on sliding microtubules in Reticulomyxa. *Cell Motility* **47**:296–306. doi:10.1002/1097-0169(200012)47:4<296::AID-CM4>3.0.CO;2-4

Orokos DD, Travis JL. 1997. Cell surface and organelle transport share the same enzymatic properties in Reticulomyxa. *Cell Motility* **38**:270–277. doi:10.1002/(SICI)1097-0169(1997)38:3<270::AID-CM5>3.0.CO;2-9

Orsi WD, Morard R, Vuillemin A, Eitel M, Wörheide G, Milucka J, Kucera M. 2020. Anaerobic metabolism of Foraminifera thriving below the seafloor. *ISME J* **14**:2580–2594. doi:10.1038/s41396-020-0708-1

Paluch EK, Raz E. 2013. The role and regulation of blebs in cell migration. *Curr Opin Cell Biol* **25**:582–590. doi:10.1016/j.ceb.2013.05.005

Petersen KJ, Goodson HV, Arthur AL, Luxton GWG, Houdusse A, Titus MA. 2016. MyTH4-FERM myosins have an ancient and conserved role in filopod formation. *Proc Natl Acad Sci U S A* **113**:E8059–E8068. doi:10.1073/pnas.1615392113

Pfenninger KH. 2009. Plasma membrane expansion: a neuron's Herculean task. *Nat Rev Neurosci* **10**:251–261. doi:10.1038/nrn2593

Pollitt AY, Insall RH. 2009. WASP and SCAR/WAVE proteins: the drivers of actin assembly. *J Cell Sci* **122**:2575–2578. doi:10.1242/jcs.023879

Portran D, Zoccoler M, Gaillard J, Stoppin-Mellet V, Neumann E, Arnal I, Martiel JL, Vantard M. 2013. MAP65/Ase1 promote microtubule flexibility. *MBoC* **24**:1964–1973. doi:10.1091/mbc.e13-03-0141

Rajan S, Kudryashov DS, Reisler E. 2023. Actin Bundles Dynamics and Architecture. *Biomolecules* **13**:450. doi:10.3390/biom13030450

Roberts SE, Gladfelter AS. 2015. Nuclear autonomy in multinucleate fungi. *Curr Opin Microbiol* **28**:60–65. doi:10.1016/j.mib.2015.08.009

Schliwa M, Shimizu T, Vale RD, Euteneuer U. 1991. Nucleotide specificities of anterograde and retrograde organelle transport in Reticulomyxa are indistinguishable. *J Cell Biol* **112**:1199–1203. doi:10.1083/jcb.112.6.1199

Schwelm A, Fogelqvist J, Knaust A, Jülke S, Lilja T, Bonilla-Rosso G, Karlsson M, Shevchenko A, Dhandapani V, Choi SR, Kim HG, Park JY, Lim YP, Ludwig-Müller J, Dixelius C. 2015. The Plasmodiophora brassicae genome reveals insights in its life cycle and ancestry of chitin synthases. *Sci Rep* **5**:11153. doi:10.1038/srep11153

Sebé-Pedrós A, Grau-Bové X, Richards TA, Ruiz-Trillo I. 2014. Evolution and Classification of Myosins, a Paneukaryotic Whole-Genome Approach. *Genome Biology and Evolution* **6**:290–305. doi:10.1093/gbe/evu013

Seemann T. 2013. Barrnap.

Serpeloni M, Vidal NM, Goldenberg S, Ávila AR, Hoffmann FG. 2011. Comparative genomics of proteins involved in RNA nucleocytoplasmic export. *BMC Evolutionary Biology* **11**:7. doi:10.1186/1471-2148-11-7

Solnica-Krezel L, Burland TG, Dove WF. 1991. Variable pathways for developmental changes of mitosis and cytokinesis in Physarum polycephalum. *J Cell Biol* **113**:591–604. doi:10.1083/jcb.113.3.591

Taft MH, Latham SL. 2020. Myosin XVIII. *Adv Exp Med Biol* **1239**:421–438. doi:10.1007/978-3-030-38062-5_19

Teng FYH, Wang Y, Tang BL. 2001. The syntaxins. *Genome Biology* **2**:reviews3012.1. doi:10.1186/gb-2001-2-11-reviews3012

Terunuma M. 2018. Diversity of structure and function of GABAB receptors: a complexity of GABAB-mediated signaling. *Proc Jpn Acad Ser B Phys Biol Sci* **94**:390–411. doi:10.2183/pjab.94.026

Thawani A, Kadzik RS, Petry S. 2018. XMAP215 is a microtubule nucleation factor that functions synergistically with the γ-tubulin ring complex. *Nat Cell Biol* **20**:575–585. doi:10.1038/s41556-018-0091-6

Thompson RF, Langford GM. 2002. Myosin superfamily evolutionary history. *The Anatomical Record* **268**:276–289. doi:10.1002/ar.10160

Travis JL, Allen RD. 1981. Studies on the motility of the foraminifera. I. Ultrastructure of the reticulopodial network of Allogromia laticollaris (Arnold). *Journal of Cell Biology* **90**:211–221. doi:10.1083/jcb.90.1.211

Travis JL, Kenealy JF, Allen RD. 1983. Studies on the motility of the foraminifera. II. The dynamic microtubular cytoskeleton of the reticulopodial network of Allogromia laticollaris. *J Cell Biol* **97**:1668–1676. doi:10.1083/jcb.97.6.1668

Trokter M, Surrey T. 2012. LIS1 Clamps Dynein to the Microtubule. *Cell* **150**:877–879. doi:10.1016/j.cell.2012.08.010

Tyszka J, Bickmeyer U, Raitzsch M, Bijma J, Kaczmarek K, Mewes A, Topa P, Janse M. 2019. Form and function of F-actin during biomineralization revealed from live experiments on foraminifera. *Proc Natl Acad Sci U S A* **116**:4111–4116. doi:10.1073/pnas.1810394116

Umeshima H, Hirano T, Kengaku M. 2007. Microtubule-based nuclear movement occurs independently of centrosome positioning in migrating neurons. *Proceedings of the National Academy of Sciences* **104**:16182–16187. doi:10.1073/pnas.0708047104

Urbina FL, Gupton SL. 2020. SNARE-Mediated Exocytosis in Neuronal Development. *Front Mol Neurosci* **13**:133. doi:10.3389/fnmol.2020.00133

Wickstead B. 2018. 3 - The evolutionary biology of dyneins In: King SM, editor. Dyneins: Structure, Biology and Disease (Second Edition). Academic Press. pp. 100–138. doi:10.1016/B978-0-12-809471-6.00003-6

Wickstead B, Gull K, Richards TA. 2010. Patterns of kinesin evolution reveal a complex ancestral eukaryote with a multifunctional cytoskeleton. *BMC Evolutionary Biology* **10**:110. doi:10.1186/1471-2148-10-110

Wu SH, Arévalo JC, Sarti F, Tessarollo L, Gan W-B, Chao MV. 2009. ARMS/Kidins220 regulates dendritic branching and spine stability in vivo. *Dev Neurobiol* **69**:547–557. doi:10.1002/dneu.20723

Xiang X, Osmani AH, Osmani SA, Xin M, Morris NR. 1995. NudF, a nuclear migration gene in Aspergillus nidulans, is similar to the human LIS-1 gene required for neuronal migration. *Mol Biol Cell* **6**:297–310. doi:10.1091/mbc.6.3.297

Zmiri A, Kahan D, Hochstein S, Reiss Z. 1974. Phototaxis and Thermotaxis in Some Species of Amphistegina (Foraminifera)*. *The Journal of Protozoology* **21**:133–138. doi:10.1111/j.1550-7408.1974.tb03626.x

Figure 2.1: *Filoreta* origins

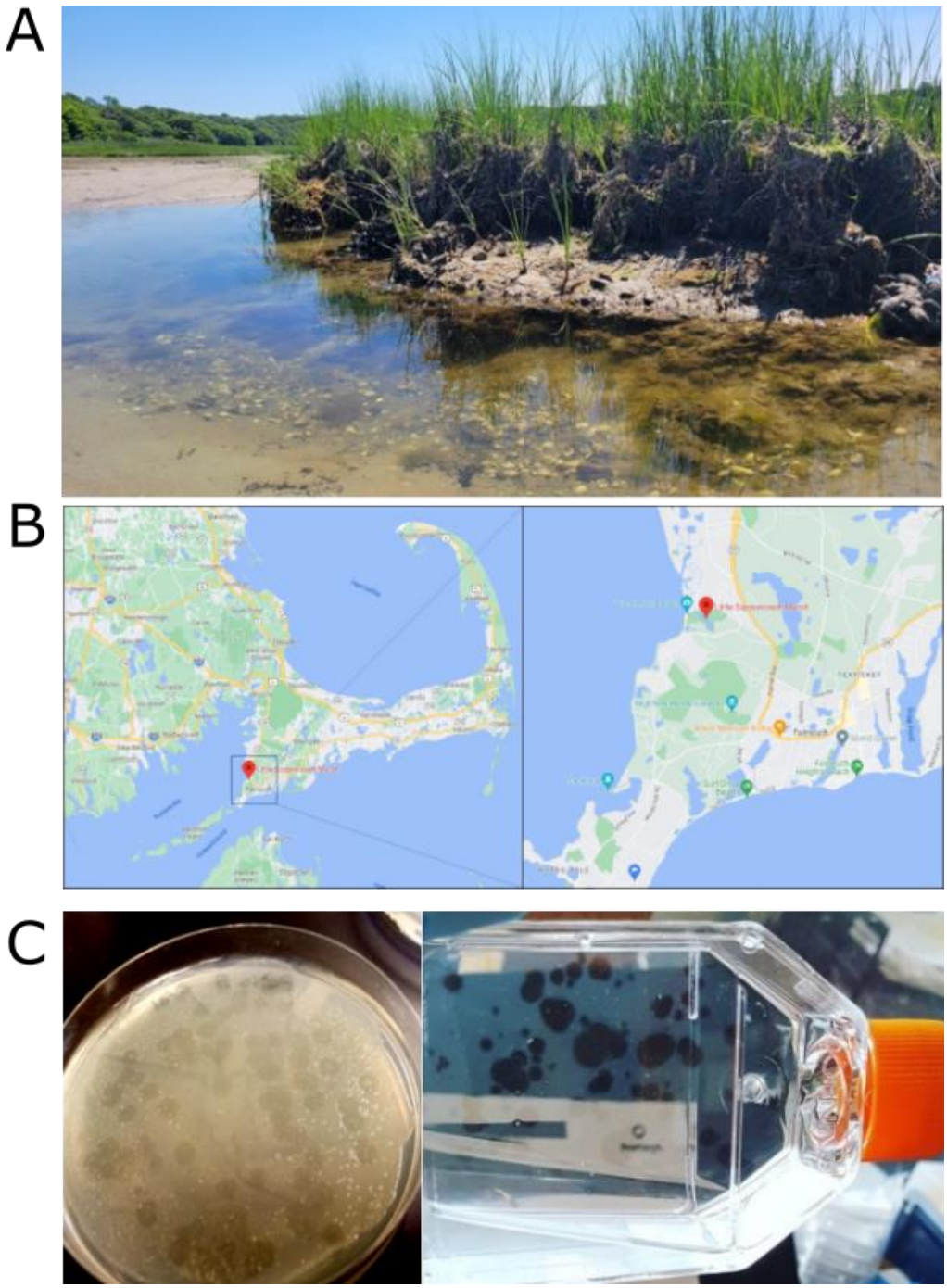

(A) The site of Sippewissett Marsh, MA where brackish sediments with high organic and sulfur content were collected (See Chapter 1 Methods).

(B) The collection site shown on a map.

(C) Examples of plaque formation of SW4B on artificial seawater plates and the culture surface inside a T25 culture flask.

Figure 2.2: Schematic of isolation method (Chapter 1 Methods)

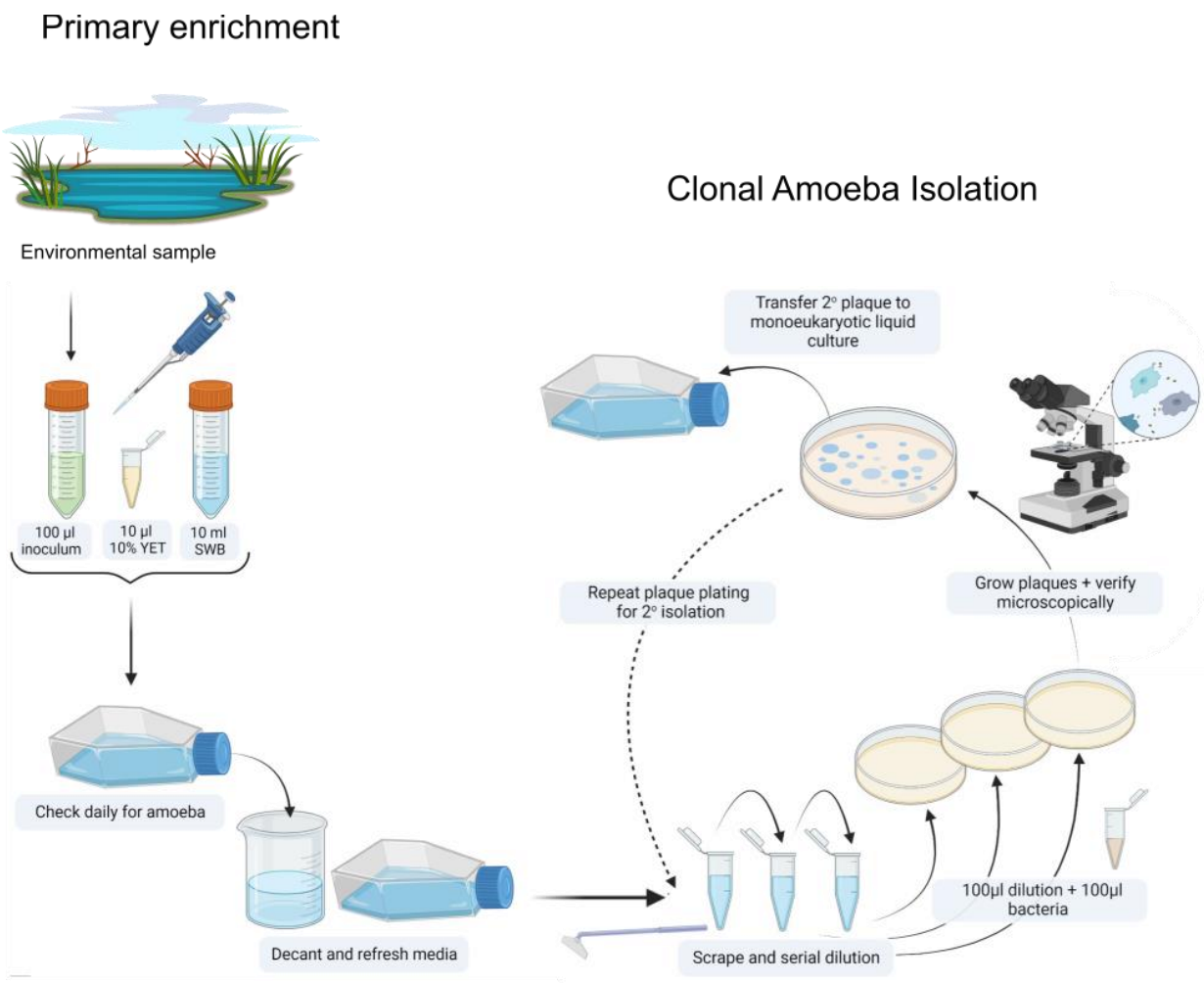

Figure 2.3: Genome size and statistics

A

Genome Stats	
Genome Size	35.8 Mb
Total Contigs	107
5.18 Mbp – 100 kbp	*22*
100 kbp – 5.2 kbp	*85*
N50	2,545,451 bp
GC %	46%
Coding %	55.50%
Introns/gene (avg)	4.4
Intron size (avg)	87.75 (median 47)
tRNA	155
rRNA	253 total
18S rRNA	*75*
28S rRNA	*77*
5.8S rRNA	*77*
5S rRNA	*24*

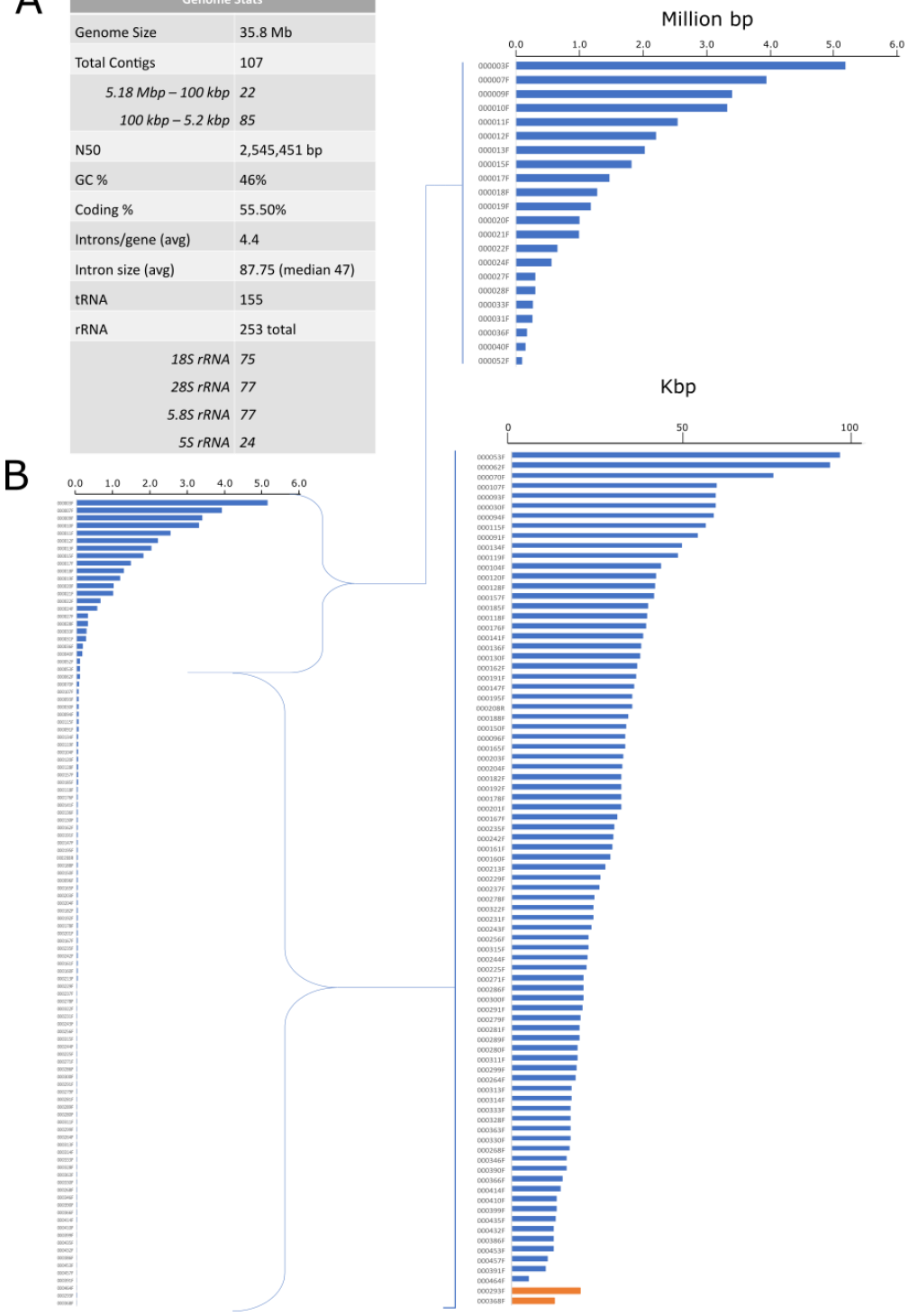

(A) Table showing general genome statistics.

(B) Histogram of contig sizes. The first 22 contigs listed are larger than 100 Kbp (top right). The remaining 85 contigs are less than 100 Kbp. Orange = mitochondrial contig sizes.

Figure 2.4: Genome Completeness by BUSCO and tRNAs

A

tRNA type	Code	Count
Alanine	Ala	13
Arginine	Arg	8
Asparagine	Asn	8
Aspartate	Asp	4
Cysteine	Cys	2
Glutamine	Gln	3
Glutamate	Glu	6
Glycine	Gly	8
Histidine	His	3
Isoleucine	Ile	11
Leucine	Leu	12
Lysine	Lys	6
Methionine	Met	13
Phenylalanine	Phe	6
Proline	Pro	4
Serine	Ser	8
Threonine	Thr	6
Tryptophan	Trp	4
Tyrosine	Tyr	4
Valine	Val	5
Pseudogene	Pseudo.	20
Undetermined	Undet.	1

B

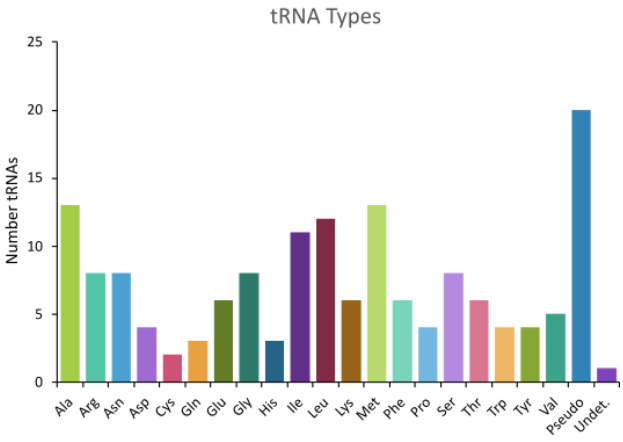

C

	Eukaryote BUSCO				Stramenopile BUSCO				Alveolate BUSCO			
Filoreta set	Genome		Protein		Genome		Protein		Genome		Protein	
Complete	182	71.4%	215	84.4%	82	82.0%	90	90.0%	151	88.3%	155	90.6%
Single copy	176	69.0%	196	76.9%	79	79.0%	79	79.0%	143	83.6%	135	78.9%
Duplicates	6	2.4%	19	7.5%	3	3.0%	11	11.0%	8	4.7%	20	11.7%
Fragmented	36	14.1%	6	2.4%	6	6.0%	0	0.0%	10	5.8%	5	2.9%
Missing	37	14.5%	34	13.2%	12	12.0%	10	0.0%	10	5.9%	11	6.5%
Total BUSCOs	255				100				171			

D

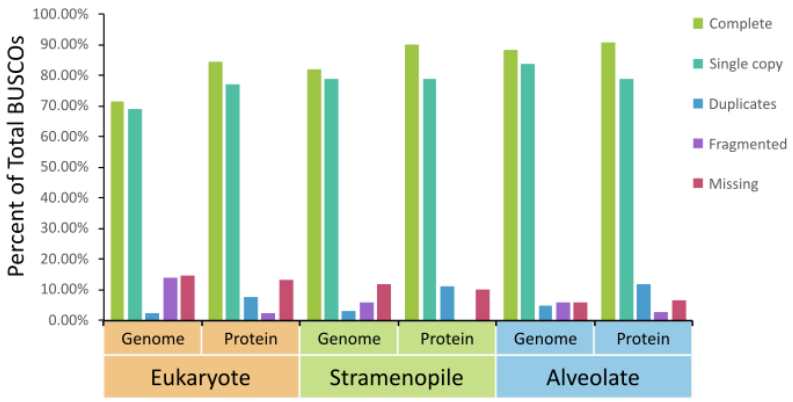

(A) Table showing complete set of identified tRNAs from tRNAscan on all contigs.

(B) Histogram of all tRNA types showing gene counts found in tRNAscan.

(C) Table of BUSCO analyses performed on genome and protein sets for the Eukaryote, Stramenopile and Alveolate BUSCO sets. (Versions: hmmsearch: 3.1; metaeuk: 5.34c21f2).

(D) Chart showing relative percent completeness based on *Filoreta* gene or protein set, organized by BUSCO set.

Figure 2.5: Repetitive elements in the genome

A

Type	Sequence	Contigs	Contig size
Telomere Start (~300-400bp)	CACTAACACTAA	000010F	3,324,632
		000015F	1,818,471
		000019F	1,179,452
Telomere End (~300-530bp)	TAGTGTTAGTGT	000003F	5,186,247
		000010F	3,324,632
		000012F	2,207,412
		000017F	1,475,713
		000021F	997,017
		000022F	653,810
0% GC region (~130-700bp)	TATTTTATTTTATTTT ATAAAATAAAATAAA	000003F	5,186,247
		000009F	3,407,696
		000019F	1,179,452
		000022F	653,810
	ATTATTATTATTATTA TAATAATAATAATAAT	000003F	5,186,247
		000007F	3,948,174
		000011F	2,545,451
		000013F	2,028,236
		000020F	1,002,739

B

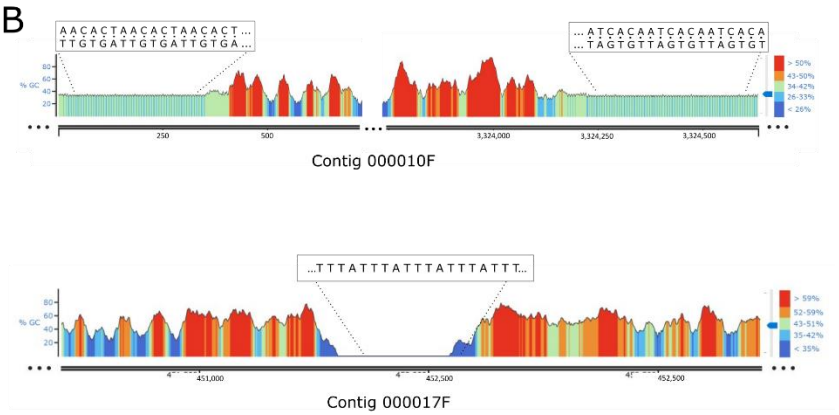

C

Repeat types	Total #	Avg length
TE motif	4338	351
A-Rich	4096	47.8
GA-Rich	770	50.5
G-Rich	87	49.76
(A)n repeats	2944	26
(T)n repeats	4501	29.7
(G)n repeats	62	30.2
(C)n repeats	76	29.6

D

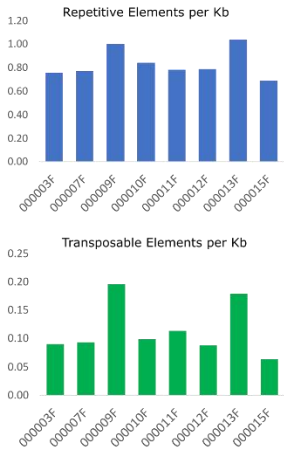

E

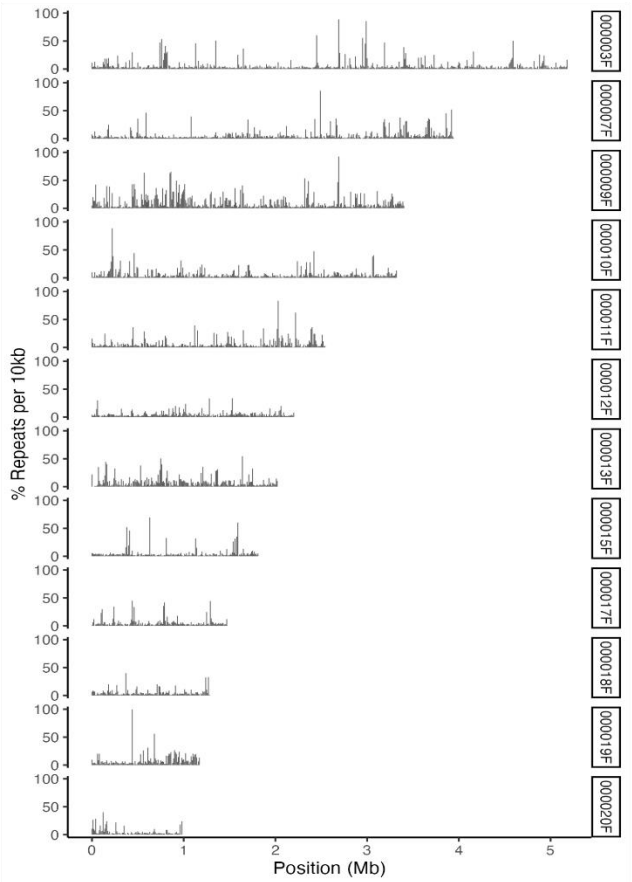

(A) Table showing Telomeric and 0% GC content regions at centers of contigs.

(B) Visualization of repetitive telomeric sequences, color coded by GC content (top). Lower panel shows visualization of regions containing AT-rich, 0% GC repeats in centers of contigs. Images generated using DNA sequence color features in SnapGene.

(C) Simplified table of repetitive elements found by RepeatMasker.

(D) Counts of repetitive elements and transposable elements represented per 1,000bp for each of the top 8 largest contigs.

(E) Maps of % repetitive elements per 10Kb across 12 largest contig lengths.

Figure 2.6: The life cycle of *Filoreta ramosa*

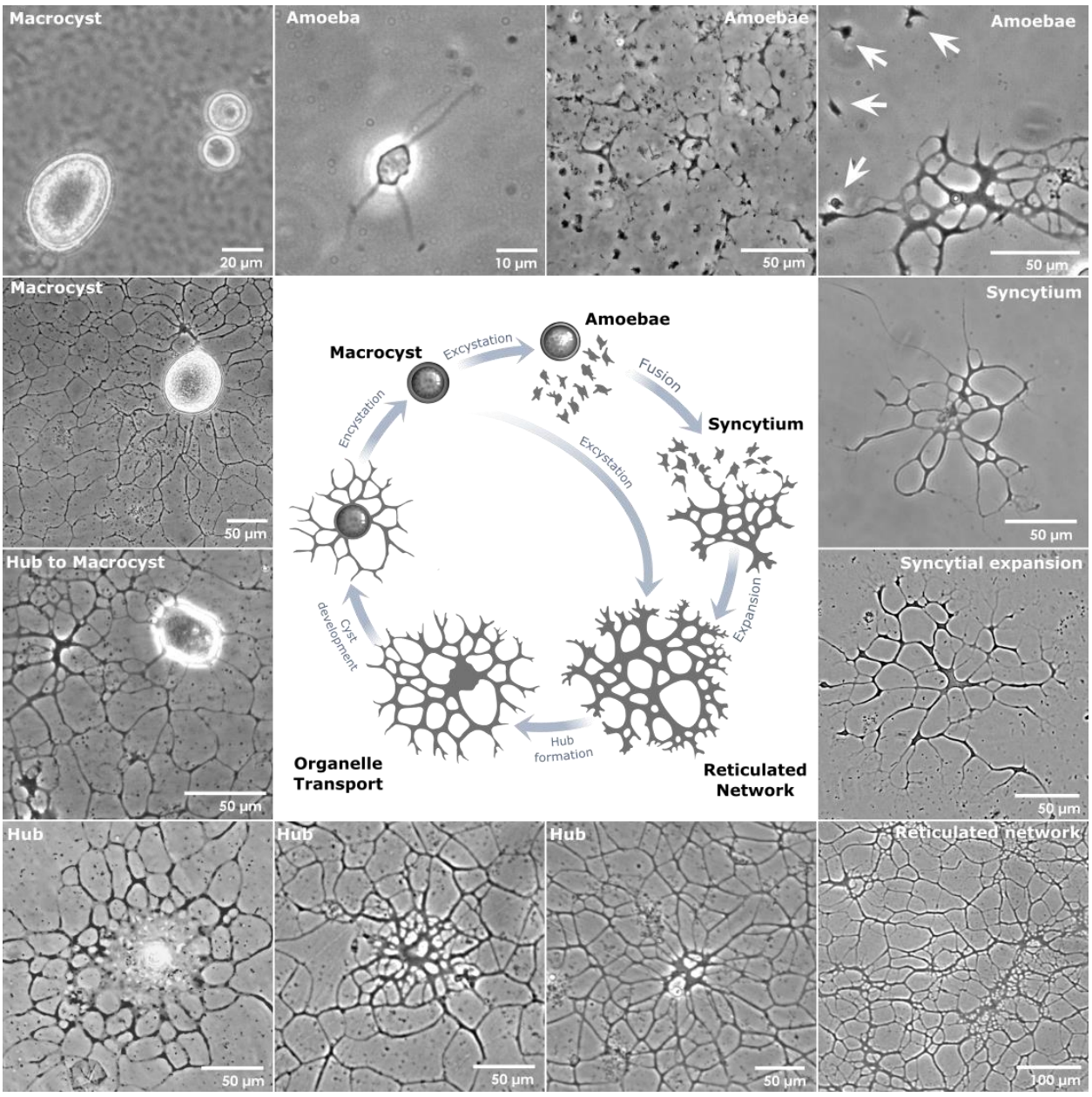

Figure 2.7: The *Filoreta* syncytial cytoskeleton has conserved proteins driving morphology

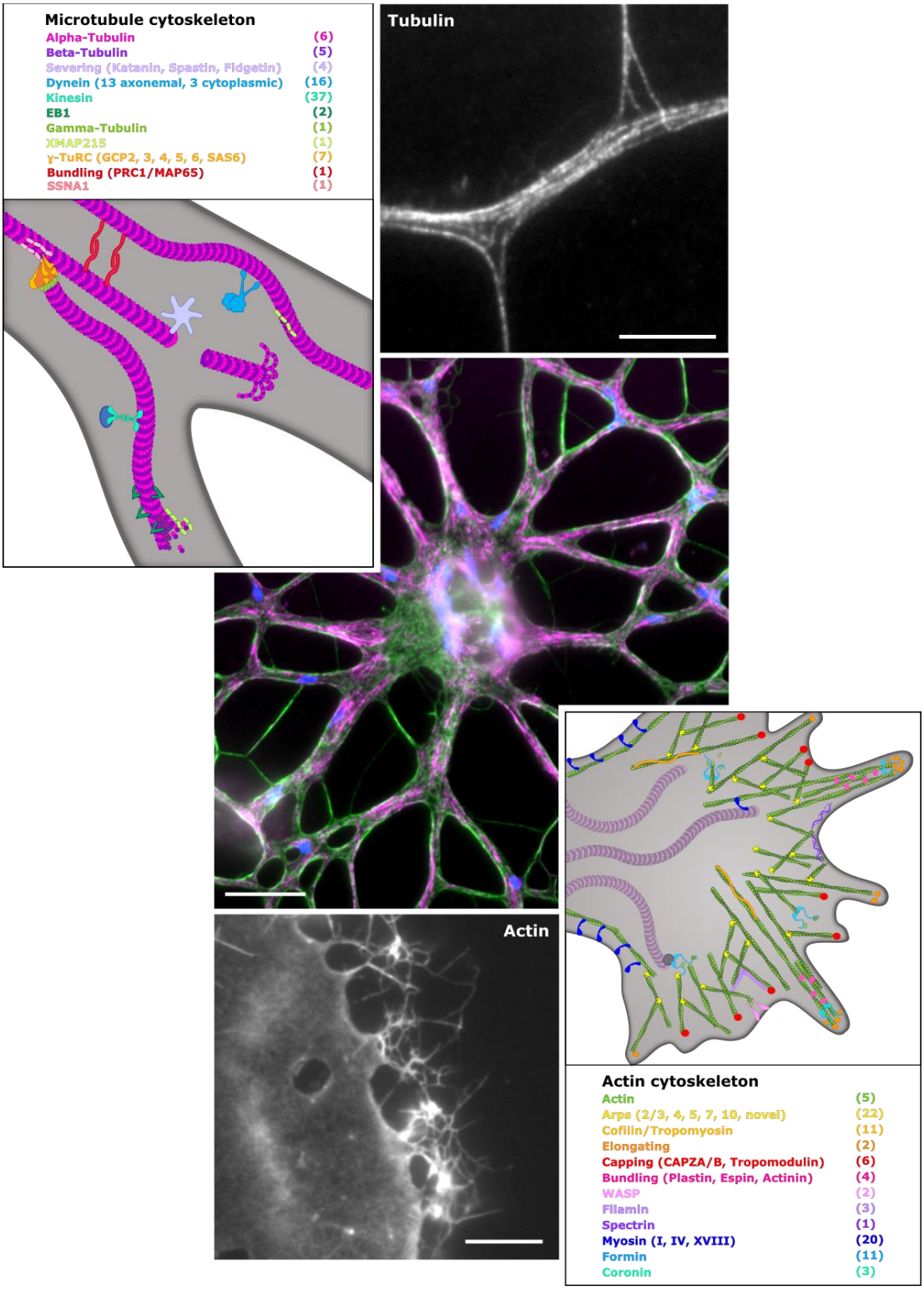

Representative images of *Filoreta* syncytium cytoskeletal network. Tubulin structures (top) and diagram with examples of protein families identified in the genome.

Actin in lamellipodia and filopodia (bottom) and diagram with examples of protein families identified in the genome. Scale bars = 10 μm.

Figure 2.8: Nuclear transport

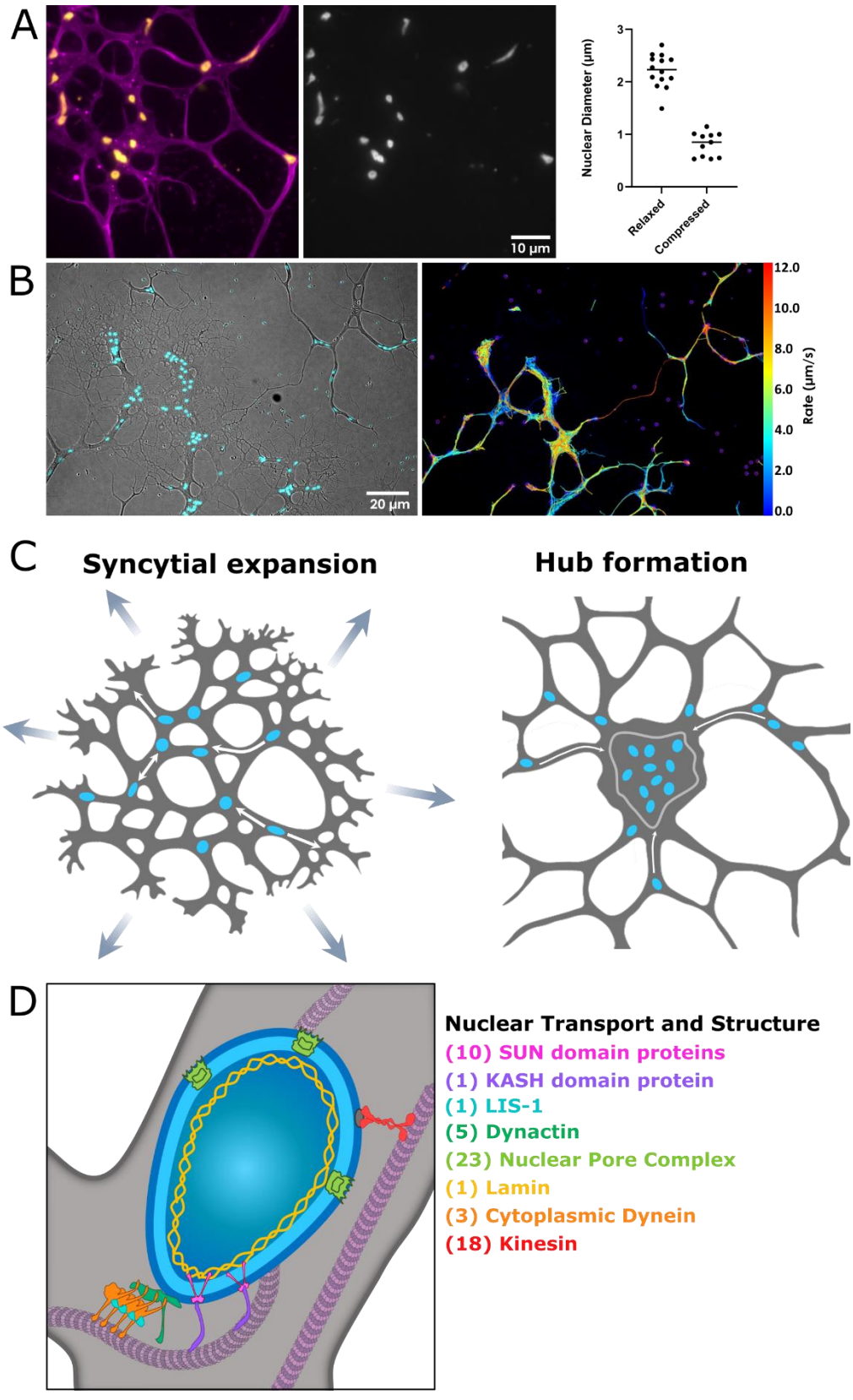

(A) Nuclei (yellow) visualized in syncytia (phalloidin=magenta) are compressed in branches during transport and relaxed at nodes and hubs. Quantitation of nuclear widths (right panel) illustrates the degree of compressibility. Average relaxed nuclear width ~ 2.2 µm, narrowest compressed nuclear width ~ 0.53 µm, less than 25% of original diameter. (Relaxed n=14, compressed n=11).

(B) Nuclear transport in the syncytium visualized by TrackMate overlay, color-coded by nuclear rate. Nuclear transport rates range up to ~12 µm/second.

(C) Diagram of nuclear transport during syncytial expansion and hub formation (nuclei = blue).

(D) Diagram of proteins identified that are involved in nuclear positioning, structure, and MT-based organelle-cargo transport.

Figure 2.9: The encystation phase of the *Filoreta* life cycle involves transport of nuclei into hubs that form macrocysts

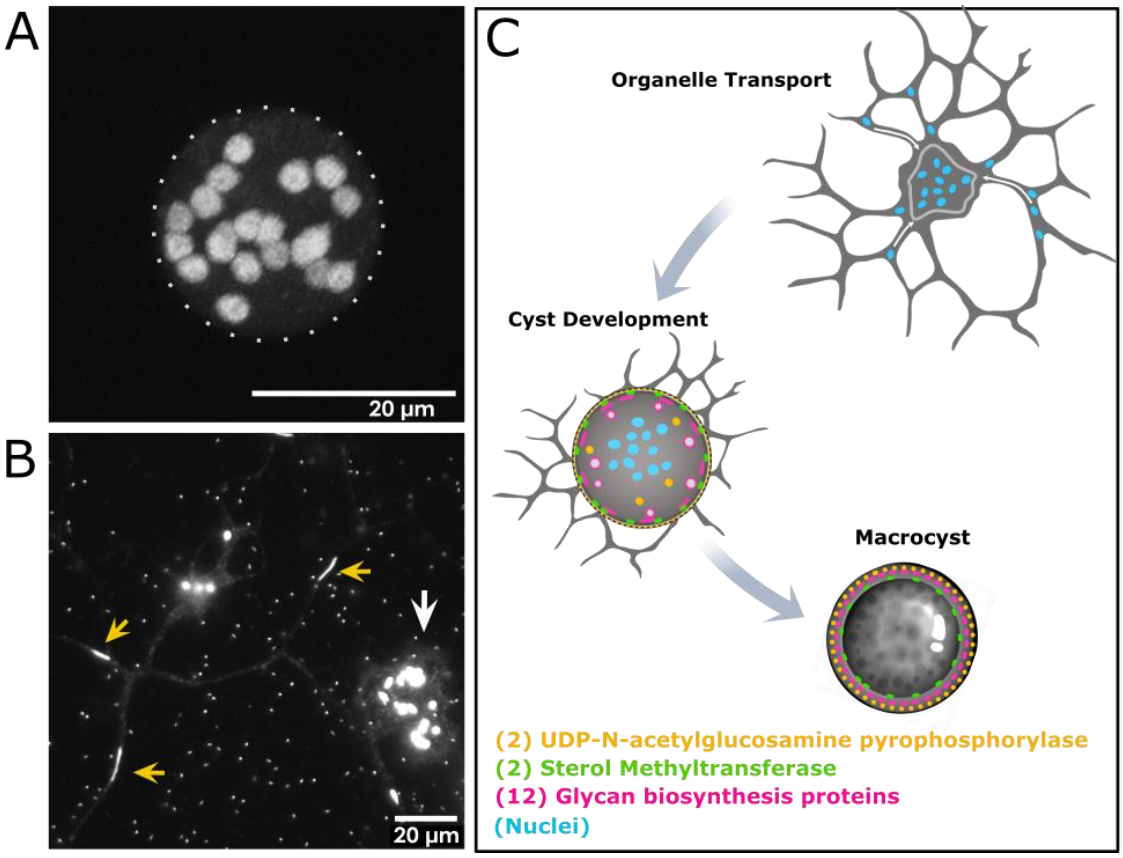

(A) Macrocysts contain numerous nuclei.

(B) Hub regions (white arrow) of the syncytium contain many nuclei as they begin to develop into cysts. Nuclei undergoing transport (yellow arrows) are often highly compressed as they travel through the network branches.

(C) Diagram depicting stages of macrocyst development and hypothesized cyst wall pathways identified.

Figure 2.10: Proteins indicative of a flagellate stage in *Filoreta*

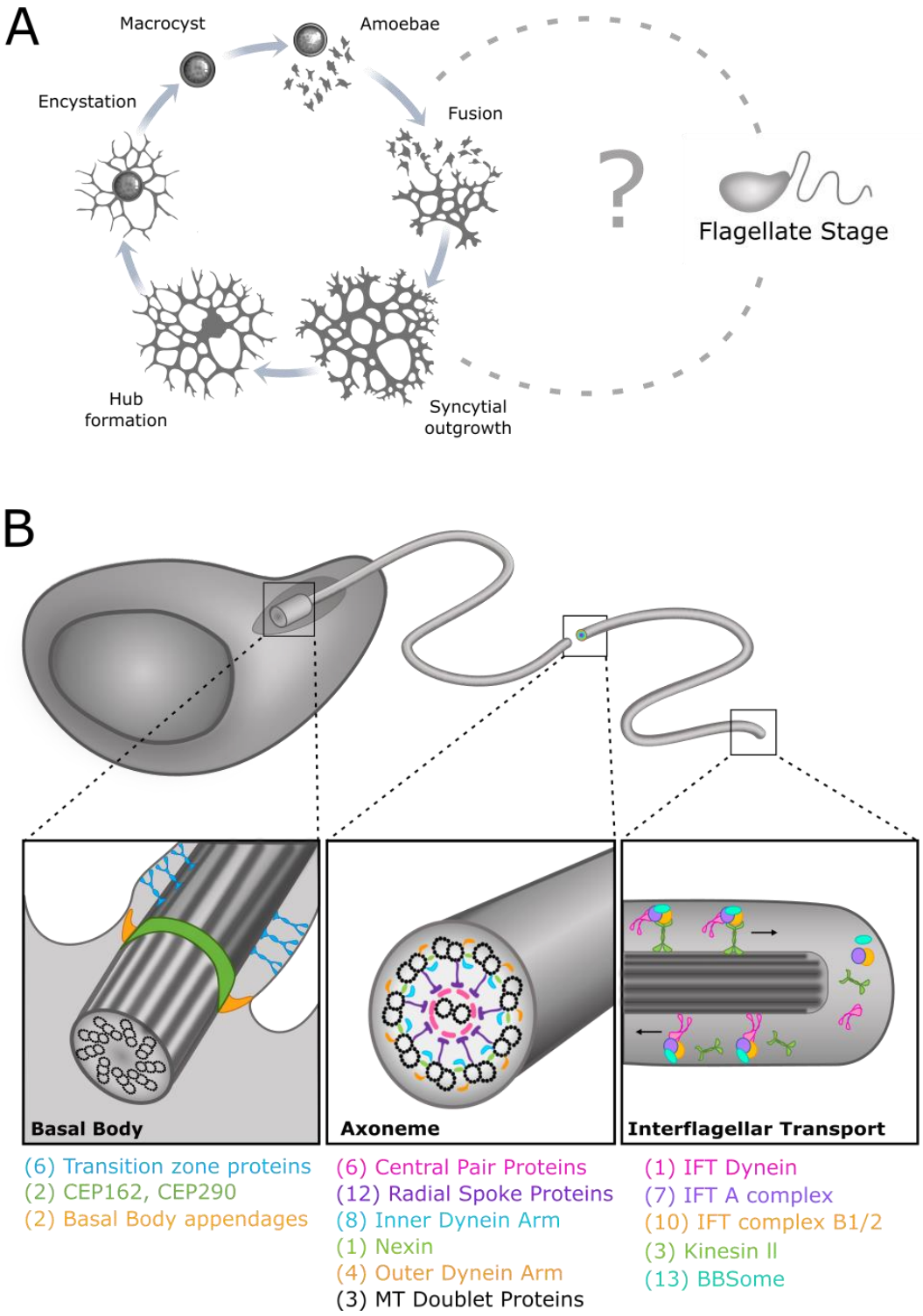

(A) Life cycle rendition with potential flagellate stage (unobserved). Flagellates may be specifically induced during excystation, or in syncytial form by environmental factors not provided in culture.

(B) Diagram showing proteins identified in the genome that are required for flagellum structure and function. Lists of proteins are further outlined in Table 5.

Figure 2.11: Self-recognition and membrane fusion the life cycle

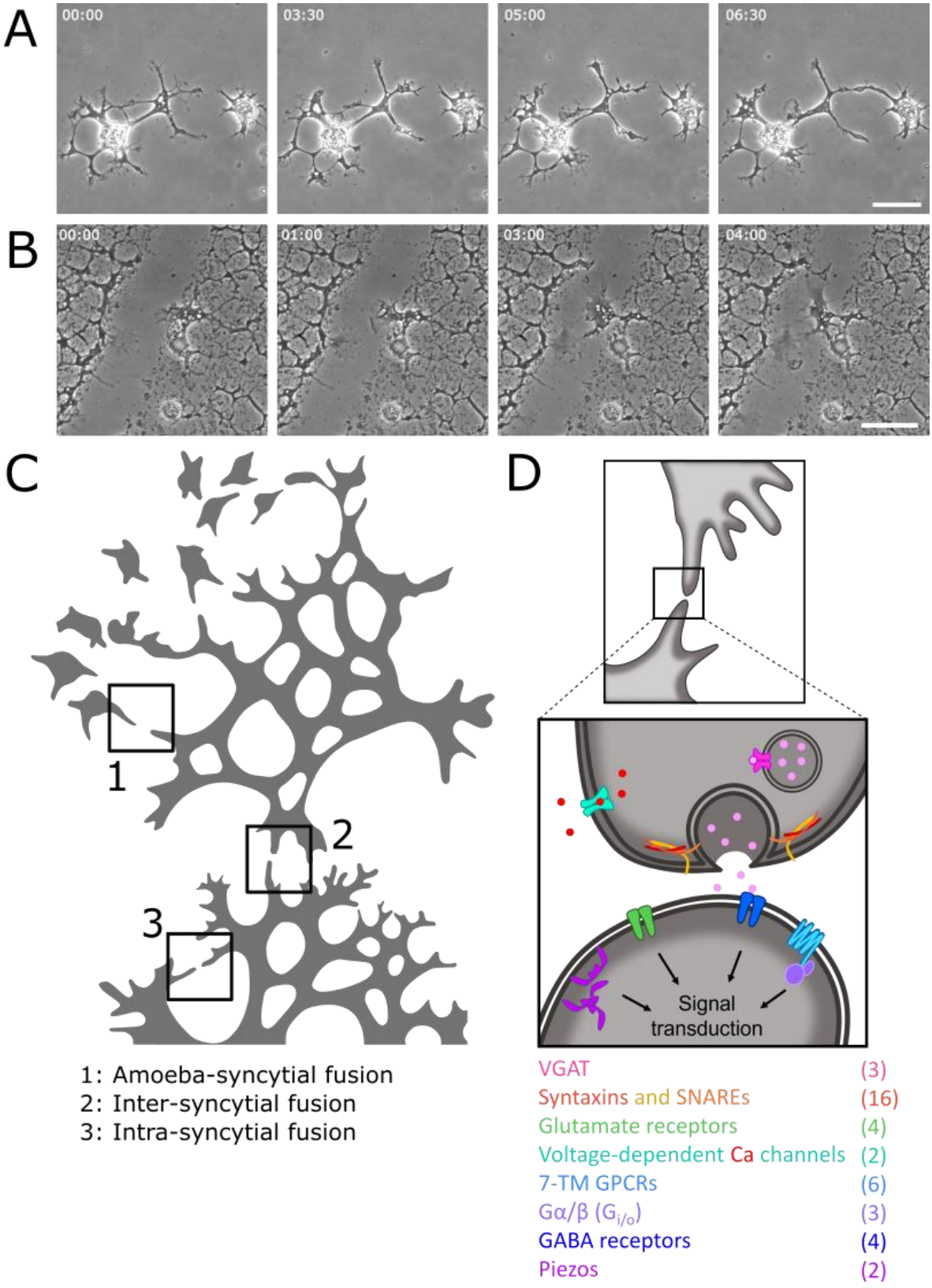

(A) *Filoreta* syncytia growing together and fusing to a smaller syncytium. Scale = 50µm.

(B) Confluent *Filoreta* syncytium shown post-mechanical disruption by scraping culture surface. Within 4 minutes, the syncytium grows back together and re-fuses to itself. Scale = 50 µm.

(C) Schematic representation of life cycle stages in which fusion events occur: (1) Amoeba are recruited towards and fuse to syncytia, (2) Syncytia fuse to neighboring syncytia, (3) syncytia self-fuse to form the looped network during development.

(D) Representation of genes identified in the *Filoreta* genome that are required for self-recognition, signal transduction and membrane fusions in other signaling cell types.

Figure 2.12: Self recognition in *Filoreta* is strain-specific

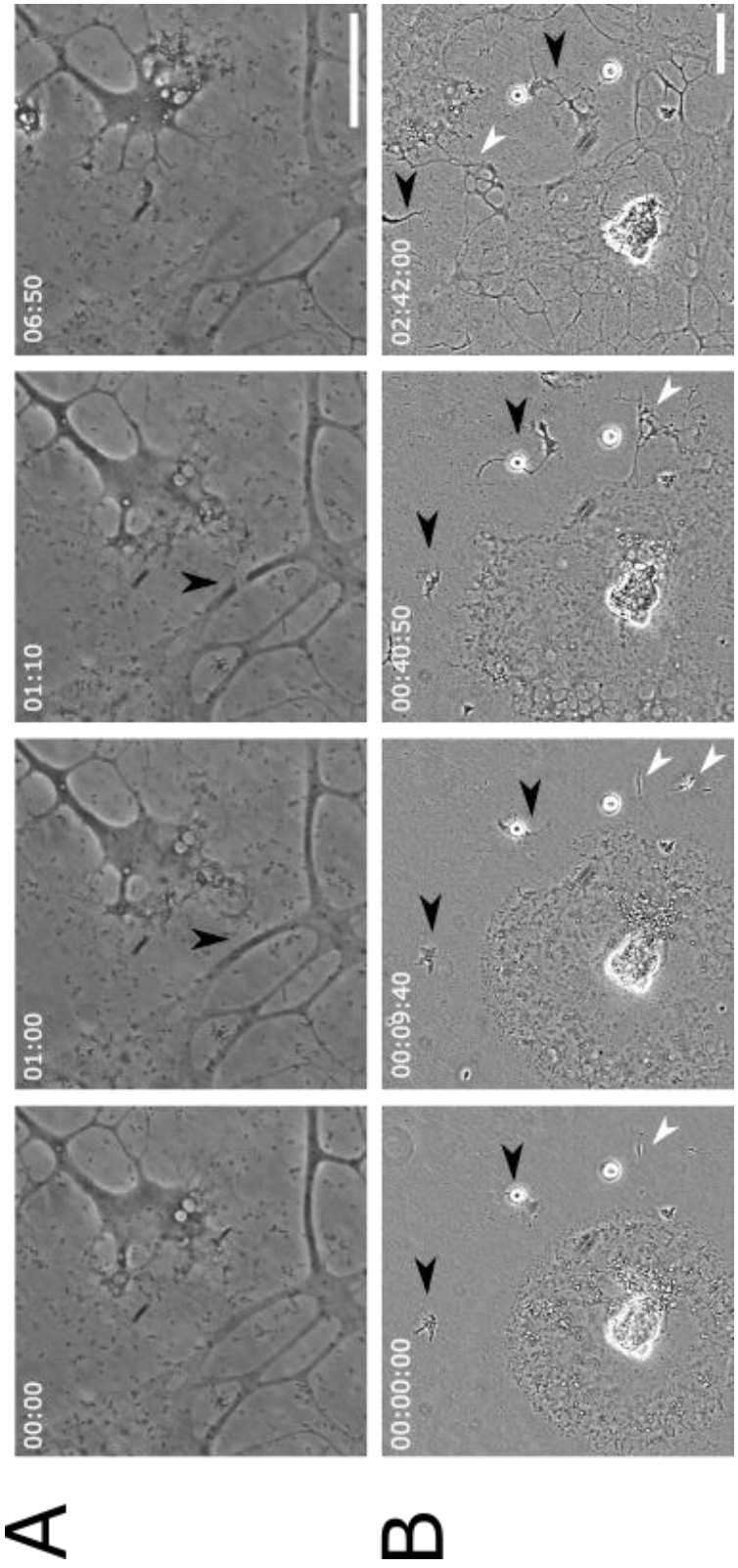

(A) *Filoreta* strains from different locations (SW4B = Sippewissett Marsh, MA and BBFil = Bodega Bay, CA) are co-incubated and disrupt each other's network structure. Strain SW4B (bottom left) breaks its branch (arrow, 1:00 minute to 1:10), to avoid interaction with BBFil (top right). Within minutes, BBFil then turns its lamellipodial edge to grow in a different direction (6:50). Scale = 50 µm.

(B) Strain SW4B grows radially but breaks symmetry in two ways: to avoid BBFil syncytial fragments (black arrows) and grow faster in the direction of clonal SW4B Syncytia (white arrows). After 2:42 hours, two large SW4B syncytia have fused but maintain a large avoidance ring around BBFil. Scale = 100 µm.

Table 2.1: Actin related proteins

Protein	Homolog	Copy#	id	IPR#
Actin	Actin 1	5	g1038.t1 g9908.t1 g9985.t1 g795.t1 g8494.t1	IPR004000
	Novel Arp1	2	g5720.t1 g5691.t1	IPR004000
	Novel Arp2	4	g10669.t1 g10558.t1 g5904.t1 g11165.t1	IPR004000
	Novel Arp3	2	g8608.t1 g8608.t2	IPR004000
	Novel Arp4	2	g3752.t1 g3151.t1	IPR004000
	Novel Arp5	2	g1362.t1 g11046.t1	IPR004000
ARP	Arp1	1	g10871.t1	IPR004000
	Arp2	1	g1455.t1	IPR004000
	Arp3	1	g7983.t1	IPR004000
	ArpC1	1	g4253.t1	IPR004000
	ArpC2	1	g6206.t1	IPR007188
	ArpC3	1	g428.t1	IPR007204
	ArpC4	1	g1759.t1	IPR008384
	ArpC5	1	g7856.t1	IPR006789
WASP	WASL	2	g9115.t1 g1322.t1	IPR003124
Formin	Formin	7	g7470.t2 g9752.t1 g4456.t1 g16.t1 g5040.t1 g281.t1 g6181.t1	PF06367 PF06017

Protein	Homolog	Copy#	id	IPR#
Cofilin	Cofilin	10	g10256.t1 g1097.t1 g1191.t1 g1611.t1 g2128.t1 g6530.t1 g7192.t1 g803.t1 g838.t1 g8513.t1	PF00241
Myosin	myosin I	8	g1217.t1 g2492.t1 g5259.t1 g6642.t1 g7826.t1 g8661.t1 g10388.t1	IPR001609
	myosin II-like	2	g1615.t1 g7892.t1	IPR001609
	myosin IV	4	g7892.t1 g11257.t1 g6102.t1 g10831.t1	IPR001609
	myosin orphan	4	g4130.t1 g10848.t1 g7655.t1 g6252.t1	
	myosin VII-like	1	g4768.t1	
Gelsolin	Gelsolin	3	g3971.t1 g6155.t1 g6155.t2	PF00626
Advillin	Advillin	1	g6150.t1	
Filamin	Filamin	4	g1758.t1 g2807.t1 g6208.t1 g6758.t1	
WASH Complex	WASH complex subunit 7	2	g6183.t1 g6183.t2	IPR028282
	strumpellin	1	g6036.t1	IPR019393
	CCDC53	2	g5498.t1 g3372.t1	IPR019309

Table 2.2: Tubulins and MAPs

Protein	Homolog	Copy#	id	IPR #
Tubulin	Alpha-tubulin	6	g668.t1 g10883.t1 g3703.t1 g9551.t1 g1300.t1 g522.t1	IPR003008
	Beta-tubulin	5	g3290.t1 g8309.t1 g5693.t1 g8271.t1 g9273.t1	IPR003008
	Gamma-tubulin	1	g8987.t1	IPR003008
Gamma-TURC	GCP2	1	g1583.t1	IPR041470
	GCP3	1	g6156.t1	IPR041470
	GCP4	2	g1291.t1 g1291.t2	IPR041470
	GCP5	1	g10914.t1	IPR041470
	GCP6	1	g3711.t1	IPR041470
	SAS6	1	g5227.t1	IPR032396
Capping/Severing	CLASP1/2	2	g5934.t1 g5934.t2	
	CLIP1	1	g6512.t1	
	Katanin p60	1	g4717.t1	
	Katanin p80	1	g10626.t1	
	Fidgetin	1	g5528.t1	
	Spastin	1	g5067.t1	
XMAP215	XMAP215	1	g8714.t1	
End-binding (EB)	EB1	2	g7175.t1 g7233.t1	
MAPs	WAFL	1	g7072.t1	
	PRC1	1	g6610.t1	
	MEMO1	1	g9300.t1	
	KIFBP	1	g4464.t1	
Kinesin	Kinesin	19	g10007.t1 g10570.t1 g1391.t1 g1391.t2 g1702.t1 g2383.t1 g2949.t1 g354.t1 g403.t1 g4075.t1 g4695.t1 g6249.t1 g6707.t1 g6947.t1 g7882.t1 g7949.t1 g8701.t1 g8752.t1 g880.t1	IPR001752
Dynein	Axonemal	13	g1562.t1 g4778.t1 g936.t1 g936.t2 g936.t3 g8132.t1 g9588.t1 g9597.t1 g7592.t1 g7592.t2 g5657.t1 g5657.t2 g6316.t1	IPR013594
	Cytoplasmic	2	g3376.t1 g6316.t1	IPR013594 IPR035699
Dynactin	Dynactin 1	1	g7184.t1	IPR000938
	Dynactin 4	1	g1032.t1	IPR008603
	Dynactin 5	1	g10.t1	
	Subunit p22	2	g11188.t1 g3348.t1	IPR009991
	LIS-1/NudF	1	G10626.t1	IPR006594
Tubulin-modifying enzymes	Tubulin-tyrosine ligase family protein	5	g9953.t1 g9953.t2 g2421.t1 g9953.t2 g8477.t1	IPR004344
Tubulin cofactors	tubulin-specific chaperone A	1	g9064.t1	IPR004226
	tubulin-specific chaperone B	1	g4125.t1	IPR000938
	tubulin-specific chaperone C	1	g5799.t1	IPR012945
	tubulin-specific chaperone D	1	g7959.t1	IPR022577
	tubulin-specific chaperone E	1	g9845.t1	IPR000938
	tubulin binding cofactor C	2	g182.t1 g2250.t1	IPR012945

Table 2.3: Centriole proteins

Protein	Homolog	Copy#	id	IPR #
BBSome	B9-type C2 domain	3	g5873.t1 g381.t1 g881.t1	IPR010796
	TTC8, BBS8; tetratricopeptide repeat protein 8	2	g2444.t1 g2444.t2	
	ARL6, BBS3; ADP-ribosylation factor-like protein 6	1	g8413.t1	
	BBS1; Bardet-Biedl syndrome 1 protein	1	g8145.t1	
	BBS2; Bardet-Biedl syndrome 2 protein	1	g9893.t1	
	BBS4; Bardet-Biedl syndrome 4 protein	2	g4748.t1 g4748.t2	
	BBS5; Bardet-Biedl syndrome 5 protein	1	g4472.t1	
	BBS7; Bardet-Biedl syndrome 7 protein	1	g10199.t1	
	CCT1, TCP1; T-complex protein 1 subunit alpha	1	g2273.t1	
	CCT2; T-complex protein 1 subunit beta	1	g3910.t1	
	CCT3, TRIC5; T-complex protein 1 subunit gamma	1	g2237.t1	
	CCT4; T-complex protein 1 subunit delta	1	g7055.t1	
	CCT5; T-complex protein 1 subunit epsilon	1	g1536.t1	
	CCT8; T-complex protein 1 subunit theta	1	g5390.t1	
MKS complex	MKS1; Meckel syndrome type 1 protein	1	g5266.t1	IPR010796
	TMEM17; transmembrane protein 17	1	g3108.t1	
	TMEM67, MKS3; meckelin	1	g5686.t1	
	TMEM107; transmembrane protein 107	1	g7103.t1	
	TMEM216; transmembrane protein 216	1	g4723.t1	
	TMEM231; transmembrane protein 231	1	g8142.t1	
Centriole Proteins	K16458 CEP104; centrosomal protein CEP104	1	g8203.t1	
	K16459 CEP120; centrosomal protein CEP120	1	g7114.t1	
	K16465 CETN1; centrin-1	2	g1471.t1 g3693.t1	
	K16466 CETN3, CDC31; centrin-3	2	g7227.t1 g7531.t1	
	K16482 POC1; centriolar protein POC1	1	g6142.t1	
	K16483 POC5; centrosomal protein POC5	1	g2643.t1	
	K16487 SAS-6, SASS6; spindle assembly abnormal protein 6	1	g5227.t1	IPR032396
Pericentriole	K16533 CEP290, NPHP6; centrosomal protein CEP290	1	g3610.t1	
	K06085 SSX2IP, ADIP; synovial sarcoma, X breakpoint 2 interacting protein	1	g11080.t1	
	K16540 AZI1, CEP131; 5-azacytidine-induced protein 1	1	g3050.t1	
Other	K16770 CNTRL; centriolin	1	g1381.t1	
	K07943 ARL2; ADP-ribosylation factor-like protein 2	1	g4919.t1	
	K16750 BLOC1S2; biogenesis of lysosome-related organelles complex 1 subunit 2	1	g1248.t1	
	K16755 CCDC61; coiled-coil domain-containing protein 61	1	g8959.t1	
	K23693 CCDC78; coiled-coil domain-containing protein 78	1	g2383.t1	
	K04393 CDC42; cell division control protein 42	1	g5534.t1	
	K07195 EXOC7, EXO70; exocyst complex component 7	1	g9632.t1	
	K07901 RAB8A, MEL; Ras-related protein Rab8A	1	g3849.t1	
	K16780 SSNA1; sjoegren syndrome nuclear autoantigen 1	1	g4930.t1	
	K25164 WRAP73, WDR8; WD repeat-containing protein WRAP73	1	g5587.t1	
	K09142 SPOUT1; methyltransferase [EC:2.1.1.-]	1	g9958.t1	

Table 2.4: Flagellar/Ciliary proteins

Protein	Homolog	Copy#	id
Intraflagellar Transport Complex A	WDR19, IFT144; WD repeat-containing protein 19	1	g2574.t1
	WDR19, IFT144; WD repeat-containing protein 19	1	g4795.t1
	IFT140; intraflagellar transport protein 140	1	g8927.t1
	IFT140; intraflagellar transport protein 140	1	g8974.t1
	IFT139B; tetratricopeptide repeat protein 21B	1	g7267.t1
	IFT122; intraflagellar transport protein 122	1	g1688.t1
	IFT121; WD repeat-containing protein 35	1	g8171.t1
	IFT88; intraflagellar transport protein 88	1	g5324.t1
	DYF1; tetratricopeptide repeat protein 30	1	g2654.t1
Intraflagellar Transport Complex B1	IFT52; intraflagellar transport protein 52	1	g7551.t1
	IFT46; intraflagellar transport protein 46	1	g4478.t1
	IFT22, RABL5; intraflagellar transport protein 22	1	g10262.t1
	IFT172; intraflagellar transport protein 172	1	g2972.t1
	IFT80; intraflagellar transport protein 80	1	g9733.t1
	IFT57, HIPPI, ESRRBL1; intraflagellar transport protein 57	1	g748.t1
	IFT54; TRAF3-interacting protein 1	1	g10249.t1
Intraflagellar Transport Complex B2	IFT20; intraflagellar transport complex B, subunit 20	1	g2663.t1
	FLA10, Kinesin-II Motor Protein	1	g7347.t1
	FLA8 Kinesin II Motor Protein	2	g1391.t1 g1391.t2
	KAP, Kinesin II associated Protein	2	g9790.t1 g9790.t2
	DHC1b, Cytoplasmic Dynein Heavy Chain 1b	1	g6316.t1
	D1bLIC, Dynein 1b Light Intermediate Chain	1	g3217.t1
Central Pair	PF16/Spag6, Central PairProtein		g6268.t1
	PF20/Spag16, Central Pair Associated WDRepeat Protein	1	g825.t1
	PF6/SPAG17, Central PairProtein	1	g8030.t1
	Hydin	1	g5145.t2
Dynactins	K04648 DCTN1; dynactin 1	1	g7184.t1
	K10426 DCTN4; dynactin 4	1	g1032.t1
	K10427 DCTN5; dynactin 5	1	g10.t1
	Dynactin subunit p22	2	g11188.t1 g3348.t1
	RUVBL2, RVB2, INO80J; RuvB-like protein 2	1	g10852.t1
	CFAP298; cilia- and flagella-associated protein 298	1	g2453.t1
Modifier of Inner Arms (MIA) Complex	CFAP100, MIA1; cilia- and flagella-associated protein 100	1	g4255.t1
	CFAP73, CCDC42; CFAP73 family protein	1	g3577.t1
	CFAP73, CCDC42; CFAP73 family protein	1	g4881.t1
Radial Spoke	RSPH1; radial spoke head protein 1	7	g6256.t1 g6886.t1 g6886.t2 g6888.t1 g6900.t1 g6903.t1 g6904.t1
	RSPH3; radial spoke head protein 3	2	g10501.t1 g10501.t2
	RSPH4_6; radial spoke head protein 4/6	1	g9493.t1
	RSPH10B; radial spoke head protein 10B	1	g5298.t1
Calmodulin-spoke complex	DNAJB13; DnaJ homolog subfamily B member 13	1	g10534.t1
	CFAP61; cilia- and flagella-associated protein 61	1	g1829.t1
	CFAP91, MAATS1; cilia- and flagella-associated protein 91	1	g8646.t1
	WDR66, CFAP251; cilia- and flagella-associated protein 251	1	g2632.t1
Tether/Tether Head Complex	CFAP44, WDR52; cilia- and flagella-associated protein 44	2	g7979.t1 g7979.t2
ODA Docking Complex	CCDC63_114; coiled-coil domain-containing protein 63/114	1	g10488.t1
96 nano-molecular ruler	CCDC39; coiled-coil domain-containing protein 39		g1606.t1
	CCDC40; coiled-coil domain-containing protein 40		g4479.t1
Other Cilia-Associated Proteins	CEP162; centrosomal protein CEP162	2	g6294.t1 g6294.t2
	CFAP20; cilia- and flagella-associated protein 20	2	g3993.t1 g4322.t1
	CFAP52, WDR16; cilia- and flagella-associated protein 52	1	g7313.t1
	CFAP57, WDR65; cilia- and flagella-associated protein 57	3	g582.t1 g9669.t1 g9692.t1
	BBOF1; basal bodyorientation factor 1	1	g11012.t1
	EFHC1; EF-hand domaincontaining protein 1	1	g9046.t1

Table 2.5: Nuclear structure

Protein		Homolog	Copy#	id	IPR #
Nuclear Pore Complex	Cytoplasmic filaments	NUP358	1	g154.t1	
		GLE1	1	g5466.t1	
		DDX19	1	g9741.t1	
		Rae1	1	g8372.t1	
	Transmembrane Ring	POM33	1	g6251.t1	
		Gp210	1	g9739.t1	
	Outer Ring	Sec13	1	g761.t1	
		NUP96	2	g3385.t1 g4519.t1	
		NUP107	1	g1761.t1	
		NUP85	1	g9003.t1	
	Inner Ring	NUP205	1	g5208.t1	
		NUP155	1	g1274.t1	
	Central Channel	NUP98	2	g3385.t1 g4519.t1	
		NUP62	3	g7511.t1 g7511.t2 g7944.t1	
	Nuclear Basket	NUP88	1	g7447.t1	
		NUP93	1	g4992.t1	
		NUP153	1	g7840.t1	
THO complex		THOC1; THO complex subunit 1	1	g4609.t1	
		THOC2; THO complex subunit 2	1	g2087.t1	
		THOC3; THO complex subunit 3	1	g10110.t1	
LINC Complex		**K19347 SUN1_2; SUN domain-containing protein 1/2**	**6**	**g2595.t1 g10312.t1 g10312.t2 g7450.t1 g8074.t1 g4371.t1**	
		K21875 SPAG4, SUN4; sperm-associated antigen 4 protein	**1**	**g7450.t1**	
		K22595 CCDC155, KASH5; protein KASH5	**1**	**g7335.t1**	
Lamins		**Lamin-B2**	**1**	**g7435.t1**	

Table 2.6: Mitosis and Cell cycle

Protein	Homolog	Copy#	id	IPR #
Spindle Formation Proteins	CKAP5; cytoskeleton-associated protein 5	1	g8714.t1	
	CSE1, CAS, XPO2; exportin-2 (importin alpha re-exporter)	1	g4404.t1	
	KIF2_24, MCAK; kinesin family member 2/24	1	g7678.t1	
	KIF11, EG5; kinesin family member 11	1	g8527.t1	
	KPNA5_6; importin subunit alpha6/7	3	g1392.t1 g5008.t1 g8069.t1	
	KPNB1, IPO1; importin subunit beta1	2	g6752.t1 g6783.t1	
	NUP43; nuclear pore complex protein Nup43	1	g508.t1	
	NUP85; nuclear pore complex protein Nup85	1	g9003.t1	
	NUP98, ADAR2, NUP116; nuclear pore complex protein Nup98Nup96	2	g3385.t1 g4519.t1	
	NUP107, NUP84; nuclear pore complex protein Nup107	1	g1761.t1	
	NUP205, NUP192; nuclear pore complex protein Nup205	1	g5208.t1	
	TMEM33; transmembrane protein 33	1	g6251.t1	
	PAFAH1B1, LIS1; platelet-activating factor acetylhydrolaseIB subunit alpha	1	g10626.t1	
	RAE1, GLE2; mRNA export factor	1	g8372.t1	
	RAN; GTP-binding nuclear protein Ran	2	g311.t1 g6090.t1	
	TCHP; trichoplein keratin filament-binding protein	2	g973.t1 g1003.t1	
	TPX2; targeting protein for Xklp2	1	g5157.t1	
	NEK6; serine/threonine-protein kinase Nek6	1	g4806.t1	
	NEK9, NERCC1; serine/threonineprotein kinase Nek9	3	g4285.t1 g6702.t1 g7636.t1	
Aurora Kinase And Regulators	AURKA; aurora kinase A	1	g10330.t1	
	AJUBA, LIMD1, WTIP; LIM domain-containing protein	1	g3944.t1	
	PPP1R2, IPP2; protein phosphatase inhibitor 2	1	g8147.t1	
	TPX2; targeting protein for Xklp2	1	g5157.t1	
Sister Chromatid Separation	ESP1; separase	1	g3856.t1	
APC/C Complex	APC2, ANAPC2; anaphase-promoting complex subunit 2	1	g7664.t1	
	APC3, CDC27; anaphase-promoting complex subunit 3	1	g109.t1	
	APC4, ANAPC4; anaphase-promoting complex subunit 4	1	g10865.t1	
	APC5, ANAPC5; anaphase-promoting complex subunit 5	1	g9015.t1	
	APC6, CDC16; anaphase-promoting complex subunit 6	1	g10134.t1	
	APC7, ANAPC7; anaphase-promoting complex subunit 7	1	g9126.t1	
	APC8, CDC23; anaphase-promoting complex subunit 8	1	g8358.t1	
	APC10, ANAPC10, DOC1; anaphase-promoting complex subunit 10	2	g2414.t1 g2414.t2	
	CDC20; cell division cycle 20, cofactor of APC complex	1	g5811.t1	
Cyclins	CCNA; cyclin-A		g6823.t1 g8300.t1	
	CCNB; G2/mitotic-specific cyclin-B, other		g3263.t1 g4030.t1	
	CCNE; G1/S-specific cyclin-E1		g5840.t1	

Table 2.7: Cell Signaling

Protein	Homolog	Copy#	Id	IPR #
Neuron-Like Signaling	GABBR, gamma-aminobutyric acid (GABA) type B receptor	4	g4660.t1 g6307.t1 g7385.t1 g7385.t2	
	GRM4, metabotropic glutamate receptor 4	1	g2080.t1	
	GNAO, guanine nucleotidebinding protein G(o) subunit alpha	1	g137.t1	
	VGAT, Vesicular_inhibitory_amino_acid_transporter	3	g8225.t1 g8343.t1 g3369.t1	
	VMAT, chromaffin_granule_amine_transporter	1	g5290.t1	
	Ionotropic Glutamate receptor	3	g5733.t1 g391.t1 g5725.t1	
	voltage-dependent calcium channel	1	g10734.t1	
	SV2, synaptic vesicle glycoprotein 2	1 (3)	g2531.t1	
	DAGL, sn1-specific diacylglycerol lipase	4	g708.t1 g708.t2 g1848.t1 g1848.t2	
	FAAH, fatty acid amide hydrolase	2	g510.t1 g510.t2	
Membrane fusion Proteins	STXBP1, syntaxin-binding protein 1	1	g10817.t1	
	STX1A, syntaxin1 type	1	g4920.t1	
	Syntaxin7/12	3	g1614.t1 g9486.t1 g7535.t1	
	Syntaxin16	8	g11377.t1 g11263.t1 g10812.t1 g11377.t2 g11263.t2 g10812.t2 g11241.t1 g11103.t1	
	VAMP2 (syntaxininteractor)	1	g7955.t1	
	Synaptobrevin	1	g1194.t1	
	Synapsin	1	g3893.t1	
	Synaptotagmin(Copine-like?)	1	g2580.t1	
Rab3 interacting molecules (RIMS)	Dysferlin-like (calcium-dependent membrane repair)	2	g3192.t2 g7593.t1	
	RIMS	2	g2497.t1 g7697.t1	
	Rab3 GTPase	1	g1707.t1	
	NSF, vesicle-fusing ATPase	1	g3056.t1	
	MYCBP2, RCR-type E3 ubiquitin transferase (axon regeneration)	1	g431.t1	
Photoreception Pathways	GRK1_7, rhodopsin kinase	1	g2350.t1	
	all-trans-retinol 13,14-reductase	1	g1477.t1	
	RDH, retinol dehydrogenase 11	7	g1905.t1 g2958.t1 g4300.t1 g4329.t1 g5490.t1 g8787.t1 g9056.t1	

Chapter 3

The Rhizarian amoeba *Filoreta* develops an arborized network with conserved cytoskeletal mechanisms

Sarah L. Guest and Scott C. Dawson

Department of Microbiology and Molecular Genetics

One Shields Avenue

UC Davis, Davis, CA 95616

Abstract

Filoreta ramosa is a Rhizarian marine amoeba whose life cycle involves a multinucleate stage, during which the highly arborized syncytium undergoes extensive branching and fusion (anastomosis) events to grow, ultimately expanding multiple centimeters across a surface. How does an amoeba maintain its organization and enable transport, karyoplasmic ratio and distribution of organelles at this size?

This study investigates the basis of *Filoreta's* branched network structure, focusing on its distinctive microtubule and actin-based morphology, long-ranged and bidirectional transport mechanisms, and its unique microtubule nucleation machinery independent of conventional microtubule organizing centers (MTOCs). *Filoreta's* complex and dynamic cell morphology, characterized by variable pseudopodia and intricate branching, showcases its remarkable adaptability and response to its environment. Its interphase microtubule arrays, a key component of this morphology, facilitate rapid and extensive organelle transport, a phenomenon critical for its survival and development. Remarkably, the mechanism of cytoskeletal organization closely mirrors that of neuronal arborization. Through live imaging techniques, immunofluorescence, and cytoskeletal drug perturbations, we show that evolutionarily conserved proteins are key to the morphogenesis of the complex network of this unusual syncytial amoeba. We emphasize that this overlapping phenotype is likely an ancient mechanism toward spatiotemporal organization across long distances, and enables rapid and efficient responses to environmental cues. These findings shed light on the neuron-like strategies that enable *Filoreta* to grow in a fluctuating intertidal environment, and enable its rapid growth, transport, and wound-healing. Through these comparisons, the data presented here provides fresh insights to the evolution of arborized morphology as a strategy for spatiotemporal regulation across the eukaryotic tree.

Introduction

Eukaryotic cells are composed of both actin and tubulin cytoskeletons, and understanding the structure and function of the cytoskeleton in diverse lineages is fundamental to our understanding of the evolution of eukaryotes. Nearly every eukaryotic lineage has an amoeboid morphotype, and amoeboid morphology is incredibly varied, yet uses evolutionarily conserved cytoskeletal components and dynamics (Tekle and Williams, 2016). The genetics and evolution of amoeboid movement and its associated morphologies requires knowledge from diverse amoeboid lineages. Much like the same baking ingredients used in numerous recipes can be combined in different ways make a wide variety of desserts, the eukaryotic cytoskeleton and interacting proteins can be used in a combinatorial manner to generate an immense diversity of morphologies and structural characteristics. Amoeboid cells exhibit pseudopodial projections that are described as: flat and ruffled (lamellipodia), thin and filose (filopodia), blunt and lobed (lobopodia), radial and needle-like (axopodia), eruptive blebs, and branching and anastomosed/reticulated (reticulopodia) (Fritz-Laylin et al. 2018, 20; Berney et al. 2015). These different "flavors" of pseudopodia are found across the major eukaryotic clades, but are also source of diversity within lineages. How do amoebae throughout the eukaryotic tree use the conserved cytoskeletal proteins and mechanisms to generate these diverse and variable morphologies?

Of the amoeboid morphotypes, there is a striking resemblance between the branched reticulopodia observed in Rhizaria and Amoebozoa (Berney et al., 2015), and complex arborizations in metazoan neurons (Black, 1981). In 1890, Duval and Lépine suggested the activity of neurons could be understood via analogy with amoeboid rhizopods (branched pseudopodia) (Reynolds, 2008), drawing a clear parallel between branched amoebae and neural

arbors. While most metazoan neurons have been definitively described as individual cells that are strictly arborized, self-fusion and fasciculation events in axons lead to a looped topology during development akin to reticulopodia (Šmít et al., 2017). Further, the neural networks of ctenophores form a looped contiguous network, matching the historically deemed "incorrect" Reticular (Syncytial) Theory by Camillo Golgi (Burkhardt et al., 2023). Golgi's Reticular theory actually still holds true in many aspects*:* neurons that are connected via gap junctions effectively have a continuous cytoplasm and are transiently syncytial, allowing instantaneous signal transduction and topology changes in connectivity to neighboring neurons (Hameroff, 2010).

While underlying cytoskeletal mechanisms driving the development of network morphology have been well defined in neurons, the evolutionary history of arborized and anastomosing cell types and underlying cytoskeletal mechanisms of other lineages is unresolved. Transport of organelles and cytoskeletal components in neurites is crucial for cell development and function at processes and necessitates investigations into understanding appropriate distribution and localization for neuronal function (Koppers and Farías, 2021; Venkatesh et al., 2020). Efforts to define the dynamics and organization of the eukaryotic cytoskeleton have largely employed the use of model organisms, most of which are not free-living protists from diverse clades, but from metazoan, fungal and plant lineages, or parasites (Burki and Keeling, 2014; Matthews and Vosshall, 2020).

Are the underlying mechanisms governing cytoskeletal arborization ancient or have they evolved independently in multiple lineages? Determining how arborized and anastomosing cell types have either conserved or convergent mechanisms requires a better understanding of the evolution of cytoskeletal-based morphogenesis, complexity, multicellularity, and cell-signaling systems across eukaryotic evolutionary history.

Branched pseudopodial networks exist in at least three of the major eukaryotic lineages: Amoebozoa, Rhizaria, and Opsithokonts, specifically in the neuronal cell types of Metazoa. Many Rhizarian amoebae have extensive networks of "reticulopodia", a branched and looped network of pseudopodial extensions (Berney et al., 2015). Through this network they exhibit dynamic morphology that enables efficient interactions with their environments over large areas. The Rhizaria are often distinguished by their branched and anastomosing reticulopodial networks, a characteristic conserved across the amoeboid members of this supergroup (Berney et al., 2013; Burki and Keeling, 2014). However, aside from early efforts in the Foraminifer relative *Reticulomyxa*, the Rhizarian cytoskeleton and morphological development remain largely understudied (Burki and Keeling, 2014; Glöckner et al., 2014; Koonce et al., 1987; Orokos et al., 2000; Orokos and Travis, 1997; Schliwa et al., 1991).

Here, we define actin and MT mechanisms driving branching and anastomosing network morphology in the clonally propagated Rhizarian amoeba, *Filoreta ramosa*. We show that *Filoreta* has a dynamic reticulated morphology that coordinates actin-based and MT-based cytoskeletal machinery in a manner similar to other arborized cell types, specifically neurons. Multinucleate syncytia have an interphase MT array that organizes longitudinally in branches throughout the network, providing structure, stability, long-ranged organelle transport, and enabling branch elaboration much like the MT arrays in axons and dendrites (Baas et al., 2016). Further, the actin cytoskeleton provides dynamic, polymerization-dependent psuedopodial extensions as lamellipodia, filopodia and reticulopodia. Thus, the cytoskeletal architecture and arborized MT development of Rhizarian amoebae like *Filoreta* cytoskeletal architecture are not only physically reminiscent of metazoan cell types like neurons, but they also seem to follow similar mechanisms and interactions between the actin and MT cytoskeletons. This implies such

mechanisms are ancient and evolved over a billion years ago before the divergence of these clades. More diverse models are crucial to clarify the evolution of complex branched cytoskeletal networks.

Results

Dynamic, reticulated branched networks define the development of the *Filoreta* syncytium

In initial observations of *Filoreta* in culture, we observed an extensive reticulated network of dynamic branches and loops that alter morphology in response to environmental cues or stimuli (Chapter 2). To define the precise nature of the branching development of this expansive arborized syncytium, we performed time lapse imaging that captured key events and cellular behaviors in *Filoreta*'s branched syncytial development throughout the life cycle (Figure 3.1).

In a growing syncytium, numerous peripheral pseudopodia (3.1A) extend as transient "branchlets" (3.1G) that extend outward and form loops by fusing together in a process termed "anastomosis" (3.1B). Pseudopodial branchlets often collapsed and folded in on themselves as filopodia and lamellipodia. Branchlets that intersected with "nodes" often were thicker, stabilized "branches" as the syncytium grew outwards (3.1C). Stable branches did not retract or fold back in on themselves and remained as part of the network topology as the syncytium continued to grow outward. Serial repetition of this branching, extension, and fusion process yielded a reticulate morphology that increased in branch degree (complexity) as the syncytium developed. Higher resolution of pseudopodial activity at one of these branchlets, for example indicated the dynamic ability of pseudopodia to extend as wide, flat, and often ruffled lamellipodia (3.1A-center) or branched filopodia (1A-right). Reticulopodial anastomoses

developed throughout the network, in both transient pseudopodial branchlets and in stabilized branches.

The syncytium grew outward and maintained the looped network structure across the entire surface area provided. When presented with 0.02% yeast extract and tryptone (YET), a two-fold increase in nutrient concentration, the network responded by altering its topology and new branchlets initiated via lateral pseudopod extensions (3.1C, 3.1I). Newly initiated branchlets often thickened and became part of the interior network topology (3.1I).

"Pruning" is a phenomenon of branch simplification and loss described as a part of the aging process in dendritic arbors (Kirch and Gollo, 2021). In *Filoreta*, we also use the term "pruning" to describe the decrease in arborization density (ref for pruning neuron term). Under starvation or stress conditions, the network responded by "pruning", a process that simplifies branch topology by removal and simplification of branches via retraction (3.1D).

When grown in cultures with five times the nutrient availability (0.05% YET), individual amoebae (3.1H) were present and readily fused to the network. Neighboring syncytia also fused together to form a larger syncytium (3.1E), after which reorganization of the shared cytoskeletal components and organelles was possible. Organelles moved bidirectionally in branches throughout the network, and caused the membrane to bulge as they traversed narrow branches (3.1H). Anastomosed filopodia within the same syncytia or between neighboring syncytia transitioned from "branchlets" to "branches" by a distinctive thickening of the adjoined filopodia (3.1I).

Individual amoebae (3.1J) occurred in cultures with dense nutrient availability (Methods) or were found immediately following transfer from plate culture (see Chapter 1 methods of

cultivation). Typically, individual amoebae were transient and were approximately 10 µm in diameter. Individual amoebae were migratory via filopodia (3.1J, left panel) and lamellipodia (3.1J, right panel). When in close proximity to each other, or to a nearby syncytium, their filopodial extensions elongated until they contacted the neighboring cell, upon which they rapidly fused (3.1F) and were incorporated into the network.

Syncytia have distinct cytoskeletal architectures in both pseudopodia and in branches.

To determine the underlying cytoskeletal architecture driving the dynamic morphology in *Filoreta*, we fixed and immunostained the actin and MT (MT) arrays in syncytia at different stages of development. Actin staining revealed dense F-actin filaments and patches in filopodial (3.2A, 3.2B), in lamellipodial projections (3.2H) of peripheral branchlets, and along branches (2C, 2J). Such pseudopodial projections were particularly actin-enriched in branch-fusion sites with anastomosed filopodia (reticulopodia) (3.2A), and lamellipodia (3.3A), and at the growing edge of a syncytial periphery (3.2B). Branches comprising the interior loops of the network contained longitudinal MTs (3.2C, 3.3B). At the transition area between branches and branchlets (reticulopodia), longitudinally oriented MTs were partially incorporated into a fraction of branchlets (3.2B, 3.3B).

The major branch “hubs” (3.2D) that become sites of macrocyst formation contain MT ends and are often highlighted by actin-based structures similar to lamellipodia observed at the hub boundaries (3.2D). Branches leading to hubs were 2-3X thicker on average than peripheral branches proximal to branchlets.

The distinction between “branchlets” and “branches” is defined using live imaging to determine whether the reticulopodia remained part of the developing arbor or collapsed in on itself

(transient). We hypothesized that the branchlets that become proliferated with MTs become stabilized into “branches” as part of the network development and topology. To quantify morphological characteristics associated with “branchlets” and “branches” we measured the widths and lengths of actin-only filopodia and compared them to the narrow, proximal, MT-rich “branches.” While the widths of actin-only filopodia varied from about 0.3 μm to 0.6 μm, even the narrowest MT-rich branches were 24 percent thicker than branchlets on average (3.2E, 3.2F). Non-stabilized filopodia also were limited to lengths less than 10 μm, while branches that included MTs varied widely (over 10 μm, with major branches reaching distances well over 50 μm) (3.2G). This distinction is supported by our observations captured with time lapse imaging, where filopodial projections that were transient would collapse on themselves or retracted past a certain threshold of growth.

Dynamic syncytial branchlets with actin and MTs.

Syncytia in proximity readily break radial symmetry to fuse to one another. Pseudopodial extensions were actin enriched at regions where neighboring syncytia fused and often included lamellipodia (3.3A).

To define the cytoskeletal organization underlying the dynamic nature of branch topology and formation of new branches, we fixed and stained syncytia within five minutes after adding 0.02% YET-enriched medium (see Methods) to the growing culture. Dense actin patches occurred at new pseudopodial projections that formed laterally off existing branches, which support that actin-based pseudopodia initiate new branches in the syncytial interior (3.3B). To establish that even syncytia undergoing pruning can re-initiate actin-enriched branchlets, we “starved” cultures in unenriched medium, then fed them with enriched medium prior to fixation. In these syncytia,

peripheral branches were simplified and elongated but had numerous filopodial extensions (3.3C).

Next, we examined the MT structure within lamellipodia at the growing periphery. Lamellipodia contained MTs with varying degrees of curvature, measured by curvature radius (R_c) (3.3D) (Assoian et al., 2019). Curved MTs had a (R_c) averaging 1.07 µm (± 0.28) with curve tangents more than 5 µm from the lamellipodial edge. Straightened MTs had an average R_c over 3.0 µm and were less than 5 µm from the edge. Straightened MTs also oriented their ends towards captured bacterial cells (3.3E).

Organelles are rapidly and bidirectionally transported throughout the syncytial network.

Rapid organelle transport is a defining feature of Rhizaria (Orokos et al., 2000; Schliwa et al., 1991). Our Preliminary brightfield live imaging indicated the *Filoreta* syncytium also undergoes rapid organelle transport (3.1I). To investigate this phenomenon, we directly visualized organelle movements by staining established syncytia with Hoecsht 33342 (nuclei), Syto9 (mitochondria), and Lysotracker (lysosomes). We observed that nuclei, mitochondria, and lysosomes are transported rapidly and bidirectionally throughout the branches of the syncytial network, at rates averaging 5.3 µm/sec, 8.3 µm/sec, and 7.3 µm/sec, respectively (3.4A, 3.4B). Organelles traveling within the same branch were not constrained to the same rate or direction (3.4C). Additionally, the transport rate often slowed or stalled as organelles enter nodes, where two or more branches intersect (3.4D).

We thus hypothesized that branch width is directly correlated with the rate of organelle transport within the network. We initially determined that thicker branches occurred closer to the interior of the network, in close proximity to hubs in developmental stages prior to macrocyst

development (3.2C, D). To confirm any association of branch width with the organelle transport rate, we quantified organelle movement rates constrained by branch width, and matched the nuclear transport rates generated from kymographs within a range of branch widths (1.5 μm to 6.5 μm) (3.4F). We determined that the rate of organelle transport loosely correlated with the width of the branchlet ($R^2 = 0.5498$)(3.4H). For uncomplicated branches (i.e., fewer than one node every 10 μm in length), the rate of transport generally increased with branch width. This corresponded to prior observations showing that within the same branches, transport is not a constant rate for all organellar cargoes. The approximated number of MTs in branches does directly correlate with branch width, ($R^2 = 0.8228$), however (3.4G). Overall, these observations support the hypothesis that branches primarily use MTs as a means of organelle transport, and that branch thickness is an important regulatory aspect of organelle trafficking during different stages of development.

Dynamic expansion and pruning of syncytial arborization throughout development.

Overall branch morphology underscores the direct connection between cytoskeletal form and its inherent functioning in transport and development of the network. To quantify the degree of branch arborization in the growing syncytial during the stages of development, we used Sholl Analysis to measure branch distribution and density at distinct timepoints of *Filoreta*'s life cycle. Sholl Analysis has long been used to quantify the complexity of arborization patterns in neuron morphotypes (Sholl, 1953), which defines an arbor's level of branching complexity as the number of intersecting branch points plotted across radial distances from a central node. Sholl analysis reveals the number of branches, branch topology, and overall pattern of arborized cell types, enabling consistent quantification of morphotype complexity.

Using Sholl profiles (Methods), we quantified branch density and peripheral growth rate of the anastomosed network. Under normal growth conditions, syncytial outgrowth averages 2.5 μm/minute (± 0.55 μm), with no significant difference in growth rate between radially symmetrical syncytia (3.5A), and those with broken symmetry (3.5B). To measure changes in arbor topology during normal growth, Sholl profiles were quantified using the area under the curve, or the total surface area taken up by the branch intersections at each timepoint, respective to other timepoints with identical Sholl parameters. With respect to the relative change in branch intersections and the peripheral expansion, we determined that syncytia expand in surface area coverage by roughly 2.4% per minute at peak growth conditions (3.5H).

Pruning occurred at varying rates depending on the severity of the environmental factors affecting a syncytium (3.5C). For the purposes of these experiments, pruning was induced under artificial stress conditions (removal of nutrient medium, and exposure to blinking light during imaging (see Methods). Stressed syncytia retracted quickly, with approximately 1.5% loss of surface area coverage per minute (3.5C, D, F). Syncytia simplified arbors by pruning pseudopodia and branchlets in a manner that first narrowed minor branches and then major branches, until branches retracted to hubs (3.5D).

Cytoskeletal drugs significantly perturb the dynamics and growth in syncytial arbors.

To define the respective roles of the actin and MT cytoskeleton in generating the arborized morphology, we treated growing syncytia with the MT polymerization-interfering drug nocodazole, and the F-actin disrupting drug Latrunculin.

Quantifying syncytial growth and distribution before and after drug treatments required imaging the untreated syncytia first as a control to normalize for potential variations in culture replicates

(3.6A, C). False-colored thresholded overlays were then used to better visualize the impact of cytoskeletal drugs in syncytia captured in each time lapse (3.6A-D, third panel).

In nocodazole treatments used to quantify the role of MT dynamics in syncytial growth, Sholl profiles were generated from time lapse imaging over 10-minute intervals. By comparison to controls we found a significant decrease in peripheral branch growth, and a marked loss of interior branches (3.6B). Some branches retracted to proximal nodes, suggesting MT depolymerization toward the minus ends and/or the loss of stabilization of branches. This pattern also implied the existence of arrays of antiparallel-bundled MTs. Longer term drug treatment (40 minutes) caused truncated branches and loss of long-range syncytial contacts, yet growth was recoverable upon nocodazole washout and media replacement.

Similarly, we queried the actin-dependence of branch initiation and complexity. We performed similar imaging experiments with 10 nM Latrunculin A for 5 minutes to assess the role of F-actin in growth rate and branch topology. Following treatment, peripheral branching ceased and many filopodia and lamellipodia were observed to seize and retract. Branchlet extension was arrested, while interior branch topology retained stability (3.6D). Drug washout resulted in a delayed (5 minute) recovery of pseudopodial dynamics as a result of the reestablishment of the actin network.

Nocodazole significantly alters the MT distribution throughout the network.

Interior stabilized branches had more MT staining than the growing peripheral branchlets (3.2B, C). Thus to compare the MT arrays in branches and the dynamic peripheral branchlets, we determined the relative distribution of MTs in the network.

To directly visualize the impact of nocodazole treatment on growth and dynamics of the MT arrays in the syncytia, we fixed and immunostained nocodazole-treated syncytia and their untreated controls and quantified the relative distribution of MT staining in the branches (3.7A, B) and branchlets at the periphery of the networks (3.7C, D). We quantified this by first creating separate thresholded maps of tubulin and actin staining for each sample, and then compared the branch topology for the tubulin- and actin-stained Sholl profiles to quantify the MT network as a percentage of the actin network (actin cortex at the membrane boundary as a proxy for branch location).

At the periphery, MT-stained branch distribution comprised only 65.55% (+- 5.4%) of the actin staining in branch and filopodial distributions. In contrast, the interior branches had 88.15% (± 4.9%) MT staining, consistent with the hypothesis that branchlets are stabilized by MTs during development. Nocodazole-treated syncytial peripheries and interior branches were significantly reduced in MT staining at 38.76% and 65.36%, respectively (3.7E). Overall, nocodazole-treated samples had more aggregated signal as a result of the MT depolymerization at nodes (3.7B), likely where the MT minus ends are concentrated.

Nuclei and other organelles are transported throughout the syncytial network using MT-dependent motors.

A Rhizarian relative, *Reticulomyxa filosa*, has an extensive repertoire of kinesin and dynein MT-associated motor proteins (Glöckner et al., 2014). Further, a unique Rhizarian dynein has been reported to be capable of bidirectional transport (Schliwa et al., 1991). Organelle transport in *Filoreta* (3.4A-C) showed that nuclei, mitochondria, and lysosomes traveling within the same branch did not always move at the same rate or direction (kymographs, montage panel), which is

not consistent with cytoplasmic streaming as the primary force for long-ranged transport. In contrast, we predicted that motor driven MT-based transport is the primary mechanism, based on the extensive MT arrays present throughout these syncytial branches. To test this idea, we treated syncytia with varying concentrations of nocodazole while tracking nuclei via Hoechst 33342 staining with live imaging (3.8A, E). While nuclei were capable of some bidirectional movements, the nuclear transport within branches decreased in distance traveled by 33%, and maximal rate by 27% for 20 μM nocodazole treatments. Nuclear transport was most diminished at major branch nodes, where nuclei were stalled completely (3.8H).

To determine whether *Filoreta* transports nuclei using a dynein motors, we treated live syncytia with the dynein inhibitor Ciliobrevin A and imaged nuclear movement (3.8F). After treatment at 25 - 100 μM Ciliobrevin A, there was an immediate and significant reduction in both the rate and distance of nuclear movement (3.8B, F). Over 50% of the nuclei moved processively (more than 10 μm) before treatment, and only 6.5% moved processively after addition of 100 μM Ciliobrevin. Of the nuclei still moving, their rates were slowed by approximately 70%. The directionality of the remaining mobile nuclei was not affected, and many nuclei still moved bidirectionally through branches at 25 μM Ciliobrevin concentrations (3.8I).

While dynein-based transport is supported by Ciliobrevin A treatment, there still exists the possibility that actin-based forces also contribute to organelle transport. To investigate this possibility, we treated syncytia with a range of concentrations of the F-actin inhibitor Latrunculin (10, 25, 50, 100 nM). Latrunculin treatments had a slightly decreased rate of transport (< 25% difference) as compared to the untreated, but the more apparent effect of the drug was its impact on the morphology of branches as concentrations increased (3.8C).

MT nucleating complexes localize to branch nodes independent of nuclear location.

MT localization and nuclear transport to nodes after nocodazole treatments led us to hypothesize that nodes rather than branches are the primary sites of MT nucleation. Gamma-tubulin ring complexes (ɣ-TURC) may initiate MT polymerization at the site of a new branch in the bifurcation or anastomosing process during syncytial outgrowth. To determine where the extensive MT network is nucleated and organized, we stained fixed syncytia with an AlexaFluor conjugated gamma-tubulin antibody (3.9A). Gamma tubulin staining was diffuse throughout the MT network but had robustly stained puncta in branch nodes (3.9B). To confirm the gamma tubulin localization, we additionally raised antibodies specifically to the *Filoreta* GCP3 sequence (Methods). The GCP3 staining colocalized to the gamma-tubulin sites (9E, F), and was also enriched within branch nodes (3.9C, D). In the syncytial hubs, where there are numerous nuclei, we observed that gamma tubulin and GCP3 puncta colocalized, but did not coincide with nuclear location, additionally confirming that MT organization is not centralized around nuclear location (3.9E, F). In the larger branches emanating from hubs, both GCP3 and gamma-tubulin colocalize in puncta at the node junctions (E, F inset).

EB1 localizes to nuclei in distinct puncta

To determine the orientation of MT in the syncytial network, we generated antibodies to one of two *Filoreta* EB1 homologs We expected to see EB1 signal intensity at the syncytial periphery where the MTs proliferated branchlets at their plus ends (3.10A). Unexpectedly, the EB1 staining diffusely labeled the entire MT network and did not significantly label peripheral MTs. However, EB1 staining did robustly stain puncta at the sites of nuclei at the periphery (3.10A) and the interior of the syncytium (3.10B). Specifically, many EB1 puncta appeared to organize in a ring surrounding nuclei (3.10A, B, inset). The EB1 signal intensity was higher when

colocalized with nuclei (3.10C). To verify this finding and ensure the EB1 signal was not originating at nodes that happened to include nuclei, we compared the intensities of EB1 puncta overlapping with nuclei and EB1 signal in nodes of the network lacking nuclei. Both intensity maxima and averaged signal per area were significantly different between nuclei and nodes.

Discussion:

Branching and anastomosing networks are a common amoeboid morphological feature found in diverse eukaryotic clades, including Amoebozoa, Stramenopiles, Rhizaria, and Opisthokonts (Berney et al., 2015; Preston and King, 2005; Sachkova et al., 2021). Due to the overall lack of study in lineages outside of the Opisthokonts (Metazoans and Fungi), it remains unclear whether branched morphologies are an ancestral feature in the eukaryotes, or whether this phenotype has evolution multiple times in multiple lineages. For the former, one would expect that that similar mechanisms that generate branched networks are shared between diverse lineages. For the latter, one would expect different molecular and cellular mechanisms required to generate branched morphologies.

In general, generating a branched morphology requires specific microtubule (MT) and actin dynamics and interactions, which constrain the cytoplasmic volume while enabling a long "reach" for a cell. This cellular adaptation is useful for microbial "lifestyles" that require microbial eukaryotes to span large distances while maximizing cell-surface to volume ratio. Two contrasting such lifestyles are unicellular amoebae in a dynamic environment that searching for prey, or in multicellular organisms, neurons that are developing synapses across tissues (Luczak, 2010; Pfenninger, 2009). MT arrays in neurons organize longitudinally and provide a stabilized scaffold from which new branching can elaborate, either laterally or by leading edge (growth

cone) bifurcation (Ferreira Castro et al., 2020). Tightly regulated actin-MT interactions provide control over polarity, direction, and force-generation for developing neural branches, or neurites (Biswas and Kalil, 2018; Dent and Kalil, 2001; Pacheco and Gallo, 2016). To overcome the problem of diffusion-limited processes that large, branched cells encounter, active transport is critical for maintenance and dynamic interactions.

***Filoreta*'s actin and MT cytoskeleton mimic those defined in neuronal development and arborization.**

MTs stabilize branches in neuronal growth cones and neurites, and are regulated for determining branch location, orientation, transport, signal transduction; all of which are underlying functions for determining the highly branched morphology (Kapitein and Hoogenraad, 2011).

Pseudopodia used in adhesion, crawling, and bacterial prey capture incorporate MTs oriented toward the actin-rich site of phagocytosis— a key MT-actin interaction reminiscent of MT regulation in neuronal growth cone turning and signaling. In other amoeboid cells, the actin cytoskeleton required for crawling motility or response to stimuli derives from the MT array distribution. MT plus-end dynamics combined with actin interactions confer the path of migration in amoeboid cells (Kopf et al., 2020). MTs in lamellipodia exhibit curvature, much like the MT arrays observed in neuronal growth cones prior to actin-MT binding, or "capture" by F-actin (Jean et al., 2012). In *Filoreta* lamellipodial projections that had captured bacterial prey prior to fixation, MT proliferation into those pseudopodia oriented towards the captured bacteria (3D-E), indicating the role of external stimuli for directional pseudopod stabilization, and "turning" via the MT network.

The actin cytoskeleton in neuronal arbors stabilizes membrane-actin organization and is important in generating actin patches for pseudopodial (filopodial) projections prior to collateral branching (Gallo, 2011). The actin cytoskeleton is also important in morphogenesis of developing arbors by maintaining shape, MT anchoring, adhesion and force generation (Venkatesh et al., 2020). In *Filoreta*, collateral branches are also initiated by actin-based pseudopodia (3.1C, I). Branches are actin-enriched at the submembrane cortex (3.2C) and Latrunculin treatments confer a loss of new pseudopodia and branchlets (3.6C-D, G).

Actin is also required for adhesion to surfaces and in amoeboid cells (Schaks et al., 2019; Svitkina, 2018). In neurons, Latrunculin results in loss of actin polymer at the sub-membrane, diminishes the strength and stability of the actin-PM interface. This actin polymer collapse coincides with the degeneration of branches (Venkatesh et al., 2020). Latrunculin also had similar effects in *Filoreta*, with the exception of internal topology that was MT-stabilized. The MT-based looped structures were still visible after treatment with latrunculin, even when all actin-only loops (branchlets) had been lost (3.7E). Thus, the actin-based branchlets are required for outward growth via pseudopodial crawling, and directed MT proliferation into branchlets stabilizes them for the network to grow outward. This coordination of the actin and MT cytoskeleton is analogous to MT-actin interactions at the leading edge of a growth cone and MT proliferation in dendritic arborization (Conde and Cáceres, 2009; Tanaka et al., 1995).

The dynamic actin cytoskeleton forms the pseudopodial branchlets, which present as lamellipodia and branched filopodia that collect bacterial prey and extend outward via pseudopodial crawling. Branchlets are largely transient and collapse, fold inward, and reorganize constantly, often fusing to make loops, which are also transient (3.1A, B). Branches become stabilized for further elaboration as the loops thicken, which coincides with MT proliferation into

branchlets (3.1I, 3.2A-B, 3.2E-F). Peripheral network growth and branch initiation is dependent upon actin dynamics, and that branchlet-to-branch transition and retention (internal topology) requires MTs (3.6A-G, 3.7E). When treated with nocodazole, the MT dynamics shift toward depolymerization, and internal branches destabilize and retract to proximal nodes (3.6A-B, 3.7A-B). The proliferation of MTs into branchlets at the periphery is also diminished, affecting the stability of outward growth and the distribution of MTs at the transition zone (3.7C-D).

***Filoreta*'s cytoskeletal networks confer rapid and long-ranged organelle transport.**

Like other Rhizarian networks (Orokos et al., 2000; Schliwa et al., 1991), *Filoreta's* MT-based network constantly traffics organelles throughout the syncytium using active transport. Transport of nuclei and other organelles is an integral part of the *Filoreta* life cycle and requires MTs for transport throughout branches. We show that organelle transport loosely depends on the number of MTs in branches (3.2E-G, 3.4E-F), where motor proteins may be able to additively cooperate for increased efficacy of cargo transport. The bidirectional and unusually fast nature of these movements mirrors those previously described in the freshwater Rhizarian amoeba, *Reticulomyxa*, which occur by MT sliding (Orokos et al., 2000). Transport of cell components by MT sliding involves dynein and is bidirectional in both Rhizarian networks and in neurons (Guha et al., 2021). The MT arrays of *Reticulomyxa* were reported to only exhibit parallel, plus-end-out orientation (Euteneuer et al., 1988). *Reticulomyxa's* anterograde and retrograde transport in re-animated MT arrays corroborated this finding (Orokos et al., 2000). In ATP-reactivated membrane-extracted cytoskeletal networks, MT fragments slide along other MTs in the network via motor proteins. Further examination of the extracted cytoskeleton indicated that MT-MT sliding is essential for organelle transport, a phenomenon that has since become integral to our

understanding of MT-based transport in more recent years (Jolly et al., 2010; Koonce et al., 1987).

Initially there was skepticism of the MT-MT sliding mechanism in neurons, as results were confounded with both MT dynamics and observed motor protein rates, but it has been corroborated in other cytoskeletal studies in the years since (Lu and Gelfand, 2017; Myers et al., 2006; Winding et al., 2016). Both cytoplasmic dyneins and kinesins have been shown to be involved in neuronal organelle transport (Guha et al., 2021; Koppers and Farías, 2021). In axons, parallel MT bundles exhibit bidirectional organelle transport mediated by both kinesin (anterograde) and dynein (retrograde). Treatments with ciliobrevin resulted in loss of axonal transport for both directions, even though ciliobrevin has specificity to dynein motors (Sainath and Gallo, 2015). Our results in *Filoreta* mirror this effect, in which increasing concentrations of ciliobrevin result in loss of all transport, not just in one direction. However, at low concentrations, ciliobrevin only slows transport, but bidirectional processive movement is not lost (3.8I). Thus while organelle transport largely employs cytoplasmic dyneins in *Filoreta*, little work has been done to discern the potential sensitivities of Rhizarian kinesin motors to Ciliobrevin, or loss of kinesin processive movement as a result of dynein inhibition. Ciliobrevin is also reported to affect the recruitment and maintenance of dynein-dynactin complex localization and activity on MT arrays transporting organelles (Sainath and Gallo, 2015).

Where MTs and dynein motors appear to be the main players for organelle transport, actin exhibits a supporting role (Ruthel and Banker, 1998; Venkatesh et al., 2020). We suggest an additional role for the actin cytoskeleton in facilitating transport, as increasing concentrations of Latrunculin slowed organelle movements (3.8C, G). Even low concentrations of Latrunculin (25 nM) resulted in sensitivity of the network to UV exposure, and increased likelihood of retraction

and beading (detachment from the surface). We hypothesize that the depletion of actin from branches reduces the adhesion of the syncytium to the culture surface, resulting in this sensitivity. Additionally, the role of dynein-dynactin and actin-tethering proteins is important for MT transport (Ahmad et al., 1998; Guha et al., 2021) and in reticulopodia for force generation against the adhered substrate (Myers et al., 2006).

Although the unusual rates of transport of organelles in *Filoreta* match with those reported in *Reticulomyxa*, the assessment of organelle transport in extracted MT arrays did not account for organelles traveling at different rates along the same MT bundle, as was observed in *Filoreta* branches (3.4B-C). There are several ways in which this could occur, including varying numbers of motor proteins per MT fragment, allowing for differences in rates even along the same MT bundle (Schroeder et al., 2010). Bidirectionality could be due to antero- and retrograde activity of motor proteins transporting fragments, but also corroborates *Filoreta's* potential antiparallel MT bundling in complex (multinodal) branches.

In contrast to *Reticulomyxa's* parallel "plus-end-out" MT arrays (Euteneuer et al., 1988) and the MT orientation of axons, our results demonstrate that *Filoreta's* looped network likely incorporates antiparallel bundling and partial plus-end-in orientation (3.6B). The mixed-polarity of the MT network at the peripheral branchlets and interior loops may have a role in syncytial organization and distribution of organelles more akin to dendritic arbors (Mitchell and Wildonger, 2023; Ori-McKenney et al., 2012).

When we sought to resolve the orientation of MTs at the periphery via EB1 immunofluorescence, we unexpectedly encountered localization of EB1 puncta to nuclei (3.10A,

B). In many instances, the puncta were organized into rings around the perimeters of nuclei, similar to interphase *Dictyostelium* EB1 and *Arabidopsis* EB1C (Komaki et al., 2010; Rehberg and Gräf, 2002). In Drosophila, fat body and muscle cells also have a similar localization, where a perinuclear non-centrosomal MTOC interacts with EB1, spectraplakins, kinesins and dyneins to coordinate nuclear positioning and plasticity to withstand cytoplasmic strain (Wang et al., 2015; Zheng et al., 2020). It is possible that *Filoreta's* EB1 works in a similar manner, as nuclei are constantly trafficked and compress to less than 25% of their diameters as they move through narrow branches (Chapter 2 – nuclear plasticity). Additionally, we discovered that this particular *Filoreta* EB1 homolog has a unique C-terminal Nup88 domain, indicating a potential novel function linking EB1 to the nuclear pore structure, and may have a role in nucleocytoplasmic transport (Chapter 2). Further investigation into the function of this protein and its domain conservation in Rhizaria is warranted.

Filoreta syncytia lost a significant amount of internal branch topology during the pruning process in its cell cycle (Chapter 2), while under stress (3.5C-F), and during nocodazole treatments when MTs depolymerized from their plus ends (3.6B, F). This affected the nuclear trafficking by reducing the MT distribution, thus limiting branches nuclei traveled through (3.8H). Nocodazole-induced depolymerization also results in diminished branch stability and eventual retraction of the branch from the network interior to the nearest node from which the MT minus end is located (3.6B, G). The morphological changes and branch retraction during pruning in *Filoreta* were similar to neurite pruning and thus we argue that syncytial pruning and neurite pruning have the same underlying mechanism. Pruning in neurons is an important process during neuronal maturation and synaptic maintenance, in which the topology of the neuronal processes changes to increase efficiency (Faust et al., 2021). Pruning in both *Filoreta*

and neurons can also be caused by stressors and local changes in the environment, including trophic deprivation (Maor-Nof et al., 2016, 2013).

Neurite pruning is regulated by MT stabilization and involves MT associated proteins (MAPs) like Tau, MAP1B, MAP6, and the MT-depolymerizing kinesin Kif2A (Biswas and Kalil, 2018; Herzmann et al., 2017; Rumpf et al., 2019). Post-translational modifications (PTMs) that affect MT stability are involved in regulating pruning sites (Baas et al., 2016; Maor-Nof et al., 2013; Tint et al., 2005). In the highly regulated process of dendrite pruning, Tau phosphorylation by the kinase PAR-1 destabilizes bundled MTs and leads to their depolymerization and branch retraction (Herzmann et al., 2017). Further, the MT-stabilizing drug paclitaxel disrupts axonal pruning initiated by trophic deprivation by maintaining MT stability (Maor-Nof et al., 2013). Such an experiment with *Filoreta* would require its beta-tubulin to contain the taxol-binding pocket, a region in which most of the residues have been altered in Rhizarian relatives (Habura et al., 2005). The genes responsible for the retractive pruning response in neurons by cytoskeletal regulation, like Kif2A, Tau, PAR-1, MAP1B, and MAP6 have not been identified in the *Filoreta* genome.

Transcriptional control of neurite pruning is specific to neuron type and animal system; they typically involve specific hormone receptors and their targets (i.e., EcR-B1 with Sox14 in flies and hormone receptors in mammals) (Kirilly et al., 2009). Such transcriptional regulators and pathways have not yet been resolved in the *Filoreta* genome. However, preliminary findings from the *Filoreta* genome (Chapter 2) contain neuron-like signaling pathways including synaptic vesicle glycoprotein 2B, diacylglycerol lipases (DAGLs), and several GABA receptors, whose activity is responsible for pyrimidal neuron pruning in mice (Parato et al., 2019). *Filoreta* also has a homolog to the ubiquitin ligase Phr1/MYCBP2, which regulates neuron morphology by

inhibiting axonal overgrowth through p38 MAPK-mediated changes in microtubule stability (Babetto et al., 2013; Lewcock et al., 2007).

Individual cells respond to environmental stimuli by controlling traffic of RNA to specific subcellular regions, and the subsequent activity of the localized RNA (Engel et al., 2020). In syncytial organisms, this distance can be very large, posing a problem for regulation of RNA to regional stimuli. In *Filoreta*, we expect many nuclei must coordinate within the syncytium to provide local transcriptional control throughout the network, like the spatially differentiated transcriptomes in the syncytial Amoebozoan *Physarum* (Gerber et al., 2021). This dynamic response, we hypothesize, requires nuclear trafficking to mount localized transcriptional changes, and is essential for the dynamic control of branch growth, retention, and pruning as the syncytium interacts with its environment.

***Filoreta*'s MT cytoskeleton is nucleated independently of nuclear (MTOC) location.**

In *Filoreta*, MT nucleation likely originates at nodes of existing MT-filled branches, and not at canonical nuclear-associated MT organizing centers (MTOCs). Both gamma tubulin and the *Filoreta* GCP3 homolog colocalize and are enriched in branch nodes, indicating the gamma-TURC nucleation sites are not limited to the centrosomal MTOCs typically associated with nuclear location (Shokrollahi and Mekhail, 2021).

As previously stated, nocodazole-treated MTs depolymerized to their minus ends at nodes (3.6B, 7B, D). Nuclei are trapped in nodes following the loss of trafficking during MT depolymerization. Further, gamma-tubulin and GCP3 shows more robust puncta in nodes rather

than in minor and major branches (3.9A-D). The puncta of these two conserved gamma-TURC components do not coincide with nuclear location (3.9E-F).

In cells that develop interphase MT arrays covering large distances, MT nucleation is promoted from preexisting MTs rather than being centrosomally anchored (Ishihara 2014, Basnet 2018). Such non-centrosomal interphase MT arrays are not uncommon, and occur in in fungi (Daga et al., 2006), plants (Lee and Liu, 2019), neurons (Sánchez-Huertas et al., 2016), muscle cells, and other non-migratory cell types (Keating and Borisy, 1999). Specifically, MT-dependent MT nucleation (or branched nucleation) is of interest because of the potential diversity of nucleation machinery for lateral branching including Augmin, TPX2, SSNA1, and XMAP215 (Alfaro-Aco et al., 2020; Basnet et al., 2018; Ishihara et al., 2014; Petry et al., 2013). With the exception of XMAP215, the known nucleation machinery is not present in the *Filoreta* genome (Chapter 2). Where many have inferred evolutionary relationships across the eukaryotes by comparing MTOC structure and function (Yubuki and Leander, 2013), few have incorporated ncMTOC MT-dependent nucleation into evolutionary cell biology studies. *Filoreta* presents as an interesting model for this facet of MT nucleation research because it exists as an amoeboid cell type that develops in a non-migratory manner.

We predict that further examination of the gamma-TURC localization and activity may indicate whether MT branching truly occurs in nodes initiated by pseudopodial activity, or if they are nucleated elsewhere and transported as “seeds” via the hypothesized MT-MT sliding (Baas et al., 2006; Guha et al., 2021). Future work could include a gamma tubulin inhibitor to arrest nucleation events (Chinen et al., 2015), so that only existing MTs can elongate. If nucleation sites are anchored laterally to existing MTs, the network topology will likely depreciate in branch complexity as the syncytium grows outward.

Conclusion

Our work outlines the cytoskeletal dynamics behind the complex morphogenesis of an arborized non-model protist. *Filoreta's* utility as an emerging model system is multi-faceted and has implications for understanding the evolution of actin-MT interactions, arbor simplification via pruning, interphase MT arrays, rapid MT-based organelle transport, and MT nucleation machinery.

Numerous further questions arise from the foundation this work has laid out. Do the nuclei in syncytia move because they need to control localized transcriptional responses? Are microtubule arrays constantly sliding, or do they become anchored at a certain point in branch development like in axons? Do the actin-microtubule interactions drive pseudopodia towards environmental stimuli in a manner akin to growth cone turning? Are anastomosing networks like *Filoreta* and ctenophore neural nets an ancestral state of differentiated metazoan neurons? Anastomosing networks occur in the Stramenopiles, Amoebozoa, Rhizaria and Opisthokonts, in which the organisms cover large distances while maintaining dynamic interactions with their surroundings (Berney et al., 2015; Preston and King, 2005; Sachkova et al., 2021). This morphology is driven by conserved cytoskeletal components, yet the mechanism(s) remain relatively unresolved for free-living protists.

Filoreta represents a new organism in which to examine conserved features between Metazoan neurons and Rhizarian amoebae, and its ease of maintenance in the laboratory and reasonable genome size (Chapter 2) make it amenable to further study and development as a new model (Matthews and Vosshall, 2020). Although not yet genetically tractable, we show *Filoreta's* utility for investigating cytoskeletal dynamics through drug treatments and immunofluorescence assays.

Considering the numerous similarities in morphology and cytoskeletal organization between *Filoreta* and metazoan neurons, the dynamics and mechanisms we described here could have broad implications for understanding the evolution of arborized morphology.

Materials and Methods

Filoreta culture conditions:

Filoreta strain SW4B was isolated in September 2014 from brackish sediment samples collected in July 2014 at the Little Sippewissett Marsh in Massachusetts (41°34'33.6"N 70°38'22.7"W). The strain has been stably maintained at room temperature in these conditions. Cultures were grown at room temperature (~22°C) in monoeukaryotic culture in 75 cm^2 surface-treated flasks (Falcon™ 353135) containing 50ml of sterile artificial seawater base (SWB) (NaCl (423mM), KCl (9mM), CaCl2 dihydrate (9.27mM), MgCl2 hexahydrate (22.9mM), MgSO4 heptahydrate (25.5mM), NaHCO3 (2.14mM), buffered with 5 mM MOPS, and filter sterilized.

SWB was enriched with 0.01% final concentration of Yeast Extract and Tryptone (filter sterilized) immediately prior to addition to the culture to promote growth of bacterial prey. Active syncytia were maintained by refreshing enriched culture medium every 24-48 hours and were observed to fully encyst 72-96 hours after the removal of bacterial suspension and refilled with plain seawater medium.

Individual amoebae were grown in shallow dishes containing 0.05% YET over 48 hours, or harvested from plates when grown on a lawn of *Maribacter* sp. “prey” bacterial food as described in Chapter 1.

Generation of custom antibodies

Polyclonal rabbit antibodies were generated using Genscript's PolyExpress Antibody services. Specific peptides derived from EB1 and GCP3 homologs were selected for their location within the proteins, affinities and their predicted antigenic regions. Regions within GCP3 N-terminal end included peptides CAQSSEGSEAPPATK, TKQTSPQKPESERVC and

LKRMLRNDRTKLVEC. For the EB1 homolog, we used CSRSSGASRKPAGTR, KSGGKPKKARGVTRC and CTRSSTSTPSRSTSG.

Fixation and cytoskeletal immunostaining:

Syncytia grown to high confluence in culture flasks were gently removed using cell scrapers (GeneMate T-2443-1). Cell suspensions were added to glass coverslips pre-coated in 0.1% cold-water fish skin gelatin (Sigma G7765), placed into separate wells of a rectangular 8-well dish (Thermo 267062). Syncytial fragments were allowed to adhere for ranges of time varying from 30 minutes to 12 hours, depending on the stage of growth to be observed (30 minutes for new fragment fusions, 1-6 hours for syncytial outgrowth, 8-12 hours for syncytial pruning, hub formation, encystation). Prior to fixation, the coverslips were submerged for five minutes in filter sterilized calcium-free artificial seawater to remove excess calcium from the medium (NaCl (469 mM), KCl (10 mM), $MgCl_2$ (36 mM), $MgSO_4$ (17 mM), HEPES-NaOH (10 mM, pH 8.2), EGTA (10 mM)). Three protocols were developed and used for fixation of the marine amoeba included three fixative methods:

Paraformaldehyde (4%) fixative (20ml calcium-free seawater containing 0.4 M sucrose, 8ml cytoskeletal stabilizing buffer (CSB) (recipe below), 4ml 32% paraformaldehyde) was added for 10 minutes. CSB was prepared as a 10x stock and contained 50 mM KCl, 1.37 M NaCl, 40 mM NaHCO3, 110 mM Na2HPO4, 20 mM MgCl2, 50mM PIPES, 20 mM EGTA.

Glutaraldehyde fixative (0.5% glutaraldehyde, 5% sucrose, in calcium-free seawater buffered with 1X CSB) was added for one minute.

Glyoxal fixative (1.5ml of 40% glyoxal (Sigma 128465), 2ml ethanol, 1ml CSB, 7ml calcium-free seawater) was added for 30 seconds. Each fixation was quenched by three successive two-minute washes in PEM (100 mM PIPES, 1 mM EGTA, 0.1 mM MgSO4) (Woessner and Dawson, 2012), followed by a 10-minute permeabilization in 0.1% Triton-X 100, blocked in PEMBALG (PEM containing 1% bovine serum albumin, 0.1% sodium azide, 100 mM lysine, and 0.5% cold-water fish skin gelatin (Sigma G7765)) (Woessner and Dawson, 2012). In glutaraldehyde fixation, 0.2 M Glycine was added for 30 minutes to quench unreacted aldehydes to reduce autofluorescence.

Primary antibodies were incubated on coverslips at optimized concentrations (Mu-α-TAT1= 1:500), Rb-α-GCP3=1:1000 (Custom antibodies GenScript PolyExpress Gold – *Filoreta* GCP3 peptides), Rb-α-ɣ-Tubulin=1:1000 (Abcam ab205475) for one hour at room temperature, then washed three times in PEMBALG prior to incubation with the secondary antibody Alexa fluor 488, 594, 647 conjugates(1:1000) for the same duration at room temperature in a dark cabinet. Actin networks were labeled using a 1:1000 concentration of Phalloidin-AlexaFluor 488 conjugate in PEM for 10 minutes (PFA or Glutaraldehyde fixation only). Nuclei were labeled by counterstaining in a 1:1000 dilution of DAPI in PEM for 10 minutes in a dark cabinet. Slides were mounted with (SlowFade™ Diamond Antifade Mountant S36963).

Multichannel acquisition of stained syncytia was performed with widefield microscopy on a Leica DMI6000B with filter cube set N3, A4, L5, Cy5 and captured using a Prime 95B sCMOS camera. Images were analyzed in FIJI (imageJ) and maximum intensity projections (MIPs) were generated for structural analysis.

Live differential interference contrast (DIC) imaging:

Syncytia grown to high confluence in surface treated culture flasks were gently rinsed in sterile medium, scraped, and suspensions were added to 30mm Mattek dishes with glass coverslips coated with 0.1% gelatin. Syncytial fragments were allowed to adhere for ranges of time varying from 30 minutes to 12 hours, depending on the stage of growth to be observed (30 minutes for new fragment fusions, 1-6 hours for syncytial outgrowth, 8-12 hours for syncytial pruning, hub formation, encystation). Live imaging used differential interference contrast (DIC) with a Leica DMI6000B with shutter set to "open" on low light levels (10%) for growth and shutter set to "auto" for pruning. Timelapse movies were captured at one second intervals.

Sholl analysis of arborization:

Discrete time points were isolated from imaging data and processed prior to quantification of arborization. DIC images were background cleaned in FIJI, where a duplicate image is Gaussian blurred, then divided against the original image to remove artifact background shading (REF). Ideal thresholding levels varied by gray values across different image series, but each time point in a given series used identical thresholding parameters. Excess pixel noise was removed using "Analyze Particles" to generate masks for objects smaller than 10 pixels. The binary images corresponding to time points in a series were synchronized and identically annotated with a line drawn from a central point (identified as a syncytial hub or major branch node) towards the periphery of the image. Identical parameters were used in FIJI's Sholl Analysis software across all treatments. Sholl Intersection Profiles (SIPs) generated by the software were exported and used in Prism GraphPad to extrapolate further values in "Growth rate" and "Area under curve". The intersection number within serial spheres of 1 μm radii was plotted as a function of radial

distance from the center. Plots generated from images within the same time series were plotted together, and SIP peaks were used to quantify the change in network diameter over time.

Branch growth rate measurements

Sholl profiles were exported from FIJI for use in Graphpad Prism Software. Profiles were plotted along an X-Y graph, and the Y-value (number of intersecting branchlets) of the half-maximal peak for each Sholl profile in a series (0 min, 10 min, 20 min) was taken with its corresponding X-value (distance from center). The differences in these distances were taken and divided by minutes in the time series to generate a table of micrometer distance over one minute. Additional calculations included averaging growth measurements taken at one-minute intervals and averaged to ensure rates were not artificially elevated by using larger time intervals.

Area under curve measurements

Graphpad Prism Software analyses were used to quantify total surface area coverage by the syncytial network by generating “Area Under Curve” values for XY corresponding datasets. The area under curve data were generated using only raw values and not the “best fit” polynomial regressions produced in Sholl profiles. These AUCs were then compared across timepoints as a ratio to the original T=0 timepoint for each replicate, divided by time elapsed (for “per minute” values). Values increasing in AUC are reported as increased overall surface area (branch intersection numbers are maintained and/or increasing in number as the syncytial growth rate increases). Values decreasing in AUC are reported as decreased surface area (pruning/simplification, loss of branches, destabilization, or pseudopodial retraction).

Timelapse Sholl analysis of arborization

While each syncytial growth experiment was treated identically prior to imaging, there was no normalization of bacterial food presence in cultures other than the specific concentration of nutrient source provided. Since day-to-day imaging incorporated these potential sources of variation, we color coded data points by experimental day to indicate variation.

Live imaging of syncytia was performed at one second intervals (frame rate), and analyses used five- and ten-minute intervals for comparison of control and drug-treated growth rates and topology maintenance. Images were thresholded with identical parameters within each replicate. Sholl profiles generated in FIJI were compared for growth rate (distance to most peripheral pseudopod radial intersection) and topology (area under curve, "total peak area" of datapoints graphed in GraphPad Prism Software).

Fluorescence Sholl analysis of arborization

Images were prepared from raw data by thresholding maximum intensity projections (MIPs) using Fiji (normalized to each color for comparative 2-channel fluorescence Sholl). Center points were selected as the main nodes for multiple branches in broad scale syncytia, and main branch nodes for peripheral branchlet arbors, respectively. The comparison of actin and MT Sholl profiles used the ratio of total peak area for each channel's profile, in which branch intersections were normalized to each acquisition by using identical thresholding and Sholl profile parameters. The total area of MT SIPs were divided by the total area of Actin SIPs to find the percentage of MT proliferation within the actin network. Identical parameters were used across drug treatments.

Quantification of organelle transport

Syncytia were stained in 96-well glass-bottomed plates, and in Mattek dishes pre-coated with 0.1% gelatin. Nuclei, mitochondria, and lysosomes were stained for 10 minutes at room temperature with Hoechst 33342, Syto9, and LysoTracker, respectively. Nuclei were imaged at 1 second intervals (50 ms exposure, 10% excitation power) under widefield fluorescence, while mitochondria and lysosomes were able to be imaged at 100 millisecond intervals. Imaging experiments incorporated controls per field imaged by imaging the first 60 seconds without drug, then added the drug at a 1:1 volume at the 60-second mark for each replicate. Syncytia that showed signs of phototoxicity within the 5 minutes of fluorescent light exposure (blebbing, beading, shriveling) were excluded from data collection to minimize stress response altering biologically relevant values.

Organelle trajectories were quantified using kymographs generated in FIJI plugin "KymoResliceWide" and verified using particle tracking software in the FIJI plugin "Trackmate". Kymograph measurements were quantified for processive movements of organelles moving 10 µm or more. Rates of transport were calculated from kymograph lengths and used to populate superplots in Prism GraphPad colorized per replicate (Lord et al., 2020). Drug-treated image series of organelle traffic kymographs were generated using identical parameters to their controls and compared between series' concentrations for each data set within GraphPad using ordinary one-way ANOVA and multiple comparison analyses compared against the control.

Gamma-tubulin and GCP3 analyses

Syncytia were grown and fixed on 0.1% gelatin-coated coverslips, then fixed using glyoxal and paraformaldehyde fixation and immunostaining methods outlined above. GCP3 and gamma-tubulin staining used Rabbit-anti-GCP3 (Rb-α-GCP3) at 1:1000 ratio (Custom antibodies GenScript PolyExpress Gold – *Filoreta* GCP3 peptides) and anti-gamma-tubulin at 1:1000 (Abcam ab205475). Syncytia were counterstained with DAPI and mounted with Slowfade (SlowFade™ Diamond Antifade Mountant S36963). Images were taken on a Leica DMI6000B with Prime95B sCMOS camera.

Images were analyzed using FIJI using measurement features over segmented lines with pixel withs of 15. Average grey values were calculated over branches and nodes and normalized to length and width of areas covered by branches and nodes. Branch thickness was measured using "plot profile" function and used to categorize measurements for "minor" and "major branches" compared to "nodes" which included three or more branch intersections. The grey values/area were plotted for each image using Prism GraphPad and colored per replicate.

EB1 localization analyses

Syncytia were grown and fixed on 0.1% gelatin-coated coverslips, then fixed using glyoxal method. Samples were stained with custom Rabbit-anti-EB1 at 1:1000 (Custom antibodies GenScript PolyExpress Gold – *Filoreta* EB1 peptides), and mouse-anti-alpha-tubulin antibody at 1:500 (TAT-1, an inherited gift from Keith Gull (Woods et al., 1989). Secondary antibodies were added at a 1:1000 ratio, using goat-anti-rabbit AlexaFluor488 conjugate and goat-anti-mouse AlexaFluor 594 conjugates as described above, then DAPI stained prior to mounting on slides with Slowfade. Images were taken on a Leica DMI6000B with Prime95B sCMOS camera.

Images were analyzed using FIJI using measurement features for ellipses drawn around nuclei, then quantified for mean and maximal gray values for each channel over that area. Identical measurements were made for nodes in each image, absent of nuclei. Maximal grey values of EB1 signal were directly compared for nuclei vs nodes in Prism GraphPad, with an unpaired t test. Mean grey value intensities over the area measured for EB1 signal were normalized to the mean intensities of TAT-1. The normalized values were compared in Prism GraphPad with an unpaired t test.

Literature Cited

Ahmad FJ, Echeverri CJ, Vallee RB, Baas PW. 1998. Cytoplasmic dynein and dynactin are required for the transport of microtubules into the axon. *J Cell Biol* **140**:391–401. doi:10.1083/jcb.140.2.391

Alfaro-Aco R, Thawani A, Petry S. 2020. Biochemical reconstitution of branching microtubule nucleation. *eLife* **9**:e49797. doi:10.7554/eLife.49797

Assoian RK, Bade ND, Cameron CV, Stebe KJ. 2019. Cellular sensing of micron-scale curvature: a frontier in understanding the microenvironment. *Open Biology* **9**:190155. doi:10.1098/rsob.190155

Baas PW, Rao AN, Matamoros AJ, Leo L. 2016. Stability properties of neuronal microtubules. *Cytoskeleton (Hoboken)* **73**:442–460. doi:10.1002/cm.21286

Baas PW, Vidya Nadar C, Myers KA. 2006. Axonal transport of microtubules: the long and short of it. *Traffic* **7**:490–498. doi:10.1111/j.1600-0854.2006.00392.x

Babetto E, Beirowski B, Russler E, Milbrandt J, DiAntonio A. 2013. The Phr1 ubiquitin ligase promotes injury-induced axon self-destruction. *Cell Rep* **3**:1422–1429. doi:10.1016/j.celrep.2013.04.013

Basnet N, Nedozralova H, Crevenna AH, Bodakuntla S, Schlichthaerle T, Taschner M, Cardone G, Janke C, Jungmann R, Magiera MM, Biertümpfel C, Mizuno N. 2018. Direct induction of microtubule branching by microtubule nucleation factor SSNA1. *Nat Cell Biol* **20**:1172–1180. doi:10.1038/s41556-018-0199-8

Berney C, Geisen S, Van Wichelen J, Nitsche F, Vanormelingen P, Bonkowski M, Bass D. 2015. Expansion of the 'Reticulosphere': Diversity of Novel Branching and Network-forming Amoebae Helps to Define Variosea (Amoebozoa). *Protist* **166**:271–295. doi:10.1016/j.protis.2015.04.001

Berney C, Romac S, Mahé F, Santini S, Siano R, Bass D. 2013. Vampires in the oceans: predatory cercozoan amoebae in marine habitats. *ISME J* **7**:2387–2399. doi:10.1038/ismej.2013.116

Biswas S, Kalil K. 2018. The Microtubule-Associated Protein Tau Mediates the Organization of Microtubules and Their Dynamic Exploration of Actin-Rich Lamellipodia and Filopodia of Cortical Growth Cones. *J Neurosci* **38**:291–307. doi:10.1523/JNEUROSCI.2281-17.2017

Black SE. 1981. "Pseudopods and Synapses": The Amoeboid Theories of Neuronal Mobility and the Early Formulation of the Synapse Concept, 1894-1900. *Bulletin of the History of Medicine* **55**:34–58.

Burkhardt P, Colgren J, Medhus A, Digel L, Naumann B, Soto-Angel JJ, Nordmann E-L, Sachkova MY, Kittelmann M. 2023. Syncytial nerve net in a ctenophore adds insights on the evolution of nervous systems. *Science* **380**:293–297. doi:10.1126/science.ade5645

Burki F, Keeling PJ. 2014. Rhizaria. *Current Biology* **24**:R103–R107. doi:10.1016/j.cub.2013.12.025

Chinen T, Liu P, Shioda S, Pagel J, Cerikan B, Lin T, Gruss O, Hayashi Yoshiki, Takeno H, Shima T, Okada Y, Hayakawa I, Hayashi Yoshio, Kigoshi H, Usui T, Schiebel E. 2015. The γ-tubulin-specific inhibitor gatastatin reveals temporal requirements of microtubule nucleation during the cell cycle. *Nat Commun* **6**:8722. doi:10.1038/ncomms9722

Conde C, Cáceres A. 2009. Microtubule assembly, organization and dynamics in axons and dendrites. *Nat Rev Neurosci* **10**:319–332. doi:10.1038/nrn2631

Daga RR, Yonetani A, Chang F. 2006. Asymmetric microtubule pushing forces in nuclear centering. *Curr Biol* **16**:1544–1550. doi:10.1016/j.cub.2006.06.026

Dent EW, Kalil K. 2001. Axon branching requires interactions between dynamic microtubules and actin filaments. *J Neurosci* **21**:9757–9769. doi:10.1523/JNEUROSCI.21-24-09757.2001

Engel KL, Arora A, Goering R, Lo H-YG, Taliaferro JM. 2020. Mechanisms and consequences of subcellular RNA localization across diverse cell types. *Traffic* **21**:404–418. doi:10.1111/tra.12730

Euteneuer U, Koonce MP, Pfister KK, Schliwa M. 1988. An ATPase with properties expected for the organelle motor of the giant amoeba, Reticulomyxa. *Nature* **332**:176–178. doi:10.1038/332176a0

Faust TE, Gunner G, Schafer DP. 2021. Mechanisms governing activity-dependent synaptic pruning in the developing mammalian CNS. *Nat Rev Neurosci* **22**:657–673. doi:10.1038/s41583-021-00507-y

Ferreira Castro A, Baltruschat L, Stürner T, Bahrami A, Jedlicka P, Tavosanis G, Cuntz H. 2020. Achieving functional neuronal dendrite structure through sequential stochastic growth and retraction. *eLife* **9**:e60920. doi:10.7554/eLife.60920

Gallo G. 2011. The cytoskeletal and signaling mechanisms of axon collateral branching. *Developmental Neurobiology* **71**:201–220. doi:10.1002/dneu.20852

Gerber T, Loureiro C, Schramma N, Chen S, Jain A, Weber A, Weigert A, Santel M, Alim K, Treutlein B, Camp JG. 2021. Nuclei are mobile processors enabling specialization in a gigantic single-celled syncytium. doi:10.1101/2021.04.29.441915

Glöckner G, Hülsmann N, Schleicher M, Noegel AA, Eichinger L, Gallinger C, Pawlowski J, Sierra R, Euteneuer U, Pillet L, Moustafa A, Platzer M, Groth M, Szafranski K, Schliwa M. 2014. The Genome of the Foraminiferan Reticulomyxa filosa. *Current Biology* **24**:11–18. doi:10.1016/j.cub.2013.11.027

Guha S, Patil A, Muralidharan H, Baas PW. 2021. Mini-review: Microtubule sliding in neurons. *Neurosci Lett* **753**:135867. doi:10.1016/j.neulet.2021.135867

Habura A, Wegener L, Travis JL, Bowser SS. 2005. Structural and Functional Implications of an Unusual Foraminiferal β-Tubulin. *Molecular Biology and Evolution* **22**:2000–2009. doi:10.1093/molbev/msi190

Hameroff S. 2010. The “conscious pilot”—dendritic synchrony moves through the brain to mediate consciousness. *J Biol Phys* **36**:71–93. doi:10.1007/s10867-009-9148-x

Herzmann S, Krumkamp R, Rode S, Kintrup C, Rumpf S. 2017. PAR-1 promotes microtubule breakdown during dendrite pruning in Drosophila. *The EMBO Journal* **36**:1981–1991. doi:10.15252/embj.201695890

Ishihara K, Nguyen PA, Groen AC, Field CM, Mitchison TJ. 2014. Microtubule nucleation remote from centrosomes may explain how asters span large cells. *Proceedings of the National Academy of Sciences* **111**:17715–17722. doi:10.1073/pnas.1418796111

Jean DC, Baas PW, Black MM. 2012. A novel role for doublecortin and doublecortin-like kinase in regulating growth cone microtubules. *Hum Mol Genet* **21**:5511–5527. doi:10.1093/hmg/dds395

Jolly AL, Kim H, Srinivasan D, Lakonishok M, Larson AG, Gelfand VI. 2010. Kinesin-1 heavy chain mediates microtubule sliding to drive changes in cell shape. *Proc Natl Acad Sci U S A* **107**:12151–12156. doi:10.1073/pnas.1004736107

Kapitein LC, Hoogenraad CC. 2011. Which way to go? Cytoskeletal organization and polarized transport in neurons. *Molecular and Cellular Neuroscience* **46**:9–20. doi:10.1016/j.mcn.2010.08.015

Keating TJ, Borisy GG. 1999. Centrosomal and non-centrosomal microtubules. *Biology of the Cell* **91**:321–329. doi:10.1016/S0248-4900(99)80093-8

Kirch C, Gollo LL. 2021. Single-neuron dynamical effects of dendritic pruning implicated in aging and neurodegeneration: towards a measure of neuronal reserve. *Sci Rep* **11**:1309. doi:10.1038/s41598-020-78815-z

Kirilly D, Gu Y, Huang Y, Wu Z, Bashirullah A, Low BC, Kolodkin AL, Wang H, Yu F. 2009. A genetic pathway composed of Sox14 and Mical governs severing of dendrites during pruning. *Nat Neurosci* **12**:1497–1505. doi:10.1038/nn.2415

Komaki S, Abe T, Coutuer S, Inzé D, Russinova E, Hashimoto T. Nuclear-localized subtype of end-binding 1 protein regulates spindle organization in Arabidopsis. J Cell Sci. 2010 Feb 1;123(Pt 3):451-9. doi: 10.1242/jcs.062703. Epub 2010 Jan 12. PMID: 20067996.

Koonce MP, Tong J, Euteneuer U, Schliwa M. 1987. Active sliding between cytoplasmic microtubules. *Nature* **328**:737–739. doi:10.1038/328737a0

Kopf A, Renkawitz J, Hauschild R, Girkontaite I, Tedford K, Merrin J, Thorn-Seshold O, Trauner D, Häcker H, Fischer K-D, Kiermaier E, Sixt M. 2020. Microtubules control cellular shape and coherence in amoeboid migrating cells. *J Cell Biol* **219**:e201907154. doi:10.1083/jcb.201907154

Koppers M, Farías GG. 2021. Organelle distribution in neurons: Logistics behind polarized transport. *Current Opinion in Cell Biology*, Membrane Trafficking **71**:46–54. doi:10.1016/j.ceb.2021.02.004

Lee Y-RJ, Liu B. 2019. Microtubule nucleation for the assembly of acentrosomal microtubule arrays in plant cells. *New Phytol* **222**:1705–1718. doi:10.1111/nph.15705

Lewcock JW, Genoud N, Lettieri K, Pfaff SL. 2007. The Ubiquitin Ligase Phr1 Regulates Axon Outgrowth through Modulation of Microtubule Dynamics. *Neuron* **56**:604–620. doi:10.1016/j.neuron.2007.09.009

Lord SJ, Velle KB, Mullins RD, Fritz-Laylin LK. 2020. SuperPlots: Communicating reproducibility and variability in cell biology. *Journal of Cell Biology* **219**:e202001064. doi:10.1083/jcb.202001064

Lu W, Gelfand VI. 2017. Moonlighting Motors: Kinesin, Dynein, and Cell Polarity. *Trends Cell Biol* **27**:505–514. doi:10.1016/j.tcb.2017.02.005

Luczak A. 2010. Measuring Neuronal Branching Patterns Using Model-Based Approach. *Frontiers in Computational Neuroscience* **4**.

Maor-Nof M, Homma N, Raanan C, Nof A, Hirokawa N, Yaron A. 2013. Axonal Pruning Is Actively Regulated by the Microtubule-Destabilizing Protein Kinesin Superfamily Protein 2A. *Cell Reports* **3**:971–977. doi:10.1016/j.celrep.2013.03.005

Maor-Nof M, Romi E, Sar Shalom H, Ulisse V, Raanan C, Nof A, Leshkowitz D, Lang R, Yaron A. 2016. Axonal Degeneration Is Regulated by a Transcriptional Program that Coordinates Expression of Pro- and Anti-degenerative Factors. *Neuron* **92**:991–1006. doi:10.1016/j.neuron.2016.10.061

Matthews BJ, Vosshall LB. 2020. How to turn an organism into a model organism in 10 'easy' steps. *Journal of Experimental Biology* **223**:jeb218198. doi:10.1242/jeb.218198

Mitchell JW, Wildonger J. 2023. Live Imaging of Golgi Outposts in Drosophila Dendritic Arbors In: Wang Y, Lupashin VV, Graham TR, editors. Golgi: Methods and Protocols, Methods in Molecular Biology. New York, NY: Springer US. pp. 635–644. doi:10.1007/978-1-0716-2639-9_38

Myers KA, Tint I, Nadar CV, He Y, Black MM, Baas PW. 2006. Antagonistic forces generated by cytoplasmic dynein and myosin-II during growth cone turning and axonal retraction. *Traffic* **7**:1333–1351. doi:10.1111/j.1600-0854.2006.00476.x

Ori-McKenney KM, Jan LY, Jan Y-N. 2012. Golgi Outposts Shape Dendrite Morphology by Functioning as Sites of Acentrosomal Microtubule Nucleation in Neurons. *Neuron* **76**:921–930. doi:10.1016/j.neuron.2012.10.008

Orokos DD, Cole RW, Travis JL. 2000. Organelles are transported on sliding microtubules in Reticulomyxa. *Cell Motility* **47**:296–306. doi:10.1002/1097-0169(200012)47:4<296::AID-CM4>3.0.CO;2-4

Orokos DD, Travis JL. 1997. Cell surface and organelle transport share the same enzymatic properties in Reticulomyxa. *Cell Motility* **38**:270–277. doi:10.1002/(SICI)1097-0169(1997)38:3<270::AID-CM5>3.0.CO;2-9

Pacheco A, Gallo G. 2016. Actin Filament-Microtubule Interactions in Axon Initiation and Branching. *Brain Res Bull* **126**:300–310. doi:10.1016/j.brainresbull.2016.07.013

Parato J, Shen H, Smith SS. 2019. α4βδ GABAA receptors trigger synaptic pruning and reduce dendritic length of female mouse CA3 hippocampal pyramidal cells at puberty. *Neuroscience* **398**:23–36. doi:10.1016/j.neuroscience.2018.11.032

Petry S, Groen AC, Ishihara K, Mitchison TJ, Vale RD. 2013. Branching microtubule nucleation in Xenopus egg extracts mediated by augmin and TPX2. *Cell* **152**:768–777. doi:10.1016/j.cell.2012.12.044

Pfenninger KH. 2009. Plasma membrane expansion: a neuron's Herculean task. *Nat Rev Neurosci* **10**:251–261. doi:10.1038/nrn2593

Preston TM, King CA. 2005. Actin-Based Motility in the Net Slime Mould Labyrinthula: Evidence for the Role of Myosin in Gliding Movement. *Journal of Eukaryotic Microbiology* **52**:461–475. doi:10.1111/j.1550-7408.2005.00064.x

Rehberg M, Gräf R. 2002. Dictyostelium EB1 is a genuine centrosomal component required for proper spindle formation. *Mol Biol Cell* **13**:2301–2310. doi:10.1091/mbc.e02-01-0054

Reynolds A. 2008. Amoebae as Exemplary Cells: The Protean Nature of an Elementary Organism. *Journal of the History of Biology* **41**:307–337.

Rumpf S, Wolterhoff N, Herzmann S. 2019. Functions of Microtubule Disassembly during Neurite Pruning. *Trends in Cell Biology* **29**:291–297. doi:10.1016/j.tcb.2019.01.002

Ruthel G, Banker G. 1998. Actin-dependent anterograde movement of growth-cone-like structures along growing hippocampal axons: a novel form of axonal transport? *Cell Motil Cytoskeleton* **40**:160–173. doi:10.1002/(SICI)1097-0169(1998)40:2<160::AID-CM5>3.0.CO;2-J

Sachkova MY, Nordmann E-L, Soto-Àngel JJ, Meeda Y, Górski B, Naumann B, Dondorp D, Chatzigeorgiou M, Kittelmann M, Burkhardt P. 2021. Neuropeptide repertoire and 3D anatomy of the ctenophore nervous system. *Current Biology* **31**:5274-5285.e6. doi:10.1016/j.cub.2021.09.005

Sainath R, Gallo G. 2015. The Dynein Inhibitor Ciliobrevin D Inhibits the Bi-directional Transport of Organelles along Sensory Axons and Impairs NGF-Mediated Regulation of Growth Cones and Axon Branches. *Dev Neurobiol* **75**:757–777. doi:10.1002/dneu.22246

Sánchez-Huertas C, Freixo F, Viais R, Lacasa C, Soriano E, Lüders J. 2016. Non-centrosomal nucleation mediated by augmin organizes microtubules in post-mitotic neurons and controls axonal microtubule polarity. *Nat Commun* **7**:12187. doi:10.1038/ncomms12187

Schaks M, Giannone G, Rottner K. 2019. Actin dynamics in cell migration. *Essays Biochem* **63**:483–495. doi:10.1042/EBC20190015

Schliwa M, Shimizu T, Vale RD, Euteneuer U. 1991. Nucleotide specificities of anterograde and retrograde organelle transport in Reticulomyxa are indistinguishable. *J Cell Biol* **112**:1199–1203. doi:10.1083/jcb.112.6.1199

Schroeder H (Trey) W, Mitchell C, Shuman H, Holzbaur ELF, Goldman YE. 2010. Motor number controls cargo switching at actin-microtubule intersections in vitro. *Curr Biol* **20**:687–696. doi:10.1016/j.cub.2010.03.024

Shokrollahi M, Mekhail K. 2021. Interphase microtubules in nuclear organization and genome maintenance. *Trends in Cell Biology* **31**:721–731. doi:10.1016/j.tcb.2021.03.014

Sholl DA. 1953. Dendritic organization in the neurons of the visual and motor cortices of the cat. *J Anat* **87**:387–406.

Šmít D, Fouquet C, Pincet F, Zapotocky M, Trembleau A. 2017. Axon tension regulates fasciculation/defasciculation through the control of axon shaft zippering. *eLife* **6**:e19907. doi:10.7554/eLife.19907

Svitkina T. 2018. The Actin Cytoskeleton and Actin-Based Motility. *Cold Spring Harb Perspect Biol* **10**:a018267. doi:10.1101/cshperspect.a018267

Tanaka E, Ho T, Kirschner MW. 1995. The role of microtubule dynamics in growth cone motility and axonal growth. *Journal of Cell Biology* **128**:139–155. doi:10.1083/jcb.128.1.139

Tekle YI, Williams JR. 2016. Cytoskeletal architecture and its evolutionary significance in amoeboid eukaryotes and their mode of locomotion. *Royal Society Open Science* **3**:160283. doi:10.1098/rsos.160283

Tint I, Fischer I, Black M. 2005. Acute inactivation of MAP1b in growing sympathetic neurons destabilizes axonal microtubules. *Cell Motility* **60**:48–65. doi:10.1002/cm.20045

Venkatesh K, Mathew A, Koushika SP. 2020. Role of actin in organelle trafficking in neurons. *Cytoskeleton (Hoboken)* **77**:97–109. doi:10.1002/cm.21580

Wang S, Reuveny A, Volk T. 2015. Nesprin provides elastic properties to muscle nuclei by cooperating with spectraplakin and EB1. *J Cell Biol* **209**:529–538. doi:10.1083/jcb.201408098

Winding M, Kelliher MT, Lu W, Wildonger J, Gelfand VI. 2016. Role of kinesin-1–based microtubule sliding in Drosophila nervous system development. *Proceedings of the National Academy of Sciences* **113**:E4985–E4994. doi:10.1073/pnas.1522416113

Woessner DJ, Dawson SC. 2012. The Giardia Median Body Protein Is a Ventral Disc Protein That Is Critical for Maintaining a Domed Disc Conformation during Attachment. *Eukaryotic Cell* **11**:292–301. doi:10.1128/EC.05262-11

Yubuki N, Leander BS. 2013. Evolution of microtubule organizing centers across the tree of eukaryotes. *Plant J* **75**:230–244. doi:10.1111/tpj.12145

Zheng Y, Buchwalter RA, Zheng C, Wight EM, Chen JV, Megraw TL. 2020. A perinuclear microtubule-organizing centre controls nuclear positioning and basement membrane secretion. *Nat Cell Biol* **22**:297–309. doi:10.1038/s41556-020-0470-7

Figure 3.1: Dynamic, reticulated branched networks define *Filoreta*'s syncytial development.

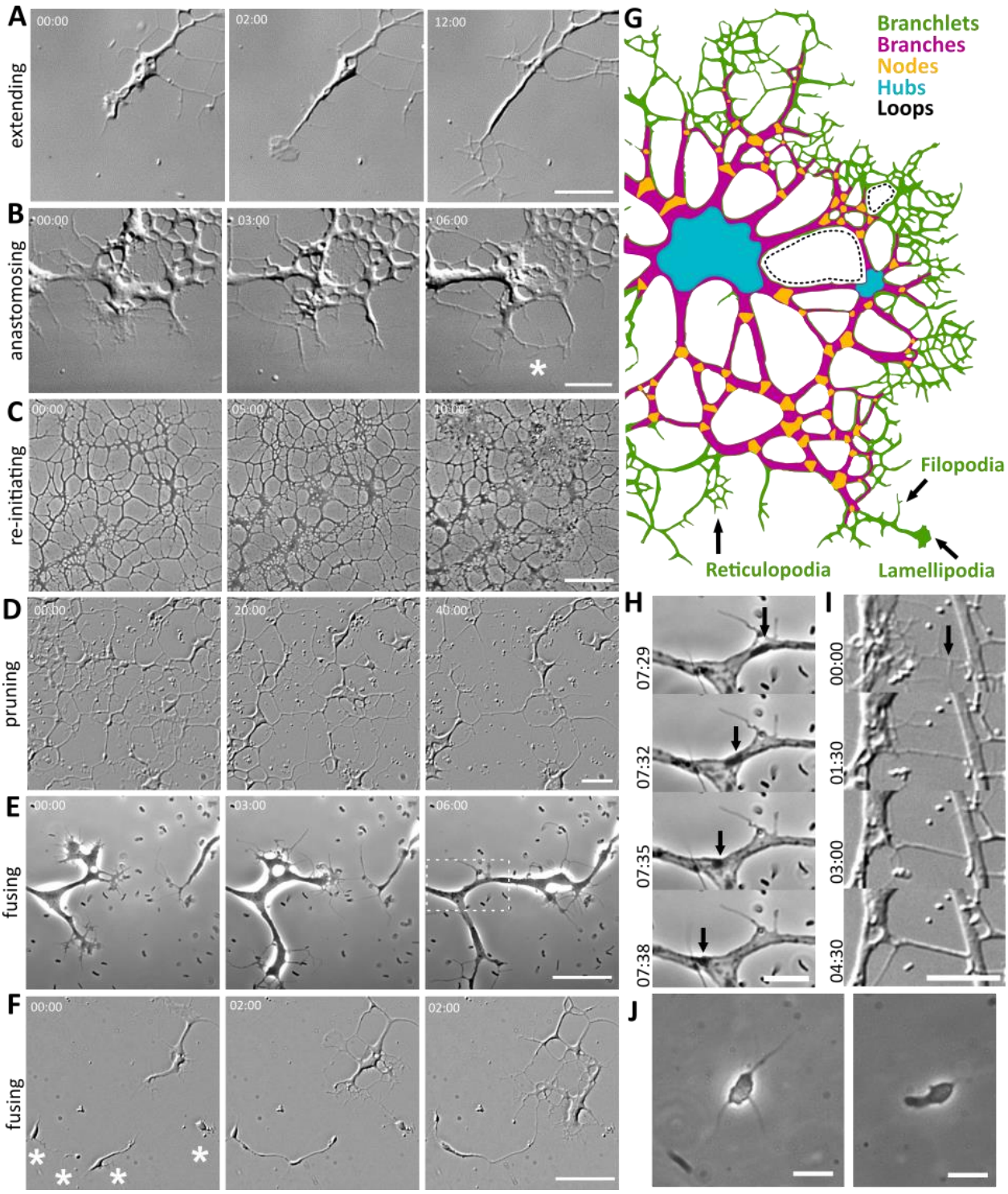

(A) Pseudopodial branchlets “extending” as they crawl outwards, constantly growing and retracting as lamellipodia and filopodia. Left panel = ruffled pseudopod, center = lamellipodia, right = branched filopodia. Scale = 10μm.

(B) Branchlets “anastomosing.” Self-fusion (asterisk) is known as anastomosis, which generates the looped structure of the syncytial network. scale=20μm.

(C) The syncytial network is dynamic and responds to the environment, re-initiating pseudopodia from simplified nodes upon addition of nutrient sources. scale=100μm.

(D) The syncytium responds to stress by pruning back its branches and retracting into hubs. scale=20μm.

(E) Syncytial neighbors recognize and fuse to each other. Inset rectangle in right panel was used in (H). scale=10μm.

(F) Individual amoebae fuse to each other and are recruited by a nearby syncytium. Scale=20μm.

(G) A colored diagram showing the morphology and associated terminology used to describe syncytial networks. Branchlets (green) = transient pseudopodial extensions that may be filopodia, lamellipodia or reticulopodia (bottom, arrows). Branches (magenta) = non-transient thicker lengths that make up the network. Nodes (orange) = intersecting points of two or more major branches that occur via bifurcation or anastomosis. Hubs (blue) = broad regions of cell body with five or more major branches intersecting. Loops (black) = closed circles occurring through anastomosis that may either be complete (filled in by branches, larger dotted region), or incomplete (partially bordered by branches or only by branchlets, smaller dotted region).

(H) A montage from inset in (E) with frame intervals of 3 seconds show an organelle traversing a branch node (arrows). Scale=10 μm.

(I) A montage with frame intervals of 90 seconds showing branchlet to branch transition and thickening (arrow). Scale=20µm.

(J) An individual amoeba forming filopodia (left) and a small lamellipodia-like pseudopod (right). scale=10µm.

Figure 3.2: *Filoreta* syncytia have distinct cytoskeletal architectures in pseudopodia and branches.

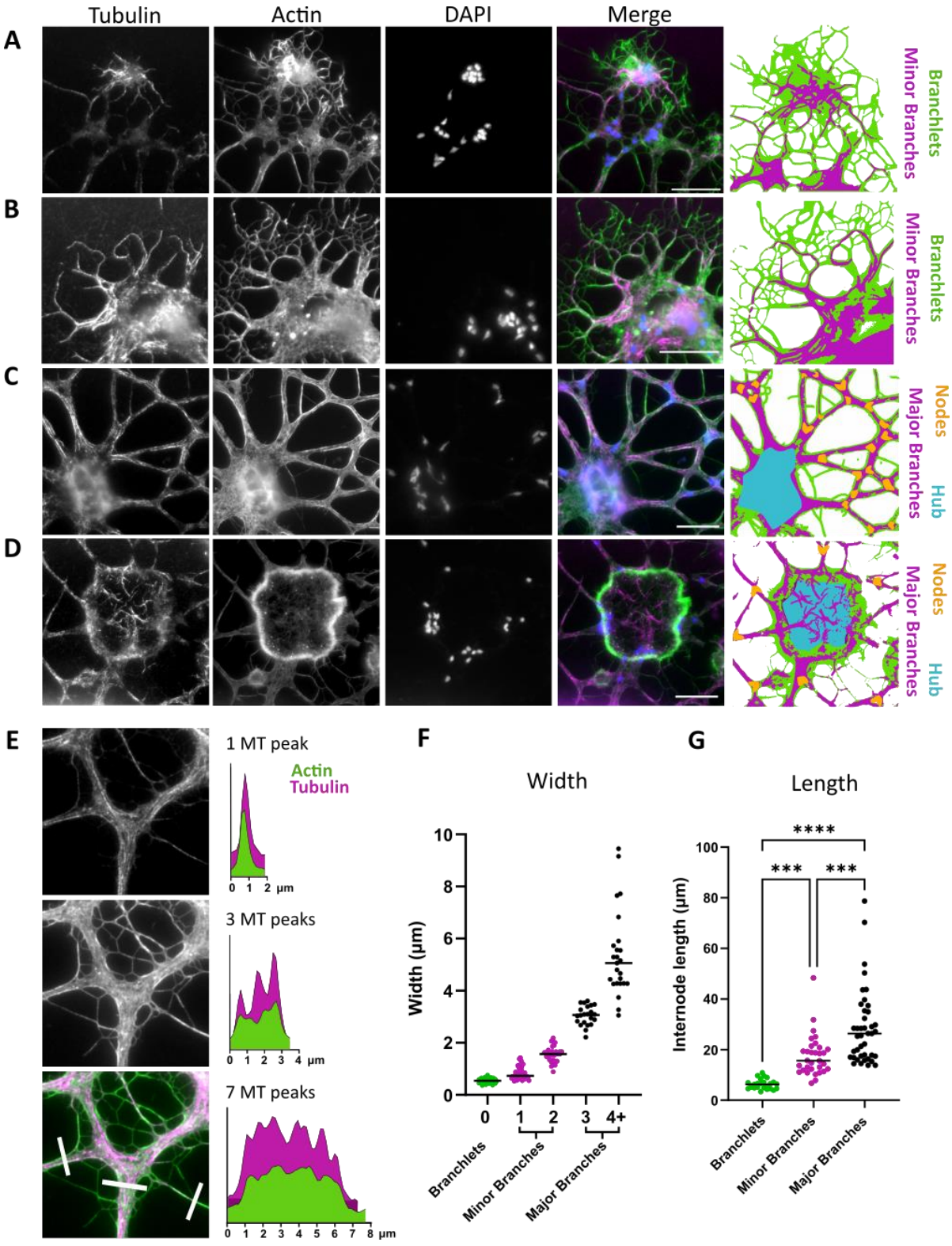

(A) A small syncytial fragment (top) fused to a larger syncytium (bottom) showing enriched actin at filopodial (branchlet) fusion sites. (Actin=Green, MTs=Magenta) Right panel shows cartoon of features and identification of branchlets and minor branches with newly proliferated MTs between syncytia. Scale=20µm.

(B) Peripheral branchlets show partial proliferation of MTs (magenta) in the filopodial actin network (green). Right panel shows cartoon of features highlighting proliferating MTs into anastomosed branchlets at the transition zone. None of the anastomoses are "completed" loops at the transition zone. Scale=20µm.

(C) The interior branches of the network include both actin and MTs. F-actin is found throughout and is enriched at the submembrane cortex (bright margins). Right panel shows cartoon of features and identification of completed loops with MT-based major branches intersecting at nodes (orange). Branchlets (green) can be seen between major branches. Scale=20µm.

(D) Central hubs of the network include MT ends and are bordered by an actin-rich boundary. Right panel shows cartoon of features including hub (blue) with multiple major branches converging, their MT ends visible in thresholded overlay (magenta). Scale=20µm.

(E) Representative image of branchlets, minor and major branches used in quantifications for (F, G). Top panel = Tubulin, Middle panel= Actin, Bottom panel= merged. White bars (15µm) designate branch cross-sections measured for counting MT (MT) peaks (right graphs), width and length. (Branchlets= absent of MTs) and "Branches" (MT-stabilized).

(F) Quantifications of branchlet and branch widths per MT peaks counted in line profiles.

(G) Quantifications of branchlet and branch lengths by category.

Figure 3.3: The dynamic syncytial branchlets react to stimuli with actin and MTs.

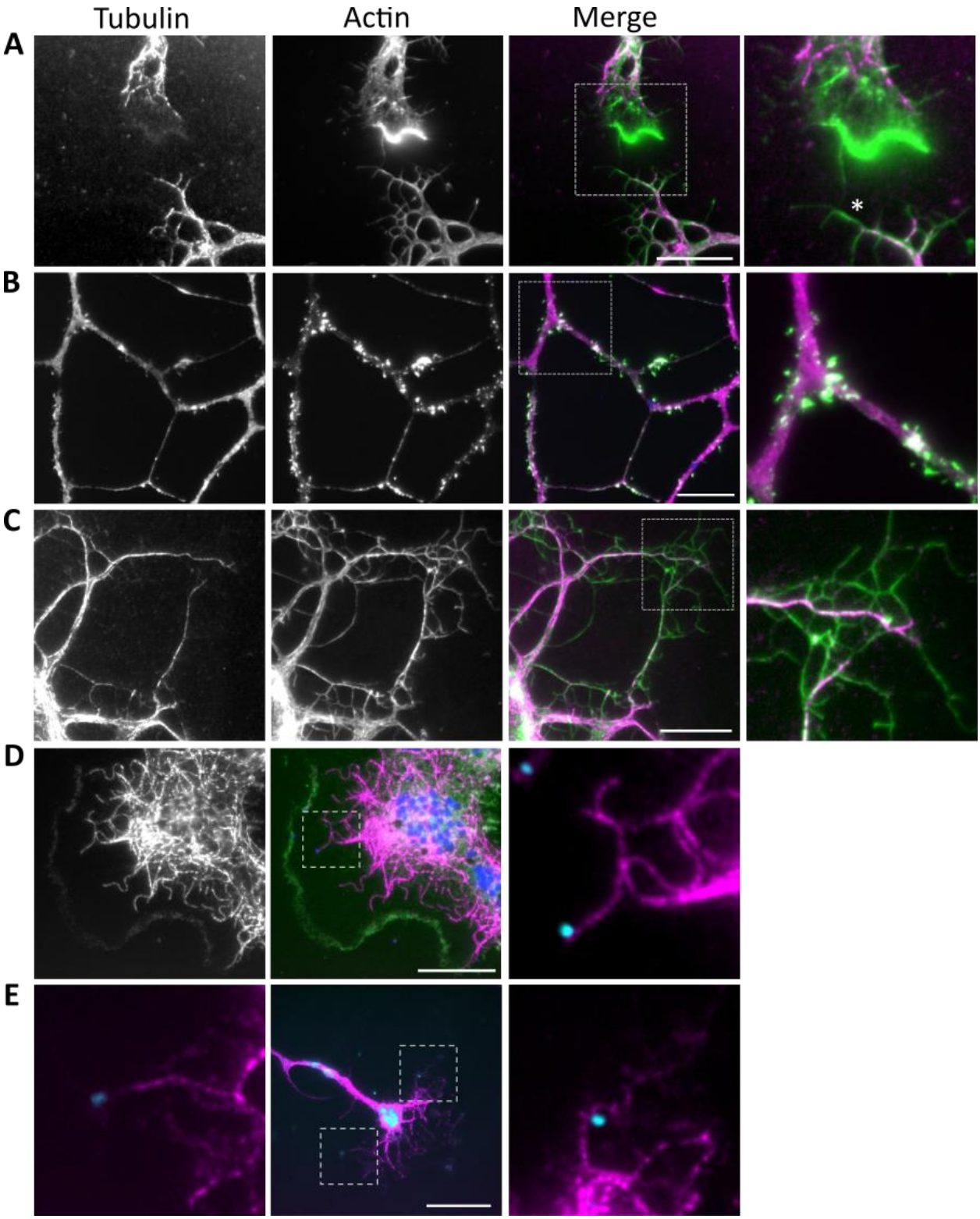

(A) Two syncytia (top and bottom) at the site of branchlet (filopodial) fusion (asterisk) show enriched actin at the lamellipodial and filopodial edges. (MT=Magenta, Actin=Green). scale=20µm.

(B) Internal branch topology with actin patches (green) immediately (<5min) after they are exposed to higher nutrient availability. scale=20µm.

(C) Starved syncytia with elongated (simplified) branches at the periphery exhibit actin-rich filopodia after being fed enriched medium. Inset shows new reticulopodia at tips of previously pruned branches. scale=50µm

(D) A wide lamellipodium with MTs exhibiting pronounced curvature. Right panel (inset) shows interaction with captured bacterial prey (cyan).

(E) A branch with straightened MTs has captured several bacteria. scale=20µm.

Figure 3.4: Organelles are rapidly and bidirectionally transported throughout the syncytial network.

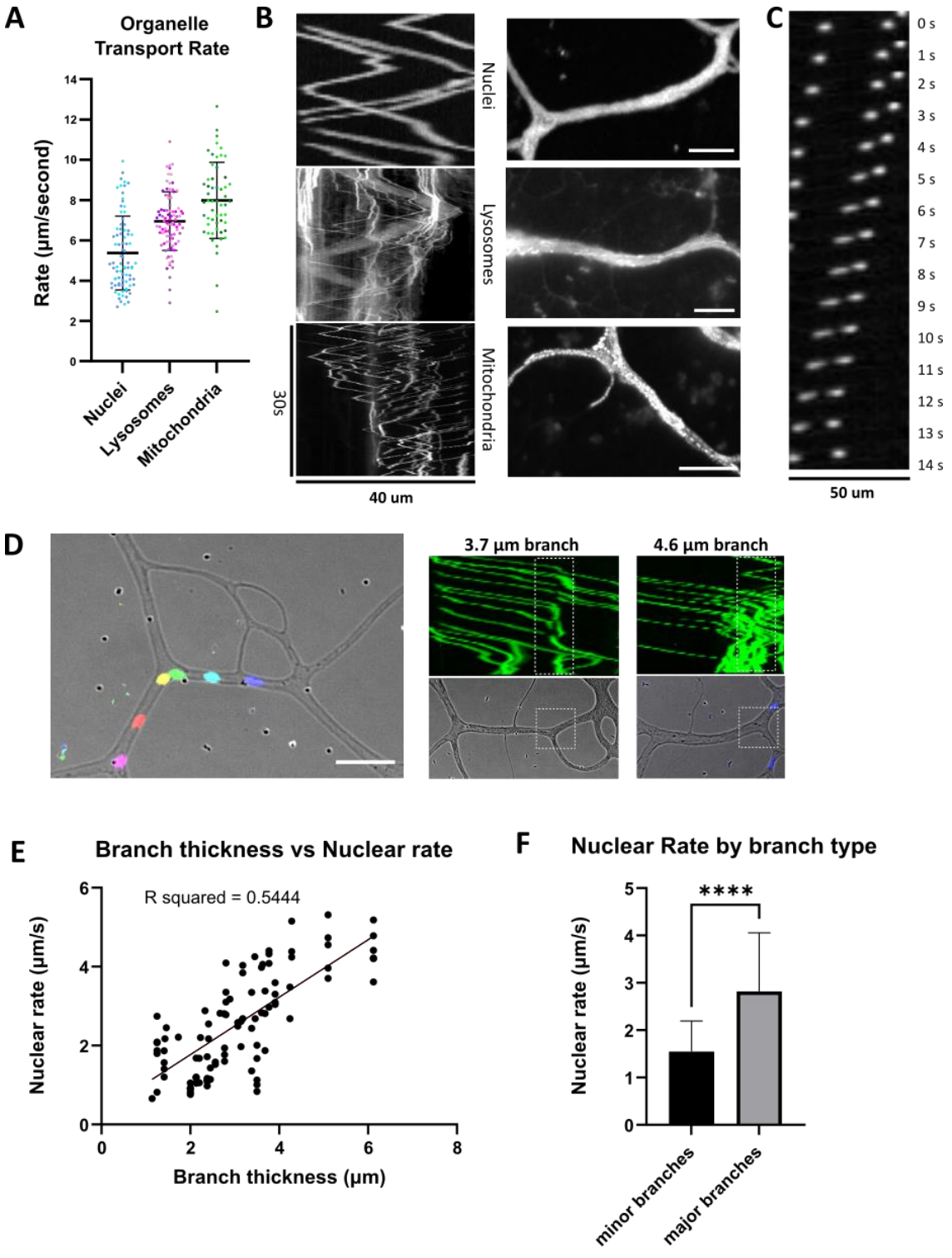

(A) Organelle transport rate quantified and presented as μm per second. lysosomes (n=89) mitochondria (n=55) nuclei (n=82). Datasets colored per replicate. (B) Representative kymographs of organelle movements over 40μm and 30 seconds. Right panels show branches used for kymographs, created as stack overlays. Scale=10 μm. (C) A montage shows nuclei are transported in a branch at different rates. Right nucleus changes direction at T=13s. (D) Nuclei traveling in branches become stalled or slow at nodes. Left panel is false-colored with 5 second intervals, scale = 20μm. Right panels show kymographs (green) of nuclear movements corresponding to the bottom panel branch images. Node locations in kymographs are outlined and correspond to inset squares. (E) The nuclear rate as a function of branch thickness (n=95). Nonlinear fit, R-squared = 0.544. (F) Transport rate quantified in (E) organized into minor and major branch categories based on thickness. ****$p<0.0001$ by unpaired T-test. (n=19 minor branches, n=76 major branches).

Figure 3.5: *Filoreta*'s complex syncytial patterns change throughout development.

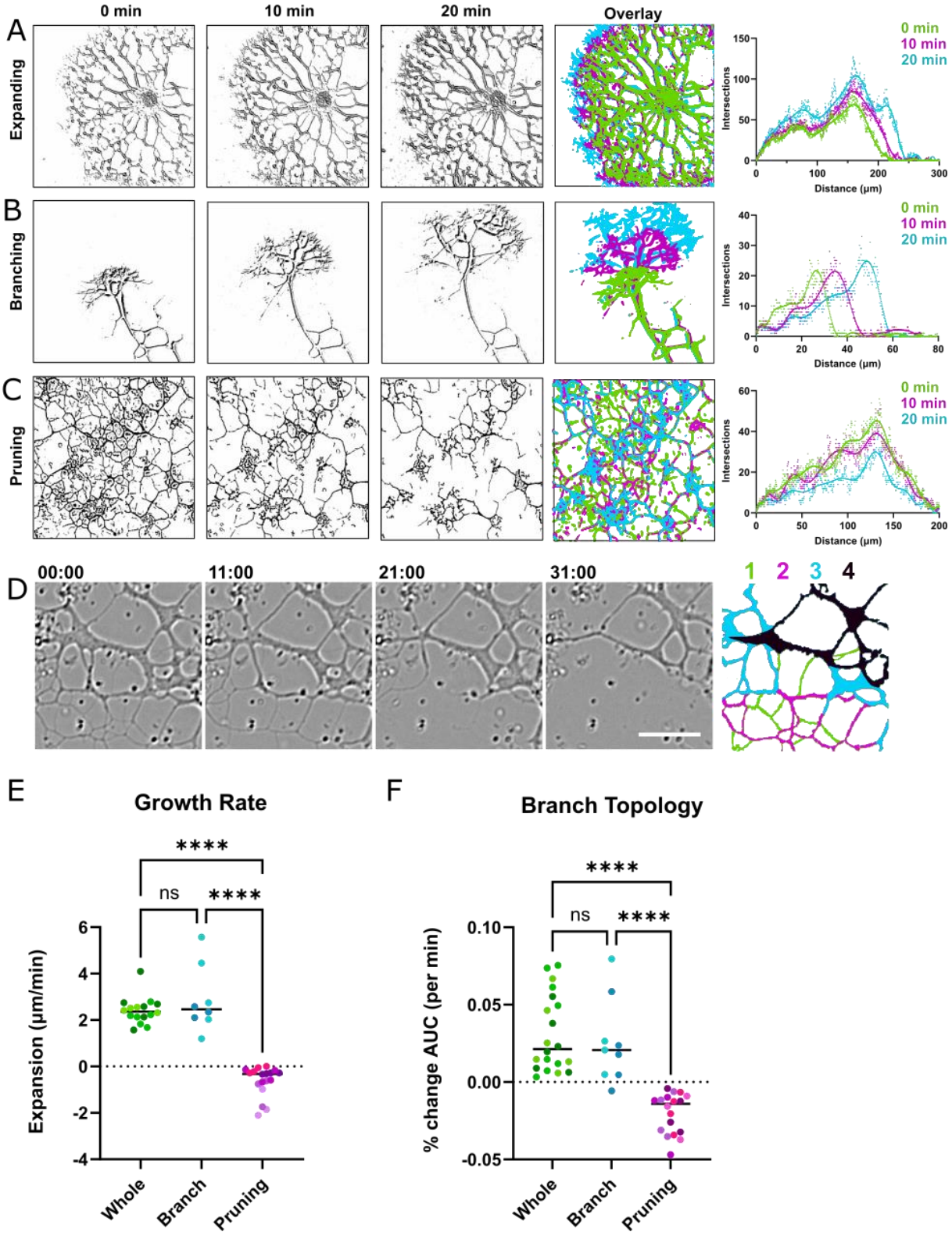

(A) The outward growth of a radially symmetrical syncytium over 10-minute intervals, thresholded image. 336.44μm width.

(B) Extension of a syncytium with broken symmetry showing elongating branch with arborizing branchlets. 151.40μm width.

(C) The entire syncytial network undergoes pruning when exposed to blinking light. 203.78μm width.

(D, E, F) Sholl Intersection Profiles (SIPs) at time points of whole radial syncytium shown in (A), branch shown in (B), and pruning shown in (C), respectively. Time points are color coded chronologically: green=0minutes, magenta=10 minutes, blue=20 minutes.

(G) The order of branch retraction during pruning, with the branch pruning false-colored in left panel. Branchlets in panel 1 disappear first (green), followed by minor branches in panel 2 (magenta), followed by thinning of major branches in panel 3 (blue) and loss of major branches (final panel, black). scale bar = 20 μm.

Quantification of peripheral growth rate from Sholl profiles (H) and change in branch topology (percent change in Area Under Curve) (I). n= 8 (branch) n= 16 (whole) n= 18 (pruning). ****$p<0.0001$, by ANOVA. Data sets colored per replicate.

Figure 3.6: Cytoskeletal drugs significantly perturb the growth in syncytial arbors.

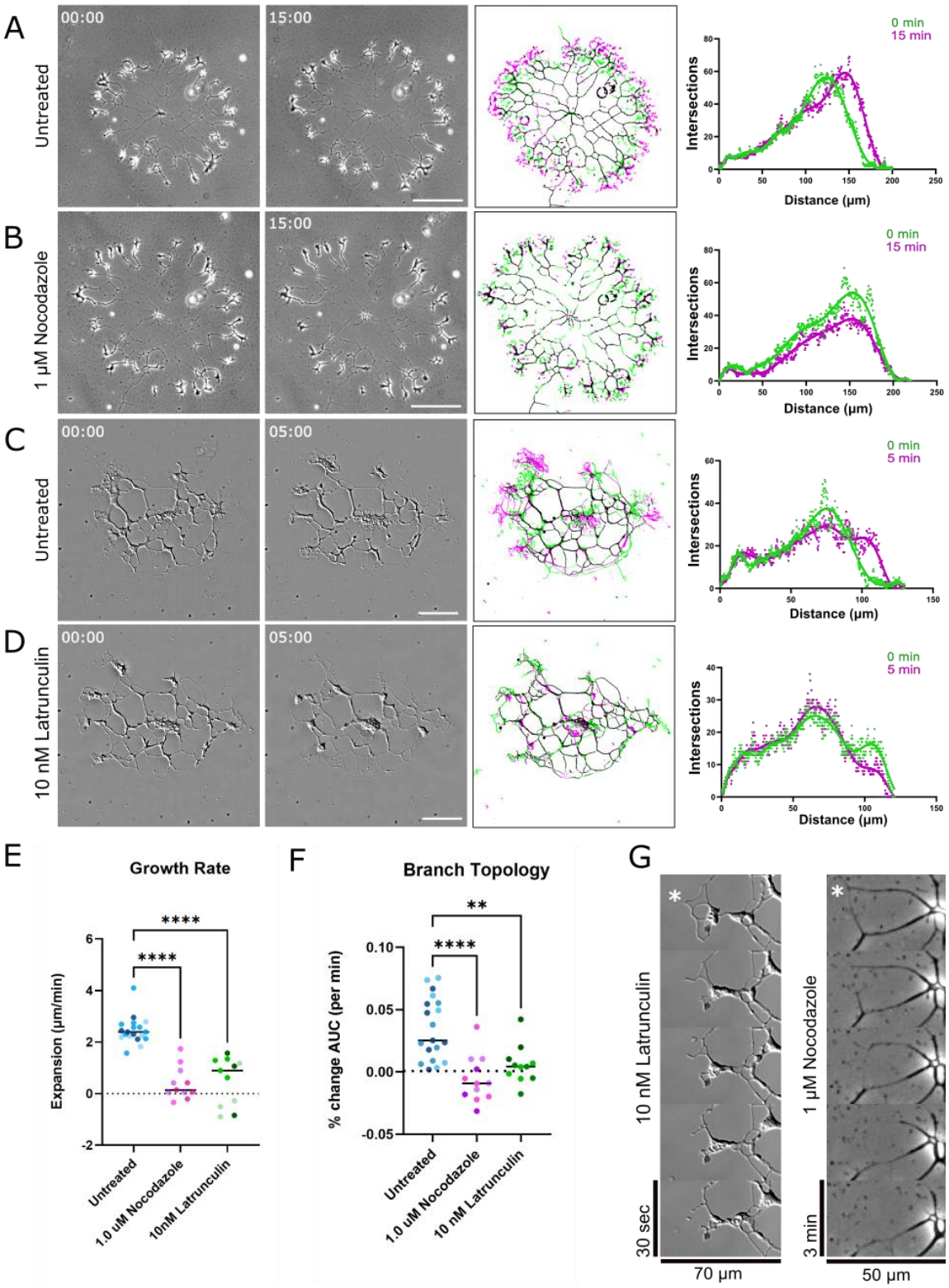

(A) An untreated syncytium grew outward over 15 minutes. False-colored thresholded overlay (3rd panel) shows each timepoint superimposed. Green=0 minutes, Magenta=15 minutes, Black=locations branches remained unchanged between both images. Scale bar = 100µm. Far-right panel is the SIP for each timepoint, showing syncytial growth. (B) The same syncytium was then treated with 1.0 µM Nocodazole and imaged for 15 minutes. The 3rd panel overlay shows areas of branch retraction (see montage in G). Green branches were present in T=0, and Magenta branches are present in T=15, with Black marking the locations of the overlap. Far-right panel is the respective SIP, with marked reduction of arbor topology due to branch retraction.

(C) An untreated syncytium grew outward for 5 minutes. False-colored threshold is labeled as in (A) and (B). The corresponding SIP in the far-right panel shows branchlet extension. Scale bar = 50µm. (D) The same syncytium was then treated with 10nM Latrunculin A and imaged for 5 minutes. The 3rd panel shows the change in morphology as branchlets retracted (areas of green), while the internal topology remains relatively unchanged (black). The corresponding SIP shows the quantified loss of branchlet structure at the periphery following treatment. Pseudopodia and branchlets retract and cease outward expansion (see montage in G).

(E)The growth rate of syncytia is significantly affected by cytoskeletal drugs. These experiments were repeated to quantify effects of each drug on the syncytial arbors. The growth rate of each syncytium was calculated by the difference in SIPs as µm/minute. The quantified expansion for each treatment group was then statistically compared with each other using ANOVA (****$p<0.0001$). Control (n=19), Nocodazole (n=11), Latrunculin (n=11). (F) Branch topology is significantly affected by drug treatments. The area under the curve (AUC) was calculated between time points and presented as a change in percentage of total AUC. The quantified change in topology for each treatment group was then statistically compared with each other

using ANOVA (**p=0.0017, ****p<0.0001). Control (n=19), Nocodazole (n=11), Latrunculin (n=11). Superplot data points are colored by replicates per date.

(G) Montage of examples of each described effect seen in Latrunculin and Nocodazole treatments, showing pseudopodial branchlet retraction (left panel) and internal branch loss (right panel), respectively.

Figure 3.7: Nocodazole treatment significantly alters the MT distribution throughout the network.

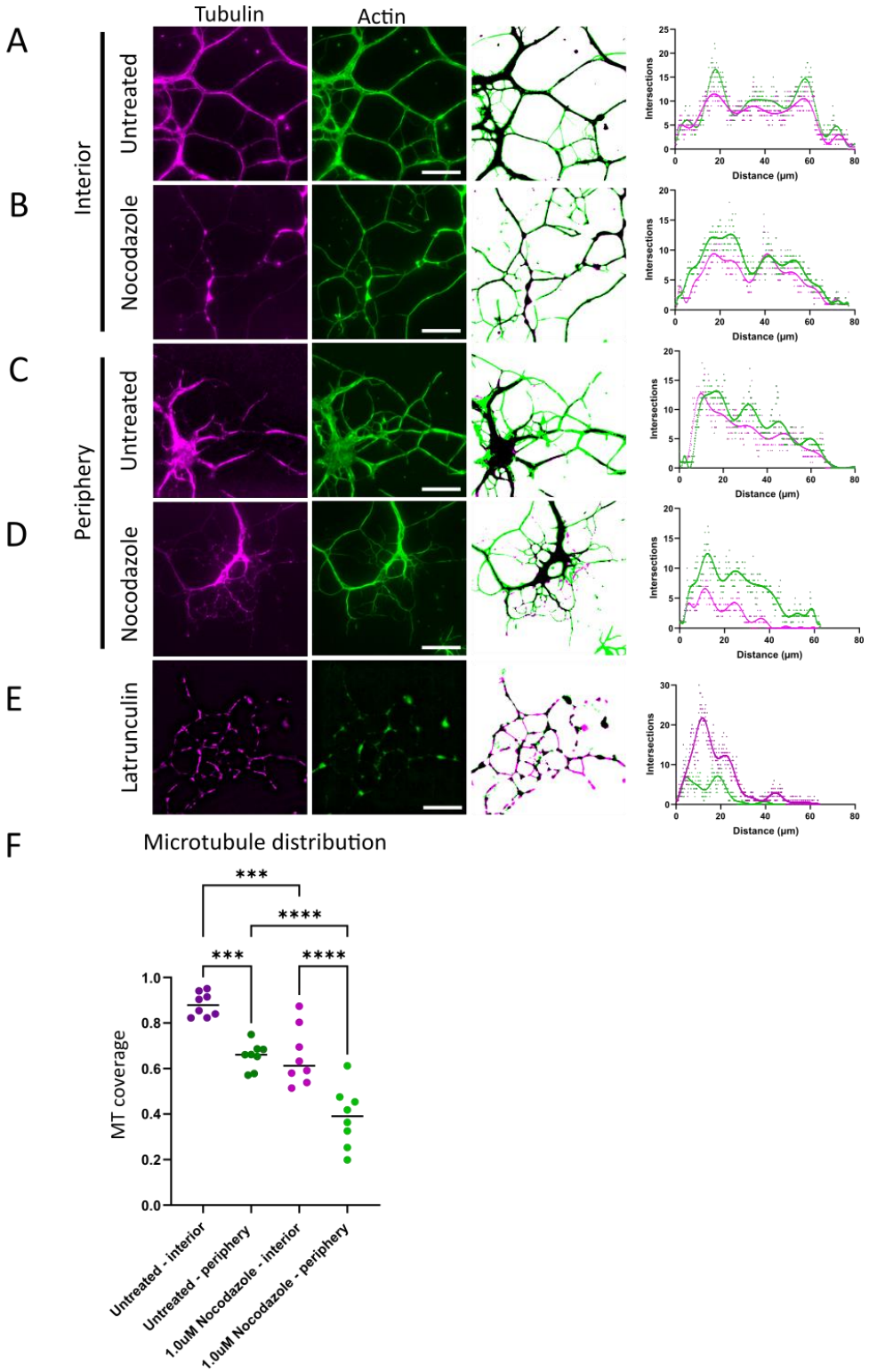

(A) The syncytial branch topology of the interior is filled in with MTs (magenta), and actin (green). A false-colored overlay (third panel) shows the proportion of branches (MT-filled, black) and branchlets (actin only, green). The corresponding Sholl profile (far right) for each cytoskeletal component's quantified distribution. Scale=20 μm.

(B) The MT and actin distribution of a nocodazole-treated syncytium interior. The false-colored overlay shows tubulin staining relative to actin stained branches. A corresponding Sholl profile for each cytoskeletal component's quantified distribution. Scale=20 μm.

(C) The peripheral branches are partially filled with MTs compared to actin. A false-colored overlay shows the proportion of branches (MT-filled, black) and branchlets (actin only, green). The corresponding Sholl profile for each cytoskeletal component's quantified distribution. Scale=20 μm.

(D) The periphery of a syncytium treated with nocodazole stained for MTs and actin. The corresponding overlay (third panel) and Sholl profiles showing decreased MT distribution compared to actin. Scale=20 μm.

(E) A syncytium treated with latrunculin has altered distribution of MTs and actin. The false colored overlay shows relative distribution and the corresponding Sholl profile of quantified distribution of each component. Scale=20 μm.

(F) Relative Sholl profiles quantified as a percent of MT coverage within the actin-stained network. The interior and periphery of untreated syncytia have significantly different MT distributions (*** $p=0.0006$). The MT distribution is significantly different between both interior (***$p=0.0005$) and periphery of nocodazole-treated syncytia, compared to untreated (****$p<0.0001$), by ANOVA. n=8 for all categories.

Figure 3.8: Nuclei are actively transported along MTs via dynein.

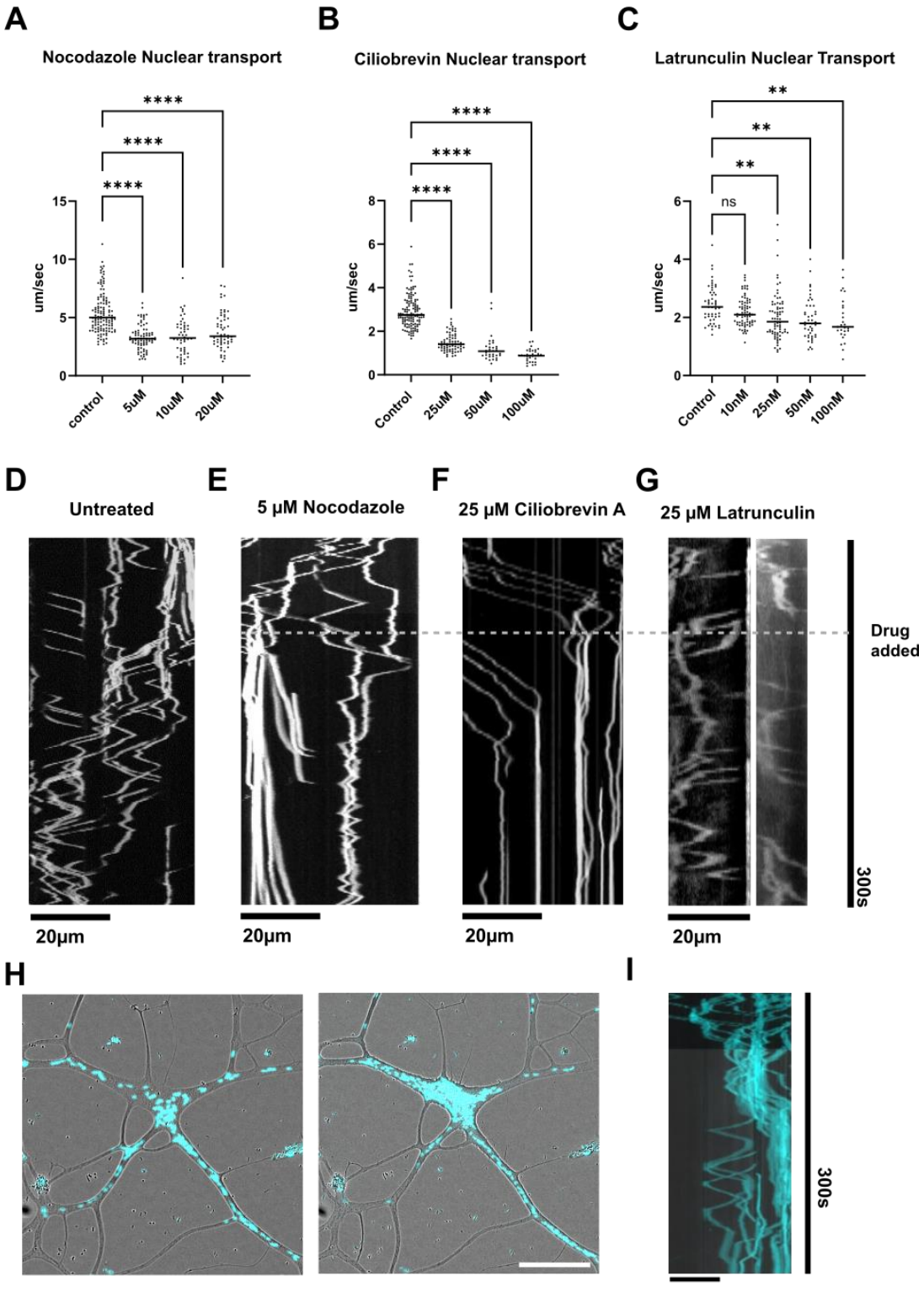

(A) Quantified nuclear rates in μm/second for processive movements of 10μm or longer; for Nocodazole concentrations of 5 μm (n=80), 10 μm (n=50), and 20 μm (n=57). Control (n=126). ****p< 0.0001.

(B) Quantified nuclear rates in μm/second for processive movements of 10μm or longer; for Ciliobrevin concentrations of 25 μm (n=70), 50 μm (n=330), and 100 μm (n=33). Control (n=131). ****p< 0.0001.

(C) Quantified nuclear rates in μm/second for processive movements of 10μm or longer; for Ciliobrevin concentrations of 10nM, (ns=not significant) (n=74), 25 nM (**p=0.0032) (n=73), 50 nM (**p=0.0012) (n=45), and 100 nM (**p=0.0041) (n=27), the effects are significant. All treatments were statistically compared using one-way ANOVA against the control.

(D-G) Representative kymographs showing nuclear movements over a 5-minute time course. scale=20μm. In (E-G), the respective cytoskeletal drugs were added at the 1-minute timepoint (dotted line).

(H) Effect of 20 μm Nocodazole on nuclear trafficking at t=0 (left panel) and t=5 min (right panel) (nuclei=cyan). scale=50 μm.

(I) Kymograph of 25 μm ciliobrevin showing bidirectional movement is slowed by not absent. scale=20μm.

Figure 3.9: GCP3 colocalizes with gamma tubulin in branch nodes, independently of nuclear location.

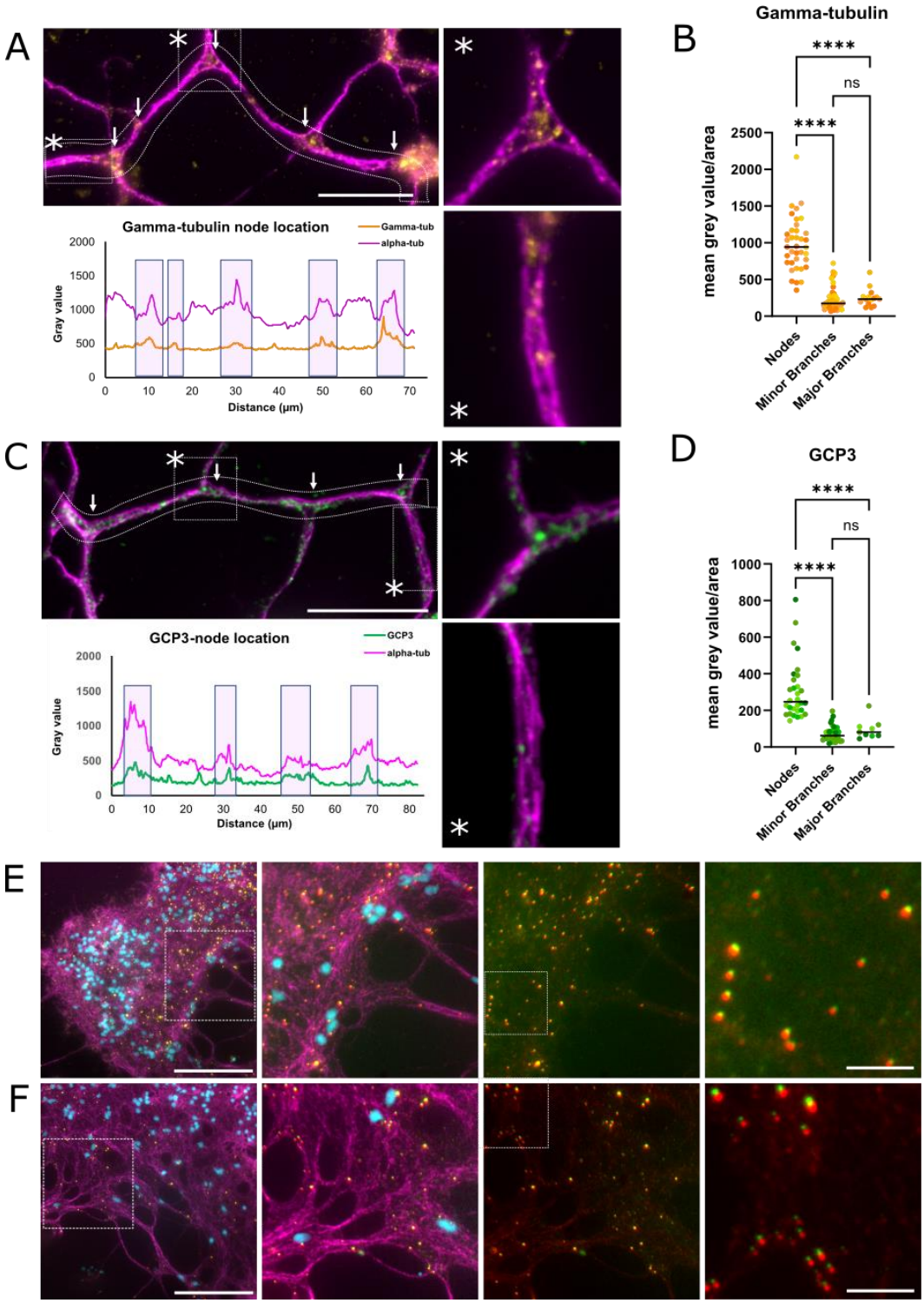

(A) A syncytium (gamma-tubulin=yellow, MT=magenta) shows localization of gamma tubulin is enriched at nodes (arrows) (top panel)(scale=20μm). The intensity profile was plotted for the outlined region in the image, with nodes marked in shaded areas.

(B) Quantification of signal intensity (mean grey value) over area, comparing nodes with internode branches. Comparison by unpaired T-test (****$p<0.0001$)(n=79, branches; n=88, nodes). Color coded dark and light orange by replicate image sets.

(C) A syncytium (GCP3=green, MT=magenta) showing localization of GCP3 puncta enriched at nodes (arrows) (top panel)(scale=20μm). The corresponding intensity profile (bottom panel) for the marked area shows peaks in GCP3 signal intensity at nodes (shaded).

(D) Quantification of signal intensity at nodes vs branches as in (B). n=37 (branches); n=52 (nodes). Color coded dark and light green by replicate image sets.

(E,F) Syncytia stained with gamma-tubulin and GCP3 exhibit puncta at the same locations. right panels shows inset (scale=60μm). Red=GCP3, green=gamma-tubulin, magenta=MT, cyan=nuclei.

Figure 3.10: EB1 localizes to nuclei in distinct puncta

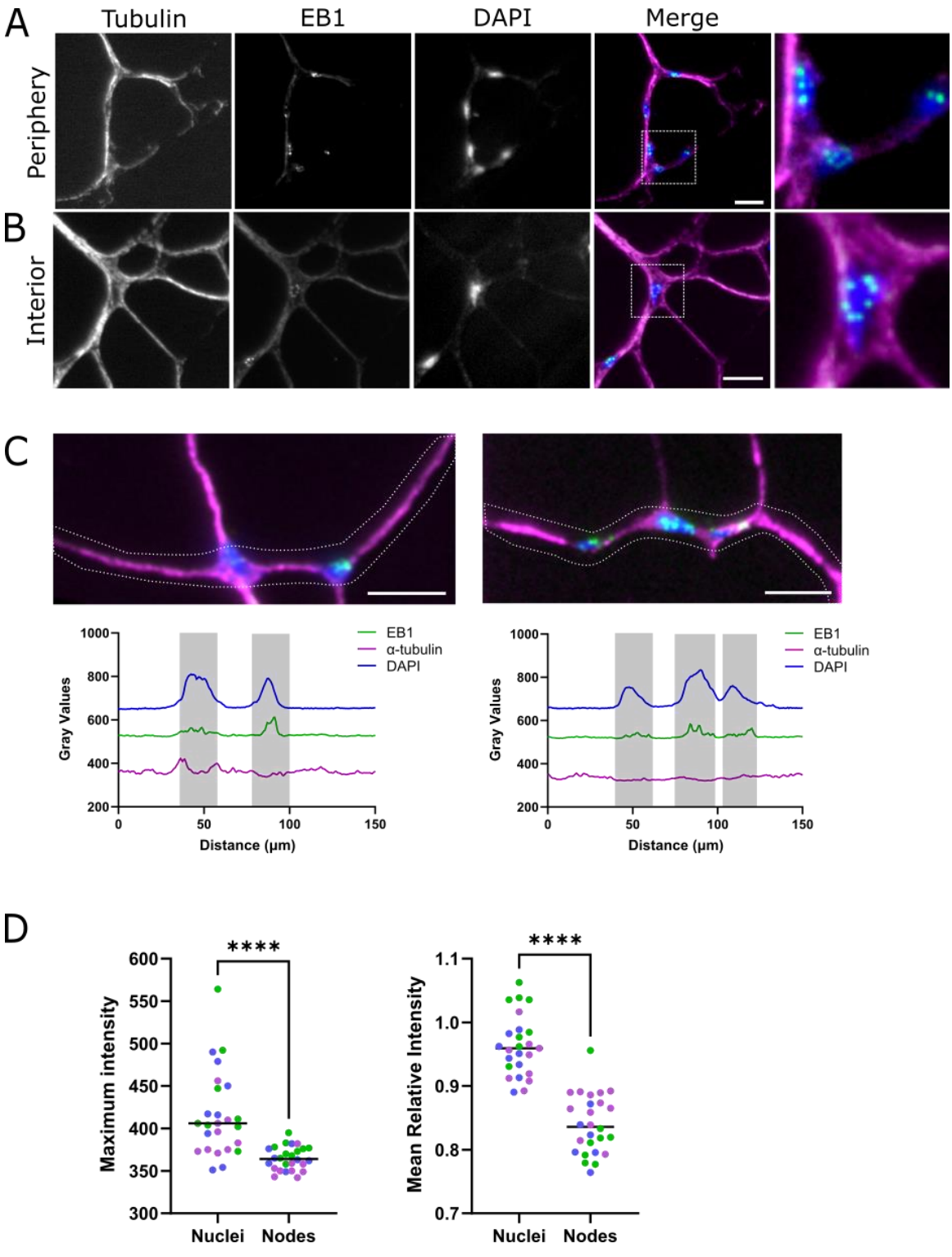

(A) At the syncytial periphery, EB1 localizes to puncta in close proximity to nuclei, and diffusely along MTs (Magenta= MTs, Green=EB1, Blue=DAPI). Scale=5µm.

(B) In the syncytial interior, EB1 localizes to puncta in close proximity to nuclei, and diffusely along MTs. Scale=5µm.

(C) Two examples of syncytia showing localization of EB1 puncta at the same location as nuclei (top panels) (scale=5µm). The corresponding intensity profile (bottom panels) for the marked area (white dotted outline) shows peaks in EB1 signal intensity at nuclei (shaded areas, DAPI peaks).

(D) EB1 puncta quantified by maximal intensities in nuclei vs nodes (left). Mean values normalized to relative intensity of tubulin per unit area measured (right). (nuclei; n=25, nodes; n=26). **** $p<0.0001$ by unpaired t test. Both datasets are color-coded by replicate image sets.